# ULTRAFAST DYNAMICS OF CARRIERS IN GERMANIUM PROBED BY BROADBAND FEMTOSECOND SPECTROSCOPIC ELLIPSOMETRY

BY

CARLOS ANTONIO ARMENTA, B.S., M.S.

A dissertation submitted to the Graduate School

in partial fulfillment of the requirements

for the degree

Doctor of Philosophy

Major Subject: Physics

New Mexico State University

Las Cruces, New Mexico

June 2025

"Ultrafas<br/>at dynamics of carriers in germanium probed by broadband femtosecond

spectroscopic ellipsometry, " a dissertation prepared by Carlos A. Armenta in

partial fulfillment of the requirements for the degree, Doctor of Philosophy, has

been approved and accepted by the following:

Ranjit Koodali

Interim Dean of the Graduate School

Stefab Zollner

Chair of the Examining Committee

Date

Committee in charge:

Dr. R.T. James McAteer

Dr. Igor Vasiliev

Dr. Michael Engelhardt

Dr. Stefan Zollner, Cahir

ii

# DEDICATION

I dedicate this work to  $\dots$ 

### ACKNOWLEDGMENTS

This research was funded by the Air Force Office of Scientific Research under award numbers FA9550-20-1-0135 and FA9453-23-2-0001, by the Department of Energy, National Nuclear Security Administration under Award Number DE-NA0004103, and by the National Science Foundation under Award Number DMR-2423992. Contributions and discussions with José Menéndez are gratefully acknowledged. Contributions and discussions with Carola Emminger are gratefully acknowledged. Contributions and discussions with Martín Zahradník, Mateusz Rebarz, Shirly Espinoza, Saul Vazquez-Miranda, and Jakob Andreasson from ELI ERIC are gratefully acknowledged. CAA gratefully acknowledges support from the J. A. Woollam Foundation. The author is grateful for this support, which enabled the experimental and theoretical work described herein.

## VITA

September 19, 1990	Born at El Paso, Texas
2010-2015	B.S., New Mexico State University, Las Cruces, NM
2017-2019	B.S., New Mexico State University, Las Cruces, NM
2019-2022	M.S., New Mexico State University, Las Cruces, NM
2019-2022	Teaching Assistant, Department of Physics, New Mexico State University, Las Cruces, NM
2021-2025	Research Assistant, Department of Physics, New Mexico State University, Las Cruces, NM

## **PUBLICATIONS**

- M. R. Arias, C. A. Armenta, C. Emminger, C. M. Zamarripa, N. S. Samarasingha, J. R. Love, S. Yadav, and S. Zollner, J. Vac. Sci. Technol. B 41, 022203 (2023).
- C. A. Armenta, M. Zahradník, M. Rebarz, C. Emminger, S. Espinoza, S. Vazquez-Miranda, J. Andreasson, and S. Zollner, 2024 IEEE Photonics Society Summer Topicals Meeting Series (SUM), Bridgetown, Barbados, 2024, pp. 01-02.
- S. Zollner, C. A. Armenta, S. Yadav, and J. Menéndez, J. Vac. Sci. Technol. A 43, 012801 (2025).
- C. A. Armenta and S. Zollner, J. Appl. Phys. 137, 245701 (2025).

### MANUSCRIPTS IN PROGRESS

C. A. Armenta, M. Zahradník, M. Rebarz, C. Emminger, S. Espinoza, S. Vazquez-Miranda, J. Andreasson, and S. Zollner, *Band Filling and Relaxation Effects in the Transient Dielectric Function of Ge.* 

#### **PRESENTATIONS**

Carlos A. Armenta, M. Zahradník, C. Emminger, S. Espinoza, M. Rebarz, Saul Vazquez-Miranda, J. Andreasson, S. Zollner, Band Filling and Relaxation Effects in the Transient Dielectric Function of Ge. 10<sup>th</sup> International Conference on Spectroscopic Ellipsometry. Boulder, CO, June 9, 2024.

Carlos A. Armenta and S. Zollner, Excitonic Effects at the Temperature-dependent  $E_1$  and  $E_1 + \Delta_1$  Critical Points of Ge. 10<sup>th</sup> International Conference on Spectroscopic Ellipsometry. Boulder, CO, June 13, 2024.

Carlos A. Armenta, M. Zahradník, C. Emminger, S. Espinoza, M. Rebarz, Saul Vazquez-Miranda, J. Andreasson, S. Zollner, Band Filling and Relaxation Effects in the Transient Dielectric Function of Ge. AVS 70<sup>th</sup> International Symposium & Exhibit. Tampa, FL, November 8, 2024.

Carlos A. Armenta, M. Zahradník, C. Emminger, S. Espinoza, M. Rebarz, Saul Vazquez-Miranda, J. Andreasson, S. Zollner, Efectos de saturación de banda y relajación en la función dieléctrica transitoria de Ge. LXVI Congreso Nacional de Física. Chihuahua, México, October 9, 2024.

Carlos A. Armenta, M. Zahradník, C. Emminger, S. Espinoza, M. Rebarz, Saul Vazquez-Miranda, J. Andreasson, S. Zollner, Band Filling and Relaxation Effects in the Transient Dielectric Function of Ge. IEEE 2024 Summer Topical Meeting Series. Bridgetown, Barbados, July 16, 2024.

Carlos A. Armenta, M. Zahradník, C. Emminger, S. Espinoza, M. Rebarz, Saul Vazquez-Miranda, J. Andreasson, S. Zollner, Modeling Many-body Effects in Ge Using Pump-Probe Time-Resolved Spectroscopic Ellipsometry. AVS 69<sup>th</sup> International Symposium & Exhibit. Portland, OR, November 6, 2023.

Carlos A. Armenta, M. Zahradník, C. Emminger, S. Espinoza, M. Rebarz, Saul Vazquez-Miranda, J. Andreasson, S. Zollner, Coherent Acoustic Phonon Oscillations in Ge Using Pump-Pulse Time-Resolved Spectroscopic Ellipsometry. 12<sup>th</sup> Workshop on Spectroscopic Ellipsometry. Prague, Czech Republic, September 19, 2023.

Carlos A. Armenta, M. Zahradník, C. Emminger, S. Espinoza, M. Rebarz, J. Andreasson, S. Zollner, Coherent Acoustic Phonon Oscillations in Ge Using Pump-Pulse Time-Resolved Spectroscopic Ellipsometry. APS March Meeting 2023, Las Vegas, NV, March 8, 2023.

Stefan Zollner, Melissa Rivero Arias, Carlos A. Armenta, Carola Emminger, Cesy M. Zamarripa, Jaden R. Love. Temperature dependence of the infrared dielectric function and the direct band gap of InSb from 80 to 725 K. APS March Meeting 2023, Las Vegas, NV, March 7, 2023.

Carlos A. Armenta, M. Zahradník, C. Emminger, S. Espinoza, M. Rebarz, J. Andreasson, S. Zollner, Coherent Acoustic Phonon Oscillations in Ge Using Pump-Pulse Time-Resolved Spectroscopic Ellipsometry. AVS 68<sup>th</sup> International Symposium & Exhibit. Pittsburgh, PA, November 8, 2022.

## ABSTRACT

# ULTRAFAST DYNAMICS OF CARRIERS IN GERMANIUM PROBED BY BROADBAND FEMTOSECOND SPECTROSCOPIC ELLIPSOMETRY

BY

## CARLOS ANTONIO ARMENTA, B.S., M.S.

Doctor of Philosophy

New Mexico State University

Las Cruces, New Mexico, 2025

Dr., Chair

This dissertation aims to investigate the transient dielectric function (DF) of Germanium at very high electron-hole pair densities using time-resolved spectroscopic ellipsometry. By employing a pump-probe technique, we explore the evolution of the critical points near the L-valley on a femtosecond time scale. Through modeling the DF of the material under different carrier temperatures, we analyze the impact that the photo-induced phenomena, such as phase-filling and many-body effects, have on the material's optical properties.

Pump-probe ellipsometry measurements were conducted on Ge from -10 ps to 1 ns delay time with a minimum step size of 50 fs. The pump pulse was energetic enough to achieve carrier densities on the order of  $10^{20}$  cm<sup>-3</sup>. The evolution of the DF over delay time is dictated by the ultrafast dynamics of the photo-excited carriers. Since the critical points (CPs)  $E_1$  and  $E_1 + \Delta_1$  lie inside the energy range of our probe (1.8 to 3 eV), the primary focus of our model is to describe these features as a function of delay times. Given the two-dimensional character of these CPs, the absorption of Ge is significantly enhanced by excitonic effects. Furthermore, at high carrier densities, intervalley scattering and band saturation will play a significant role in the optical response of the material. To address these effects, we combined band-filling effects with a 2D excitonic line shape to model the DF. We also simulated the Fermi energies and carrier temperatures governing the measurements using Fermi-Dirac statistics. The relaxation of photoexcited carriers occurs in very short timescales. As a result, this analysis focuses exclusively on the first few picoseconds after excitation, which is the temporal regime where carrier dynamics were modeled and simulated.

Our aim is to enhance our understanding of Ge's optical behavior under intense laser excitation. These findings provide quantitative insight into the timescales and mechanisms governing carrier relaxation in Ge and demonstrate the utility of femtosecond ellipsometry as a sensitive probe of nonequilibrium semiconductor dynamics. Moreover, we seek to translate these results to describe other materials

of interest, providing new insights into the ultrafast dynamics of carriers and their influence on the optical properties of diverse materials. The results have implications for the design of high-speed optoelectronic devices and contribute to the broader understanding of ultrafast processes in indirect bandgap semiconductors.

# CONTENTS

LIST	Γ OF TABLES	xiv
LIST	Γ OF FIGURES	XXV
1	INTRODUCTION	1
2	BACKGROUND AND THEORETICAL FRAMEWORK	3
2.1	Classical optics	3
2.2	Semiconductor optics	7
2.3	Excitonic effects	12
2.4	Carrier dynamics	15
	2.4.1 Ultrafast processes	15
	2.4.2 Many-body effects	18
	2.4.3 Carrier diffusion	19
3	EXPERIMENTAL METHODS	21
3.1	Spectroscopic Ellipsometry	21
3.2	Broadband Femtosecond Ellipsometry	25
4	MODELING THE STEADY-STATE DIELECTRIC FUNCTION	
	OF GE	35
4.1	Two-dimensional excitons	35
4 2	Experimental data	39

4.3	Tangu	y model	40
	4.3.1	Temperature dependence of the fixed parameters	44
	4.3.2	Unrenormalized effective mass	45
	4.3.3	Complete model	47
4.4	Result	s	48
	4.4.1	Fitting procedure	48
	4.4.2	Temperature dependence of the fitting parameters	50
	4.4.3	Dielectric function	54
	4.4.4	Fitting the effective mass	58
4.5	Discus	sion	61
5	RESU	LTS AND ANALYSIS	64
5.1	Data p	presentation	64
5.2	Ultrafa	ast dynamics and band filling	66
	5.2.1	Carrier statistics	69
	5.2.2	Dielectric function	75
	5.2.3	Thermal equilibrium	79
5.3	Final	model and interpretation	83
5.4	Fitting	g procedure	84
5.5	Carrie	r relaxation	87
6	CONC	CLUSION AND OUTLOOK	92
6.1	Summ	ary of main findings	92

6.2	Limitations of the model	93
6.3	Future work	94
6.4	Preliminary results on additional samples	95
6.5	Conclusion	97
A	Effective masses	98
A.1	Parabolic approximation at the L-point	98
A.2	Non-parabolicity at the L-point with small spin-orbit interaction .	100
В	Dielectric function of Ge	103
С	Unrenormalized energies	105
D	Fitting procedure	107
D.1	Extended Gaussian digital filter	111
D.2	Savitzky-Golay digital filter	112
Ε	Direct bandgap	114
F	Surface effects	117
G	Band-filling effects	118
DDT	DEDENICEO	101

# LIST OF TABLES

1	Fitted parameters of the Bose-Einstein model for the energy and	
	broadening of the $E_1$ and $E_1 + \Delta_1$ critical points	53
2	Samples with the pump power and beam diameter used for the	
	measurement. The thickness in parenthesis was determined with	
	WVASE32	95
3	Value of the fitting parameters and filter width $\Delta E$ for the extended	
	Gauss digital filter. The step size selected was 1 meV from 1.0 to	
	$3.2~{\rm eV}$ (2201 points). (f) indicates a fixed parameter	109
4	Value of the fitting parameters and order of polynomial $n$ for the	
	Savitzky-Golay digital filter. The frame length was constrain to $5\%$	
	of the number of points (11 points). (f) indicates a fixed parameter.	110

# LIST OF FIGURES

1	Band structure of Ge. The arrows indicate interband transitions of	
	the critical points	9
2	(a) Excitation of an electron-hole pair and formation of discrete	
	exciton states below the conduction band. (b) Schematic of the	
	imaginary part of the dielectric function, showing discrete absorp-	
	tion lines below the band edge and continuum absorption above	
	$E_g$	14
3	Schematic of a rotating compensator ellipsometry setup. The un-	
	polarized light has an angle of incidence $\theta$ , and its path comprises	
	a polarizer, sample stage, rotating compensator, and analyzer	21

4	Schematic of the broadband femtosecond spectroscopic ellipsome-	
	try setup. A beam splitter $\mathbf{BS}$ ) splits the initial (35 fs and 800 nm	
	wavelength) pulse into the pump and probe. In the pump path,	
	the pulse goes through a 250 Hz chopper $\mathbf{Ch}$ , the delay line $\mathbf{DL}$ ,	
	a focusing lens ${\bf L},$ and the sample ${\bf S}.$ On the probe path, the pulse	
	is redirected to ${\rm CaF_2}$ plate that transforms the infrared pulse into	
	white light via supercontinuum generation ( $\mathbf{SCG}$ ). This white light	
	probe pulse then goes trough a $\mathbf{PSC_RA}$ (polarizer, sample, rotat-	
	ing compensator, and analyzer) ellipsometry configuration stage,	
	before hitting the <b>CCD</b> detector	26
5	Reflectance-difference spectra recorded for each compensator angle.	
	The $y$ -axis shows detector pixel index (proportional to wavelength),	
	and the $x$ -axis shows the delay steps. Compensator, polarizer, and	
	analyzer angles are indicated in the lower right corner of each panel.	28
6	The spectral chirp correction polynomial (black line) fitted to the	
	$N,C,\mathrm{and}S$ elements of the sample Mueller matrix. For reference,	
	the differences of these matrix elements relative to their steady-	
	state values, $\Delta N$ , $\Delta C$ , and $\Delta S$ are also shown	30
7	The two choppers of the femtosecond setup give rise to four different	
	intensities. P1: Pump+probe, P2: Pump only, P3: Probe only, and	
	P4: Dark	31

8	Real (left) and imaginary (right) part of the point-by-point dielec-	
	tric function fit as a function of energy from $1.8~\mathrm{eV}$ to $3~\mathrm{eV}$ and	
	delay-time from -0.25 ps to 3.5 ps	32
9	Photographs of key components of the experimental setup: (a) the	
	delay line, (b) the supercontinuum generation stage, and (c) the	
	spectroscopic ellipsometry stage. In each panel, the red line indi-	
	cates the 800 nm pump beam path, while the white line traces the	
	probe beam path	34
10	Band structure of Ge in the $\Lambda$ -direction, where the $E_1$ and $E_1 + \Delta_1$	
	transitions (black arrows) are located. The range of wave vectors	
	<b>k</b> where these transitions take place is labeled $k_{\text{max}}$ (grey region).	35
11	Because the longitudinal reduced mass $\mu_{\parallel}$ is much larger than the	
	transverse reduced mass $\mu_{\perp}$ in the CPs $E_1$ and $E_1 + \Delta_1$ , the excitons	
	are restricted to the plane perpendicular to the z-axis	39

12	(a) Real and (b) imaginary part of the dielectric function of two-	
	dimensional Wannier excitons. This complex dielectric function	
	(solid black line) is composed of the continuum (red dot-dashed	
	line) and bound states (green dot-dashed line) of the exciton. No-	
	tice the similarity between the continuum state and the optical	
	dispersion for uncorrelated electron-hole pairs (blue dashed line).	
	The arbitrary values for the parameters are $E_1=2.2$ eV, $\Gamma=37$	
	meV, and $A = 41.8 \text{ eV}^2$	43
13	2 <sup>nd</sup> derivative of the real (a) and imaginary (b) part of the dielectric	
	function. The derivatives of the experimental data (translucent	
	lines) were calculated using the EG digital filter in Eq. (64). The	
	fitted 2 <sup>nd</sup> derivatives of Eq. (62) for each temperature are shown	
	by the solid lines	48
14	Bose-Einstein model fits for the energy (a) and broadening (b).	
	Shown by the squares are the fitted parameters, while the blue and	
	red solid lines are the Bose-Einstein models. For comparison, data	
	from different references is also shown.[17, 18, 32]	52

15	Real (a) and imaginary (b) part of the dielectric function of Ge	
	at 4 K. The translucent lines are the experimental data, the fitted	
	model with masses from the $\mathbf{k} \cdot \mathbf{p}$ -model in Eqs. (58) is shown by the	
	solid lines, and the model with the reduced mass as an additional	
	free parameter is shown by the dot-dashed lines	54
16	Dielectric function of Ge from 100 to 600 K. The translucent lines	
	are the experimental data, the fitted model from the $\mathbf{k}\cdot\mathbf{p}\text{-model}$	
	in Eqs. (58) is shown by the solid lines, and the model with the	
	reduced mass as an additional free parameter by the dot-dashed	
	lines	57
17	Fitted reduced masses as a function of temperature for $E_1$ ( $\square$ ) and	
	$E_1 + \Delta_1$ ( $\bigcirc$ ). The solid lines show results from Eqs. (58). The	
	dot-dashed and dashed lines are literature values at 4 K[11, 53] and	
	room temperature,[54] respectively	60
18	Comparison between the model at 4 K (red solid line) and the	
	point-by-point fits with different thicknesses for the oxide correction	
	(translucent lines)	62
19	Intensities of the four acquisition channels: dark (blue), probe only	
	(red), pump only (yellow), and pump+probe (purple). The inten-	
	sities are shown for three compensator angles	64
20	Reflectance difference for three compensator angles	65

21	Real (left) and imaginary (right) parts of the experiential dielectric	
	function after an oxide correction from -1 to 3 ps delay time	66
22	The initial 1.55 eV pump pulse (red arrows) promotes electrons	
	(gray circles) from the heavy-hole (blue line), light-hole (light blue	
	line), and split-off (cyan line) valence band to the conduction band	
	(black line) near the $\Gamma$ -point. The pump pulse also creates holes	
	(white circles) in the valence bands. Once in the conduction band,	
	the electrons thermalize and scatter to the L- and X-valley	67
23	Once the hot electrons (and holes) thermalize to a distribution with	
	a defined temperature, they raise the quasi-Fermi energy of the	
	conduction band $E_F^{(\mathrm{C})}$ (dark gray area) [and of the valence band	
	$E_F^{(\mathrm{V})}$ (gray area)]. Because Ge is an indirect semiconductor, the	
	electrons do not return to the $\Gamma$ -valley. Instead, they eventually	
	relocate from the X-valley to the L-valley (the lowest conduction	
	valley). At this stage, the energy required to move the electrons	
	from the valence band to the conduction band is given by the quasi-	
	Fermi energy $E_F^{({\rm C})}$ [and $E_F^{({\rm V})}$ ] plus the renormalized bandgap [this is	
	the definition of the chemical potential $\mu$ (black arrow)]. In the case	
	of the L-valley, it is the renormalized energy of the critical points	
	$\overline{E}_1$ and $\overline{E}_1 + \Delta_1$ , not the renormalized bandgap that influence the	
	interband transitions (green arrows)	69

24	Charge carrier density as a function of temperature. The black	
	line is given by Eq. (71a), and the red line is the same density	
	multiplied by 2. The squares $(\Box)$ show the density at the effective	
	carrier temperature given in Eq. (67)	71
25	(a) Chemical potential as a function of temperature for a density	
	of $5 \times 10^{19}$ cm <sup>-3</sup> (black line) and $10^{20}$ cm <sup>-3</sup> (red line). The squares	
	$(\Box)$ show the chemical potential at the effective carrier temperature	
	given in Eq. (67). (b) The relative population density $\Gamma$ -, L-, and	
	X-valley (black, blue, and red line, respectively) with respect to the	
	total density of Eq. (72)	75
26	Density of electrons and holes at 300 K as a function of chemical	
	potential in the parabolic (red and blue lines, respectively) and	
	non-parabolic approximation (dot-dashed black lines). The circles	
	( ) show the corresponding intrinsic chemical potential for both	
	approximations (purple for parabolic and black for non-parabolic	
	approximation)	80
27	Imaginary part of the two-dimensional excitonic dielectric function	
	(black solid line) along with the band-filling model using the chem-	
	ical potential in the parabolic and non-parabolic approximation	
	(green dot-dashed and red dashed lines, respectively)	82

28	Imaginary part of the dielectric function for the band-filling model	
	shown in Eq. (90). The black solid lines show the steady state	
	dielectric function. The colored curves shows the dielectric function	
	at different points in the evolution of the chemical potential [shown	
	in the circles (o) of the right-side plots]. The temperature and	
	chemical potential for the steady-state DF is shown by the black	
	circle (o) in the right-side plots. (a) presents the evolution of the	
	dielectric function for a density of $10^{20}$ cm <sup>-3</sup> . (b) shows the same	
	dielectric function for a density of $5 \times 10^{19}$ cm <sup>-3</sup>	85
29	(a) Transient dielectric function of Ge. Delay times range from	
	-0.5 ps up to the first 2 ps. (b) The model shown for the fitted	
	chemical potentials and carrier temperatures. (c) Experimentally	
	fitted chemical potential of the model as a function of the carrier	
	temperature	88
30	Experimentally fitted chemical potential of the model as a function	
	of the carrier temperature shown by the circles $(\circ)$ . For compari-	
	son, the theoretically calculated chemical potential for the carrier	
	densities $5 \times 10^{19}$ (red line) and $10^{20}$ cm <sup>-3</sup> (black line)	89

31	The fitted carrier temperature is shown on the left axis by the	
	circles $( \circ )$ as a function time delay. These experimentally obtained	
	values are fitted with an exponential function, shown by the red	
	line. On the right axis, the rate of energy relaxation is shown by	
	the green line	90
32	Fitted energy and broadening parameters for the critical points $E_1$	
	and $E_1 + \Delta_1$ . Negative delays (grey area) show the parameters for	
	a steady state measurement	91
33	Imaginary part of the dielectric function for the screening of 3D	
	excitons shown in Eq. (121). Smaller values of $g$ give greater	
	excitonic screening	94
34	Transient dielectric function of 200 nm of n-dopped Ge on 840 nm $$	
	of Ge on Si (001). The time delays show data from -1 to 100 ps	96
35	Transient dielectric function 345 nm of $\mathrm{Ge_{0.908}Sn_{0.092}}$ on Si (001).	
	The time delays show data from -1 to 100 ps	96
36	Band structure of Ge at the L-valley. The perpendicular $k_{\perp}$ -vector	
	is shown in atomic units where $a_0 = 0.53$ Å. The thick solid lines	
	represent the exact solution to the $3 \times 3$ Hamiltonian in Eq. (96),	
	the thin solid lines show the parabolic approximation, and the dot-	
	dashed lines are the small spin-orbit approximation	102

37	(a) Thermal expansion coefficient from Eq. (60)[38] (blue solid line)	
	and Eq. $(116)[112]$ (green solid line) compared to experimental data	
	(_).[114, 115] (b) The experimental values for $E_1$ and $E_1+\Delta_1$	
	(blue and red dot-dashed line, respectively) are shown along with	
	their respective unrenormalized energy (red and blue solid lines,	
	respectively). (c) On the left axis is the binding energy of the	
	excitons of the critical points (black and red solid lines). On the	
	right axis is the transverse reduced effective masses (green and blue	
	dot-dashed lines)	107
38	(a) Natural logarithm of the Fourier coefficient amplitude $C_n$ of	
	the real (red) and imaginary (blue) parts of the dielectric function	
	at 200 K. The same plot also shows the Fourier transform of the	
	extended Gaussian filter ( $\bigcirc$ ) for different filter widths. (b) $2^{\rm nd}$	
	derivative of the dielectric function calculated with the extended	
	Gauss filter ( ) and with the Savitzky-Golay filter (solid)	113

39	(a) In addition to the parabolic approximation (thin solid line),
	we show the exact solution (thick solid line) and the small spin-
	orbit approximation (dot-dashed) to the 8-band model of the band
	structure of Ge. (b) Imaginary part of the dielectric function at
	4 K in the parabolic approximation (solid) and including non-
	parabolicity linear terms in $\alpha\epsilon$ (dashed) and quadratic terms in $\beta\epsilon^2$
	(dot-dashed) of the density of states mass. (c) Parabolic (solid)
	and non-parabolic (dashed, dot-dashed) models extended up to 3 eV.114
40	Real (a) and imaginary (b) parts of the dielectric function of Ge
	from a point-by-point fit for three substrates with (100), (110), and
	(111) surface orientations (black, blue, and red, respectively) 118
<i>1</i> 1	110

#### 1 INTRODUCTION

From the development of the first transistors to contemporary photonic and electronic devices, Germanium (Ge) has played a pivotal role in the semiconductor industry. Beyond its historical significance, Ge exhibits unique electronic and optical properties, including a high carrier mobility, an indirect bandgap supplemented by strong direct transitions near 2 eV, and pronounced excitonic effects close to critical points in the Brillouin zone. These features make Ge an ideal candidate for exploring fundamental carrier dynamics under non-equilibrium conditions.

When a semiconductor is exposed to ultrafast optical excitation, photoexcited carriers are created with high excess energies and out-of-equilibrium distributions. Their subsequent relaxation mediated by carrier-carrier interactions determine key timescales for energy dissipation, recombination, and recovery of the equilibrium electronic system and dielectric response. In Ge, these processes are particularly interesting because of the interplay between indirect and direct transitions and the pronounced role of excitonic effects in the two-dimensional van Hove singularities  $E_1$  and  $E_1 + \Delta_1$ . Understanding these relaxation processes at femtosecond timescales is essential for modeling the transient optical properties of Ge and for the design of optoelectronic devices operating in high-field conditions.

Among the various techniques available to probe ultrafast carrier dynamics,

broadband femtosecond spectroscopic ellipsometry offers a unique combination of temporal and spectral resolution. Unlike conventional transient reflectivity or transmission measurements, ellipsometry provides access to the complex dielectric function without relying on Kramers–Kronig transformations. This capability enables direct observation of band filling, bandgap renormalization, and exciton effects with femtosecond resolution across a broad energy range. In this thesis, femtosecond ellipsometry is employed to disentangle the competing contributions to the transient dielectric function of Ge following strong optical excitation.

This work aims to investigate the ultrafast carrier dynamics in Ge by modeling the transient dielectric function obtained from time-resolved ellipsometric measurements. The specific objectives are:

- To develop a model incorporating band filling and excitonic effects in Ge's dielectric function near the  $E_1$  and  $E_1 + \Delta_1$  transitions.
- To measure the time-resolved changes in the dielectric response following femtosecond excitation and extract carrier temperatures and chemical potentials as a function of delay time.
- To estimate the characteristic energy relaxation rates of hot carriers and explain the mechanisms that govern the return to equilibrium.
- To evaluate the dependence of the dielectric function to the carrier density and temperature under present experimental conditions.

The thesis is organized as follows: chapter 2 provides a theoretical background on classical optics, polarization formalism, and the optical response of semiconductors. Chapter 3 describes the experimental methods, including the broadband femtosecond ellipsometry setup and data acquisition procedures. Chapter 4 presents the modeling of the steady-state dielectric function of Ge based on spectroscopic ellipsometry measurements. Chapter 5 develops the transient dielectric function model and details the fitting procedure used to obtain the carrier parameters. Chapter 6 discusses the results of time-resolved measurements, including carrier cooling dynamics and their consequences. Finally, Chapter 7 summarizes the main findings and outlines future research.

#### 2 BACKGROUND AND THEORETICAL FRAMEWORK

#### 2.1 Classical optics

Consider an electromagnetic (EM) field in a medium. Given the electric charges that exist within the atoms of the medium, the presence of this EM field will induce auxiliary fields that encompass polarization and magnetization effects. These auxiliary fields are the electric displacement and macroscopic magnetic fields

$$\mathbf{D} = \varepsilon_0 \mathbf{E} + \mathbf{P},\tag{1}$$

and 
$$\mathbf{H} = \frac{1}{\mu_0} \mathbf{B} - \mathbf{M},$$
 (2)

respectively. In Eq. (1),  $\varepsilon_0$  is the permittivity of free space, **E** is the electric component of the wave, and **P** is the electric dipole density induced by the electric field within the dielectric medium. In Eq. (2),  $\mu_0$  is the permeability of free space, **B** is the magnetic component of the wave, and **M** magnetization density of the material. These charge and current densities and auxiliary fields play an important role in the propagation of EM waves in a medium. We present the derivation of the non-homogeneous EM wave equations by starting with Maxwell's equations in a macroscopic medium,

$$\nabla \cdot \mathbf{D} = \rho, \qquad (Gauss' law) \tag{3a}$$

$$\nabla \cdot \mathbf{B} = 0,$$
 (Gauss' law for magnetism) (3b)

$$\nabla \times \mathbf{E} = -\frac{\partial \mathbf{B}}{\partial t},$$
 (Faraday's law) (3c)

$$\nabla \times \mathbf{H} = \mathbf{J} + \frac{\partial \mathbf{D}}{\partial t}$$
, (Ampere's law with Maxwell's correction) (3d)

Taking the curl of Eqs. (3c) and (3d), we can decouple this set of four 1<sup>st</sup> order partial differential equations (PDE) into a set of two decoupled 2<sup>nd</sup> order PDE. By doing so, we get the following EM waves equations:

$$\nabla^{2}\mathbf{E} - \varepsilon_{0}\mu_{0}\frac{\partial^{2}\mathbf{E}}{\partial t^{2}} = \mu_{0}\frac{\partial\mathbf{J}}{\partial t} + \mu_{0}\frac{\partial^{2}\mathbf{P}}{\partial t^{2}} + \frac{1}{\varepsilon_{0}}\boldsymbol{\nabla}\rho,$$
 (4a)

$$\nabla^2 \mathbf{B} - \varepsilon_0 \mu_0 \frac{\partial^2 \mathbf{B}}{\partial t^2} = -\mu_0 \mathbf{\nabla} \times \mathbf{J}. \tag{4b}$$

If we assume an isotropic, homogeneous, and nonconducting medium ( $\rho = 0$  and  $\mathbf{J} = 0$ ), we can obtain the solutions to Eqs. (4) of the form

$$\mathbf{E}(\mathbf{r},t) = \mathbf{E}_0 e^{i(\mathbf{k} \cdot \mathbf{r} - \omega t)} \tag{5}$$

and 
$$\mathbf{P}(\mathbf{r},t) = \mathbf{P}_0 e^{i(\mathbf{k} \cdot \mathbf{r} - \omega t)}$$
. (6)

This solutions hold true if

$$\mathbf{P}_0(\omega) = \varepsilon_0 \chi(\omega) \mathbf{E}_0(\omega), \tag{7}$$

where  $\chi(\omega)$  is the electric susceptibility [strictly speaking,  $\chi(\omega)$  is really a 2<sup>nd</sup> rank tensor, but we have assumed that material at hand is isotropic]. With this definition, we can redefine the electric displacement of Eq. (1) as

$$\mathbf{D} = \varepsilon_0 \left( 1 + \chi \right) \mathbf{E} = \varepsilon_0 \varepsilon_r \mathbf{E} \tag{8}$$

The new term  $\varepsilon_{\rm r}$  is called the complex relative dielectric constant. For simplicity, we will set the permittivity of free space to unity, making the dielectric constant equal to its relative counterpart. In other words,  $\varepsilon = \varepsilon_0 \varepsilon_{\rm r} = \varepsilon_{\rm r}$ . By inserting Eq. (7) in Eq. (5), and then to Eq. (4a), we get the dispersion relation

$$k = -\frac{\omega}{c}\sqrt{1+\chi} = -\frac{\omega}{c}\sqrt{\varepsilon}.$$
 (9)

In general,  $\varepsilon(\omega)$  is a complex number [hence,  $\chi(\omega)$  is also complex], which leads to a complex index of refraction,

$$\tilde{n} = n + i\kappa = \sqrt{\varepsilon} = \sqrt{\varepsilon_1 + i\varepsilon_2}.$$
(10)

The extinction coefficient  $\kappa$  accounts for the absorption of the medium. We see this by explicitly placing Eq. (10) in Eq. (5):

$$\mathbf{E}(\mathbf{r},t) = \mathbf{E}_0 e^{-\frac{\kappa \omega}{c} \hat{\mathbf{k}} \cdot \mathbf{r}} e^{i\left(\frac{n\omega}{c} \hat{\mathbf{k}} \cdot \mathbf{r} - \omega t\right)},\tag{11}$$

which conveys an exponential decay of the oscillatory behavior of a wave proportional to  $\kappa$ . In the literature, it is typical to use the absorption coefficient  $\alpha$  instead of the extinction coefficient.

$$\alpha = \frac{\kappa \omega}{c}.\tag{12}$$

The derivations for the electric field and the polarization vector in Eq. (5) are an oversimplification of the actual physical quantities at hand. The full definition of the polarization vector is

$$\mathbf{P}(\mathbf{r},t) = \varepsilon_0 \iiint \chi_{ij}(|\mathbf{r} - \mathbf{r}'|, |t - t'|) \mathbf{E}(\mathbf{r}', t') d^3 \mathbf{r}' dt'.$$
 (13)

Here, the indices i and j run through the components of the second-rank tensor  $\chi_{ij}$ . However, it is easier to work with Eq. (13) by Fourier transforming it, which changes  $(\mathbf{r},t) \to (\mathbf{k},\omega)$ . By doing this transformation, Eq. (13) reduces to

$$\mathbf{P}(\mathbf{k},\omega) = \varepsilon_0 \chi_{ij}(\mathbf{k},\omega) \mathbf{E}(\mathbf{k},\omega), \tag{14}$$

which is similar to Eq. (7). The relation between  $\varepsilon$  and  $\chi$ 

$$\varepsilon_{ij}(\mathbf{k},\omega) = 1 + \chi_{ij}(\mathbf{k},\omega).$$
 (15)

is still valid. The **k** dependence of  $\varepsilon_{ij}$  is called spatial dispersion. For simplicity, we will ignore this dependence from now on  $[\varepsilon_{ij}(\mathbf{k},\omega) \to \varepsilon_{ij}(\omega)]$ . If the material of interest is isotropic or has a cubic crystal structure (as is the case with diamond and zincblende semiconductors), we can simplify even further by noting that the tensor  $\varepsilon_{ij}$  has only three identical diagonal elements. Hence,  $\varepsilon_{ij}(\omega)$  becomes the usual dielectric function  $\varepsilon(\omega)$  of the material.

#### 2.2 Semiconductor optics

To calculate the dielectric function from first principles, we relate the light absorption of the material  $\varepsilon_2$  to the power lost by the field due to absorption per unit volume within the medium. This latter quantity is simply the transition probability per unit volume, R, multiplied by the photon energy  $\hbar\omega$ ,

$$R\hbar\omega = -\frac{\mathrm{d}I}{\mathrm{d}t} = -\frac{\mathrm{d}I}{\mathrm{d}x}\frac{\mathrm{d}x}{\mathrm{d}t} = \frac{c}{n}\alpha I. \tag{16}$$

Eq. (16) makes explicit use of Beer's law

$$\frac{\mathrm{d}I}{\mathrm{d}x} = -\alpha I,\tag{17}$$

where the absorption coefficient  $\alpha = \varepsilon_2 \omega / nc$  and the EM wave intensity  $I = cn\varepsilon_0 |\mathbf{E}(\omega)|^2 / 2$ . We can solve for the imaginary part of the dielectric function as

$$\varepsilon_2(\omega) = \frac{2\hbar R}{|\mathbf{E}(\omega)|^2}.\tag{18}$$

All is left in Eq. (18) is to find an expression for the transition probability rate R. To do so, we start with Schrödinger's equation. Treating incoming radiation

classically, the Hamiltonian for a single electron in the presence of an electric field is given as

$$\mathcal{H} = \underbrace{\frac{|\mathbf{p}|^2}{2m} + V(\mathbf{r})}_{\mathcal{H}^{(0)}} + \underbrace{\frac{e}{m} \mathbf{A} \cdot \mathbf{p}}_{\mathcal{H}^{(1)}} + \frac{e^2 |\mathbf{A}|^2}{2m}.$$
 (19)

Notice that the first two terms represent the unperturbed Hamiltonian  $\mathcal{H}^{(0)}$ . Using the **Coulomb gauge** ( $\phi = 0$  and  $\nabla \cdot \mathbf{A} = 0$ ), as well as ignoring the quadratic term, we can treat  $\mathcal{H}^{(1)}$  as a perturbation. Next, we use time-dependent perturbation theory in the form of Fermi's golden rule to get the transition probability rate from the valence band state  $|V\rangle$  to the conduction band state  $|C\rangle$ 

$$R_{V\to C} = \frac{2\pi}{\hbar} \left| \left\langle C \middle| \mathcal{H}^{(1)} \middle| V \right\rangle \right|^2 \delta \left[ E_C(\mathbf{k}) - E_V(\mathbf{k}) - \hbar \omega \right]. \tag{20}$$

The terms in  $E_{\rm C}(\mathbf{k})$  and  $E_{\rm V}(\mathbf{k})$  are the dispersion relations for the material at hand. Fig. 1 shows the band structure for Ge. The Dirac delta function highlights the absorption process at the bandgap energy  $[E_{\rm C}(\mathbf{k}) - E_{\rm V}(\mathbf{k})]$ . Solving the matrix element  $|\langle \mathbf{c}|\mathcal{H}^{(1)}|\mathbf{v}\rangle|$  involves working with Bloch functions for the states  $|\mathbf{V}\rangle$  and  $|\mathbf{C}\rangle$ . For a detailed explanation of this calculation see Ref. [81]. Without explicitly showing the details of the calculation, the matrix element is giving by

$$\left| \left\langle \mathbf{C} \middle| \mathcal{H}^{(1)} \middle| \mathbf{V} \right\rangle \right|^2 = \left( \frac{e}{2m\omega} \right)^2 \left| \mathbf{E} \right|^2 \left| P_{\text{CV}} \right|^2 \tag{21}$$

<sup>2</sup>This type of coupling between fields which involves only the charge distribution and not higher multipole moments of the charge distribution is known as **minimal coupling**.

In the Coulomb gauge the electric and magnetic fields are given by  $\mathbf{E} = -\frac{1}{c} \frac{\partial \mathbf{A}}{\partial t}$  and  $\mathbf{B} = \nabla \times \mathbf{A}$  respectively.

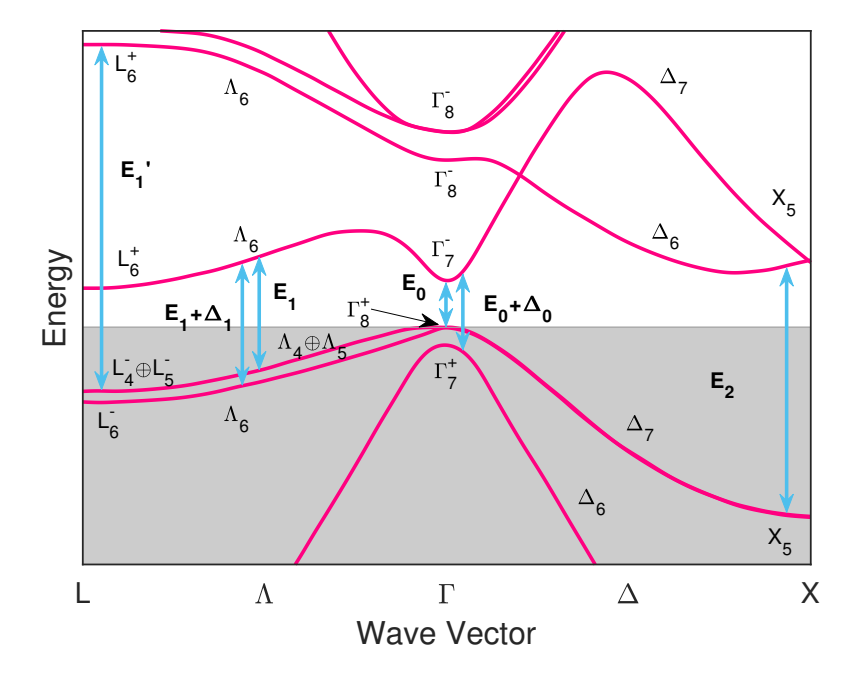


Figure 1: Band structure of Ge. The arrows indicate interband transitions of the critical points.

where  $|P_{\text{CV}}|^2$  is the average momentum matrix element. Substituting Eq. (21) in Eq. (20) and then into Eq. (18) we get the imaginary part of the dielectric function

$$\varepsilon_2(\omega) = \left(\frac{e}{m\omega}\right)^2 \sum_{\mathbf{k}} |P_{\text{CV}}|^2 \delta \left[E_{\text{c}}(\mathbf{k}) - E_{\text{v}}(\mathbf{k}) - \hbar\omega\right]. \tag{22}$$

We obtain the real part

$$\varepsilon_1(\omega) = 1 + \frac{\hbar^2 e^2}{m^2} \left[ \sum_{\mathbf{k}} \left( \frac{2}{E_{c}(\mathbf{k}) - E_{v}(\mathbf{k})} \right) \frac{|P_{cv}|^2}{(E_{c}(\mathbf{k}) - E_{v}(\mathbf{k}))^2 - \omega^2} \right]$$
(23)

from the Kramers-Kronig transformation of the imaginary part. We can rewrite Eq. (22) as

$$\varepsilon_2(\omega) = \frac{2\pi e^2}{\varepsilon_0 m \omega^2} |P_{\rm CV}|^2 J_{\rm CV},\tag{24}$$

where the joint density of states (JDOS) is defined as

$$J_{\text{CV}} = \frac{1}{8\pi^3} \int \frac{\mathrm{d}S_k}{|\nabla_k \left[ E_{\text{C}}(\mathbf{k}) - E_{\text{V}}(\mathbf{k}) \right]|}.$$
 (25)

where  $S_k$  is a constant energy surface  $E_{\rm C}(\mathbf{k}) - E_{\rm V}(\mathbf{k}) = \text{const.}$ 

An important feature arises when  $|\nabla_k [E_{\rm C}(\mathbf{k}) - E_{\rm V}(\mathbf{k})]| \approx 0$ . At such points,  $J_{\rm CV}$  becomes singular. These singularities in the JDOS (otherwise known as van Hove singularities) point to an increase in the transition rate between bands, and the energies at which they occur are labeled as critical points. The arrows in Fig. 1 indicate the transitions from the VBs to the CBs. induced by these singularities. In other words, where the gradient of the conduction band minus the valence band is approximately zero, interband transitions are more prominent. This happens at inflection points, local maxima or minima and where the bands run parallel to each other. These critical points will show up as absorption peaks and shoulders in the dielectric function of the material, namely in  $\varepsilon_2$ . Critical points are typically classified by dimensionality. By expanding the energy gap  $E_{\rm CV} = E_{\rm C}(\mathbf{k}) - E_{\rm V}(\mathbf{k})$  as[106]

$$\frac{1}{2} \left[ \frac{(k_1 - k_{0,1})^2}{m_1} + \frac{(k_1 - k_{0,2})^2}{m_2} + \frac{(k_1 - k_{0,3})^2}{m_3} \right], \tag{26}$$

gularity (0D) The singularity is localized at a single point, and it often leads to sharp peaks or discontinuities in the density of states. Line singularity (1D) can occur along specific lines in the Brillouin zone. This means that the singularity extends along a certain direction in the crystal momentum space. Surface singularity (2D) can also be associated with entire surfaces in the Brillouin zone. These are referred to as surface van Hove singularities and are related to changes in the topology of the Fermi surface. Volume singularity (3D) in rare cases, van Hove singularities can span a three-dimensional region in the Brillouin zone. This implies that the singularity is not confined to a specific direction but exists over a significant portion of the crystal momentum space. In the context of a diamond or zinc-blende structure, in three-dimensional space there are four kinds of singularities:

- $M_0$ : This is the center of the Brillouin zone. In both diamond and zincblende structures, it corresponds to the  $\Gamma$ -point. The coordinates of the  $\Gamma$ -point in the Brillouin zone are (0,0,0).
- $M_1$ : This is usually a high-symmetry point along a specific direction. In cubic systems such as diamond or zincblende, it is often associated with a point along the X direction  $\langle 1, 0, 0 \rangle$ .
- $M_2$ : Another high-symmetry point along a specific direction. In cubic sys-

tems, it is often associated with a point along the L direction (1, 1, 1).

•  $M_3$ : Yet, another high-symmetry point often associated with a point along the  $W \langle 1, 1, 0 \rangle$  direction in cubic systems.

### 2.3 Excitonic effects

The absorption of energy greater than the bandgap of a semiconductor, optically or otherwise, excites the electrons from the valence band into higher-energy states in the conduction band. In doing so, the electrons leave positively charged holes in the valence band. These newly created holes interact via the Coulomb force with the electrons in the conduction band. This interaction not only increases the probability of photon absorption, but can also lead to the formation of bound electron-hole pairs known as **excitons**. In the simplest picture, an exciton is a quasi-particle formed by an electron and a hole bound together in a hydrogen-like system.

There are two types of excitons:[2]

- Wannier-Mott excitons: Mainly observed in semiconductors, these excitons are free to move throughout the crystal, hence, they are also known as free excitons. Free excitons have a large enough radius to cover several unit cells.
- Frenkel excitons: Common in insulators and molecular crystals, these

excitons are tightly bound and localized within a single unit cell. They are sometimes referred to as tightly bound excitons.

In the present work, given that we are dealing with a semiconductor, we will focus only on Wannier-Mott excitons.<sup>3</sup> These quasi-particles, similar to a hydrogen atom, have a set of discrete energy states with a binding energy given by

$$R = \frac{\mu}{\varepsilon_{\rm st}^2} \text{Ry},\tag{27}$$

where  $\mu = (1/m_e + 1/m_h)^{-1}$  is the reduced mass of the electron-hole pair,  $\varepsilon_{\rm st}$  is the static dielectric constant of the material, and Ry= 13.6 eV is the Rydberg energy constant. The dispersion relations for excitons are[3]

$$E_{\text{ex}}(n, \mathbf{K}) = E_g - \frac{R}{n^2} + \frac{\hbar^2 |\mathbf{K}|^2}{2M}.$$
 (28)

In Eq. (28),  $E_g$  is the energy bandgap, R is the excitonic binding energy given in Eq. (53), and n,  $M = m_e + m_h$ , and  $\mathbf{K} = \mathbf{k}_e + \mathbf{k}_h$  are the principal quantum number, the total mass, and center of mass wave vector of the exciton, respectively. Figure 2 (a) shows the generation of en electron hole pair, as well as the continuum and the discrete energy states of the exciton. Figure 2 (b) shows the imaginary part of the dielectric function in the presence of excitons. The optical response of excitons

$$\varepsilon_2(E) = \frac{A}{E^2} \left[ \underbrace{\sum_{n=1}^{\infty} \frac{4\pi R^{3/2}}{n^3} \delta\left(E - E_g + \frac{R}{n^2}\right)}_{\text{Discrete}} + \underbrace{\frac{2\pi\sqrt{R}H(E - E_g)}{1 - e^{-2\pi\sqrt{R/(E - E_g)}}}}_{\text{Continuum}} \right], \quad (29)$$

<sup>&</sup>lt;sup>3</sup>Since we chiefly deal with Waninier-Mott excitons, we will refer to them as simply excitons.

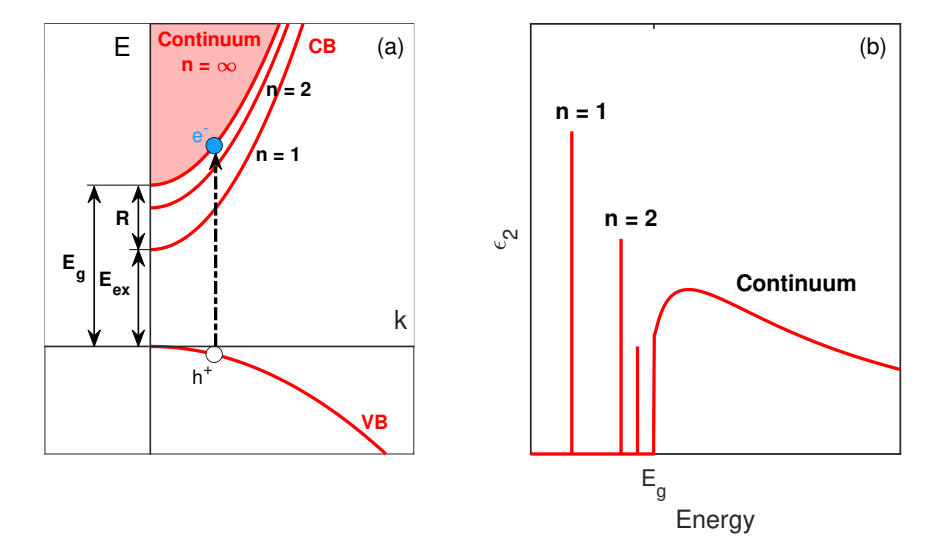


Figure 2: (a) Excitation of an electron-hole pair and formation of discrete exciton states below the conduction band. (b) Schematic of the imaginary part of the dielectric function, showing discrete absorption lines below the band edge and continuum absorption above  $E_g$ .

was first published by Elliot.[4] It incorporates the two absorption states, as seen in Figure 2 (b). The expression in Eq. (29) is only valid for 3-dimensional excitons. For 2-dimensional excitons, Shinado and Sugano give the following expression:[5]

$$\varepsilon_2(E) = \frac{A}{E^2} \left[ \sum_{n=0}^{\infty} \frac{4R}{(n+1/2)^3} \delta\left(E - E_g + \frac{R}{(n+1/2)^2}\right) + \underbrace{\frac{2H(E - E_g)}{1 - e^{-2\pi\sqrt{R/(E - E_g)}}}}_{\text{Continuum}} \right].$$
(30)

Both expressions present a similar form. The first term in Eq. (29) and Eq. (30) corresponds to discrete exciton states below the bandgap, each appearing as a delta-function-like resonance. These represent the bound states of the electron-

hole system. The second term represents continuum absorption by unbound, free carriers above the bandgap. The prefactor A affects the amplitude of both absorption states. The divergence near the band edge is known as **Sommerfeld** enhancement and arises due to Coulomb interaction between the carriers in the unbound regime.

### 2.4 Carrier dynamics

## 2.4.1 Ultrafast processes

In the absence of any external fields or strong optical excitations, the subsystem of particles and quasi-particles within the lattice structure of a semiconductor remains in thermal equilibrium. In a broad categorization, the distribution function of carriers and phonons in this equilibrium state can be described by Fermi-Dirac and Bose-Einstein statistics, respectively. Under certain circumstances, the behavior of both subsystems can also be approximated with Maxwell-Boltzmann statistics. If, however, the equilibrium state is disrupted, the carriers will go out of thermal equilibrium with the lattice, and their combined average momentum will be non-zero. Furthermore, the carrier temperature may not only differ from that of the lattice but also vary among carrier subspecies (electrons, holes, excitons). In the case of optical excitation, if the energy of the light source used is above the bandgap of the semiconductor, then the electrons are promoted from the VB to the CB, thereby leaving positively charged holes in their place. Once

these carriers populate the excited states in the bands, they will undergo several relaxation processes that will aid dissipate their corresponding excess energy and momentum. These processes occur on very short timescales that can be divided into four different overlapping regimes:[71]

- Coherent regime: Neither energy nor momentum have had any time to relax.

  Carriers have a strong coupling with the polarization of the electric field of the incident excitation radiation. Because of this coupling, the occupied states by the carriers are localized in energy and have a preferred direction in momentum space. Carriers will decohere from this regime within tens of femtoseconds.
- Non-thermal regime: After the coherence is broken, the distribution of the carriers is likely to be non-thermal (it cannot be described by a distribution function with a well defined temperature). Through different inelastic scattering processes, the carriers will establish a hot thermalized distribution.
- Hot-carrier regime: Once inelastic scattering processes take place, the momentum of the carriers will have dissipated and there will be no preferred direction in momentum space. However, since the excess energy of the carriers is yet to be dissipated, the occupied states are still localized in energy. The momentum-relaxed carriers can now be described by a distribution function. Still, the temperature of this distribution function is usually greater

than the lattice and might be different for each subspecies of carriers.

• Isothermal regime: Both energy and momentum begin to dissipate through elastic as well as inelastic scattering processes. The carriers are now in thermal equilibrium with the lattice. Diffusion and recombination of carriers takes place, either radiatively or non-radiatively.

Although the different scattering processes are the means of energy and momentum relaxation, it is only through scattering with the lattice that the carriers can relax in energy. Any other scattering process only redistributes energy among the different subspecies of carriers. [72] The excess energy of the carriers is given by [64]

$$E_e = \frac{\hbar \omega_{\text{pump}} - E_g}{1 - m_e/m_h} \tag{31a}$$

$$E_h = \hbar \omega_{\text{pump}} - E_g - E_e, \tag{31b}$$

where  $E_g$  is the bandgap energy,  $\hbar\omega_{\text{pump}}$  is the energy of the optical excitation source, m is the effective mass and the subscripts e and h stand for electrons and holes, respectively. By absorbing this excess energy, the carriers populate higher-energy states within the bands. As a consequence, the material's optical properties are modified in several ways.

# 2.4.2 Many-body effects

The presence of photo-excited carriers in the CB and VB modifies the energies of interband transitions. Exchange-correlation effects renormalize the bands and lower the transition energy of the bandgap and other critical points. On the other hand, due to phase-space filling, the chemical potential  $\mu$  of the bands varies with the charge carrier density n. An increase in photo-excited electrons raises the quasi-Fermi energy  $E_F^{(C)}$  above the CB minimum, while an increase in the hole population lowers the quasi-Fermi energy  $E_F^{(V)}$  below the VB maximum. These competing effects are described by [64, 73]

$$\overline{E}_{g} = \mu - E_{F} = E_{xc} + n \frac{dE_{xc}}{dn} - E_{F}, \tag{32}$$

where the over-line  $\overline{E}_g$  indicates the renormalized energy gap and  $E_F$  is the total quasi-Fermi level shift across the bands  $[E_F = E_F^{(C)} + E_F^{(V)}]$ . The chemical potential depends on the charge carrier density and the exchange-correlation energy, which is given by Vashishta and Kalia as[74]

$$E_{\rm xc} = \frac{a + br_s}{c + dr_s + r_s^2}. ag{33}$$

In Eq. (33),  $r_s$  is the exciton Bohr radius and the coefficients have the values a = -4.8316, b = -5.0879, c = 0.0152, and d = 3.0426. Renormalization lowers the energy of the gap and red-shifts interband transitions. Conversely, the filling of the bands with photo-excited carriers has the opposite effect and raises the

energies of these transitions. Since states at the absorption edge are unavailable, bandgap or critical point transitions need to occur higher up in the band. This is commonly known as a Moss-Burstein shift. [75, 76] Moreover, at sufficiently high carrier densities, the absorption of the material decreases due to the saturation of available states for interband transitions. In effect, the presence of photo-excited carriers within the bands will not only affect the energy of the transitions, but also decrease the absorption of the material.

# 2.4.3 Carrier diffusion

The last factor affecting the optical response of the material is the diffusion of carriers. In the case of optical excitation, excess carriers are generated only within the volume irradiated by the optical source. Once created, the carriers diffuse outside of this photo-excited volume. Therefore, the carrier density depends on both the penetration depth of the light source and the time after excitation. To get the initial concentration of carriers  $n_0$ , Richter et al.[67] give a simple expression for the upper charge carrier concentration limit based on simple assumptions:<sup>4</sup>

$$n_0 \approx \frac{E_{\text{pulse}}}{\hbar\omega} \left[1 - R(\theta, \omega)\right] \frac{4}{\delta\pi d_{\text{spot}}^2}.$$
 (34)

carriers are excited at the surface of the sample (as opposed to a homogeneous excitation), and therefore this concentration varies within the depth profile of the sample. Baron et al. [77, 78] expressed this concentration as a function of both of these factors n(x,t). Their study gives the profile of the carrier concentration at the surface where x = 0 as

$$n(t) = \frac{n_0}{4} \left[ \operatorname{erf} \left( \frac{t - \gamma_0}{\tau_0} \right) + 1 \right] e^{\alpha^2 D t - \frac{1}{\tau_1}} \operatorname{erfc} \left( \sqrt{\alpha^2 D t} \right), \tag{35}$$

where  $\alpha$  is the absorption coefficient, D is the diffusion coefficient,  $\tau_0$  and  $\tau_1$  are the relaxation time and characteristic recombination time respectively, and  $\gamma_0$  is the position of the inflection point of the error function.

The initial carrier density, although it decreases with time, remains approximately constant during the first few picoseconds. [69] Furthermore, if the penetration depth of our sample at the pump wavelength (the photoexcitation light source) is significantly greater than at the probing wavelength, the carrier density as a function of depth can be approximated as constant. Therefore, in the present work, given the timescale and photon energy range at which we are probing, we will only use Eq. (34) to estimate the carrier density and keep it constant throughout time. These assumptions are further validated by previous studies on carrier diffusion in highly excited bulk Ge. [79, 80]

### 3 EXPERIMENTAL METHODS

### 3.1 Spectroscopic Ellipsometry

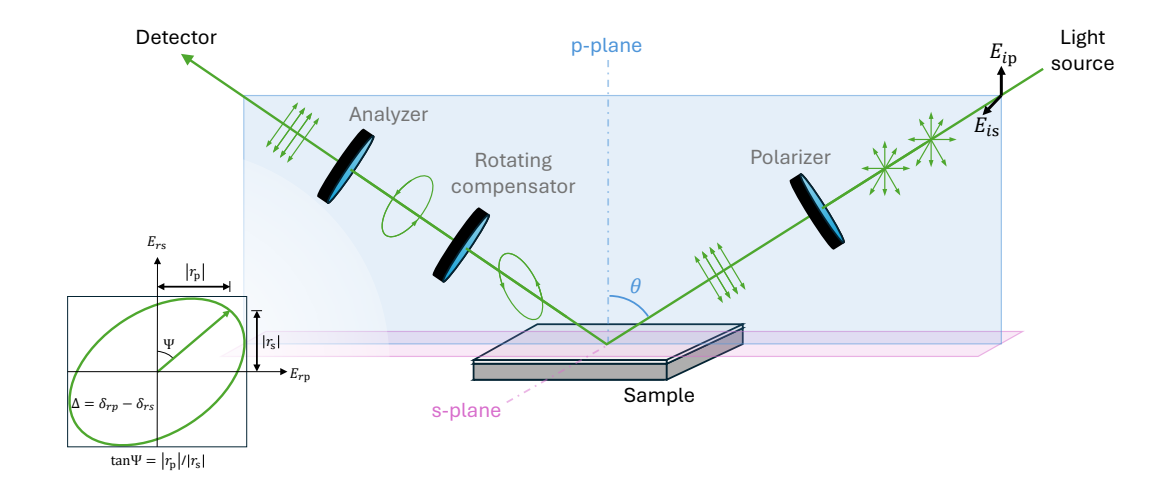


Figure 3: Schematic of a rotating compensator ellipsometry setup. The unpolarized light has an angle of incidence  $\theta$ , and its path comprises a polarizer, sample stage, rotating compensator, and analyzer.

Spectroscopic ellipsometry is an optical technique used to characterize the optical functions of bulk materials and thin films. To do this, an ellipsometer measures the reflectance of the material while modulating the polarization of both, the incident and reflected beam of light. Figure 3 shows the schematic for a rotating compensator ellipsometry (RCE) experiment. The basic procedure for this setup is to send unpolarized light through the following stages: a polarizer, the sample, a rotating compensator, an analyzer, and the detector (this configuration is denominated PSC<sub>R</sub>A). Initially, the incident beam of light of known intensity

 $I_0$  is polarized at angle P with respect to the p-plane (plane of incidence). This polarized pulse will have two components: One parallel to the plane of incidence denoted as p-wave, and a second component perpendicular to this plane, which is labeled as s-wave. Their corresponding amplitudes are  $E_p$  and  $E_s$ , respectively. After this polarization stage, the incident beam is reflected by the sample at an angle of incidence (AOI)  $\theta$ . The reflected light then propagates through a rotating compensator (a rotating retarder) and analyzer (another polarizer), before finally being detected. Since this is a RCE setup, the polarizer and analyzer are fixed in place while the compensator is the only optical element that varies its axis. This compensator introduces a phase-shift  $\delta$  between the p- and s-components of the polarized light. The final reflected intensity I is measured at several compensator angles C. Using Jones vectors and matrices to describe the state of polarization of the light  $\mathbf{L}$ , the polarization state outcome for this PSC<sub>R</sub>A configuration is [19]

$$\mathbf{L}_{\text{out}} = \mathbf{AR}(A)\mathbf{R}(-C)\mathbf{CR}(C)\mathbf{SR}(-P)\mathbf{PL}_{\text{in}},\tag{36}$$

where **A** and **P** are polarizer matrices, **C** is a retarder matrix,  $\mathbf{R}(\theta)$  is a rotation matrix by angle  $\theta$ , and the subscripts out and in stand for the final and incident polarization states, respectively. A Jones vector gives the polarization of the electric field **E**. However, since what is measured in practice is the light intensity I = |E|, it is convenient to work with Stokes vectors **S** and Mueller matrices **M**.

In this Mueller calculus formalism, the state of polarization is [87]

$$\mathbf{S}_{\text{out}} = \mathbf{M}_A \mathbf{R}(A) \mathbf{R}(-C) \mathbf{M}_C \mathbf{R}(C) \mathbf{M}_S \mathbf{R}(-P) \mathbf{M}_P \mathbf{S}_{\text{in}}, \tag{37}$$

where the subscripts A, C, and P, stand for analyzer, compensator, and polarizer, respectively. The subscripts in and out have the same meaning as in Eq. (36). Following Eq. (37), the intensity detected as a function of the compensator angle has the form [88]

$$I(C) = I_0 (\alpha_0 + \alpha_2 \cos 2C + \beta_2 \sin 2C + \alpha_4 \cos 4C + \beta_4 \sin 4C), \qquad (38)$$

where components have the explicit form[88]

$$\alpha_0 = \frac{1 + \cos \delta}{2} \left( \cos 2A \cos 2P - \cos 2P \cos 2\Psi + \sin 2A \sin 2P \sin 2\Psi \cos \Delta \right) - \cos 2A \cos 2\Psi + 1,$$
(39a)

$$\alpha_2 = -\sin 2A \sin 2P \sin \delta \sin 2\Psi \sin \Delta, \tag{39b}$$

$$\beta_2 = \sin 2A \cos 2P \sin \delta \sin 2\Psi \sin \Delta, \tag{39c}$$

$$\alpha_4 = \frac{1 - \cos \delta}{2} \left( \cos 2A \cos 2P - \cos 2P \cos 2\Psi - \sin 2A \sin 2P \sin 2\Psi \cos \Delta \right), \tag{39d}$$

and 
$$\beta_4 = \frac{1 - \cos \delta}{2} \left( \cos 2A \sin 2P - \sin 2P \cos 2\Psi + \sin 2A \cos 2P \sin 2\Psi \cos \Delta \right)$$
. (39e)

In Eq. (39),  $\delta$  refers to the phase shift induced by the rotating compensator.  $\Psi$  and  $\Delta$ , on the other hand, are the angle and phase shift between the p- and s-components, respectively (see the lower-left corner of Figure 3). Standard practice calls for the polarizer angle  $P=45^{\circ}$ , while the analyzer is set either  $A=\pm45^{\circ}$ .

To solve for the ellipsometric angles  $\Psi$  and  $\Delta$ , we note that Eq. (38) has the form of a Fourier series, where its coefficients refer to Eq. (39). We can solve for the explicit values of the coefficients by fitting the first five terms of a Fourier series to Eq. (38) (one term for each coefficient in Eq. (39)). Hence, the need for several measurements at different compensator angles (at least five for RCE).[89] If we know the values of the coefficients  $\alpha_i$  and  $\beta_i$  in Eq. (39), the ellipsometric angles have the form

$$\tan 2\Psi = -\frac{\sqrt{(\alpha_2^2 + \beta_2^2)(1 - \cos \delta)^2 / \sin^2 \delta + 4(-\alpha_4 \sin 2P + \beta_4 \cos 2P)^2}}{2(\alpha_4 \cos 2P + \beta_4 \sin 2P)},$$
(40a)

and 
$$\tan \Delta = \left(\frac{1 - \cos \delta}{2 \sin \delta}\right) \frac{\alpha_2 \sin 2P - \beta_2 \cos 2P}{\alpha_4 \sin 2P - \beta_4 \cos 2P}.$$
 (40b)

In the case of negative  $\tan 2\Psi$  values, a correction of  $+\pi/2$  to the  $\Psi$  value will be needed. The information of these ellipsometric angles can be expressed in a single complex variable

$$\rho = \tan \Psi e^{i\Delta} = \frac{r_{\rm p}}{r_{\rm s}},\tag{41}$$

known as the fundamental equation of ellipsometry. In Eq. (41),  $r_{\rm p}$  and  $r_{\rm s}$  are the complex p- and s-wave reflection coefficients, respectively. Explicitly stated,  $\tan \Psi = |r_{\rm p}|/|r_{\rm s}|$  is the ratio of the electric field amplitudes of the reflected waves.  $\Delta$ , on the other hand, is the change in the phase difference of the p- and s-waves induced by the reflection from the sample. Stated differently, if  $\delta_1$  is the p-s phase difference before light interacts with the sample and  $\delta_2$  is the p-s phase difference after reflection, then  $\Delta = \delta_1 - \delta_2$ . Once the complex quantity  $\rho$  in Eq. (41)

has been calculated, it can be used to obtain the optical constants of the sample via[90]

$$\langle \varepsilon \rangle = \langle n \rangle^2 = \sin^2 \theta \left[ 1 + \tan^2 \theta \left( \frac{1 - \rho}{1 + \rho} \right) \right].$$
 (42)

If the sample of interest were an ideal bulk specimen, then Eq. (42) would describe the actual complex DF  $\varepsilon$  (or complex index of refraction n) of the material. In practice, however, this is rarely the case. In most cases, we deal with less-than-ideal samples where surface roughness and back-side reflections cannot be ignored. In such scenarios, we refer to  $\langle \varepsilon \rangle$  as the pseudo-DF (or pseudo-index of refraction  $\langle n \rangle$ ) because it describes the optical behavior of the sample as a whole, rather than the optical response of the individual material of interest. The distinction between  $\varepsilon$  and  $\langle \varepsilon \rangle$  is particularly relevant when dealing with multi-layered samples. While in bulk samples the pseudo-DF might present similar features to the DF, the pseudo-DF can look completely different in samples composed of two or more films. In general, extracting  $\varepsilon$  from  $\langle \varepsilon \rangle$  requires extensive modeling of the optical functions of the different films, as well as an estimation of their corresponding thicknesses. It is only after this process of adjusting parameters to fit the experimental data that one is able to obtain the desired optical functions.

### 3.2 Broadband Femtosecond Ellipsometry

Figure 4 shows the femtosecond ellipsometry configuration. The Coherent Astrella (35 fs, max. 6mJ) laser emits pulses of 800 nm wavelength at 1 kHz repetition

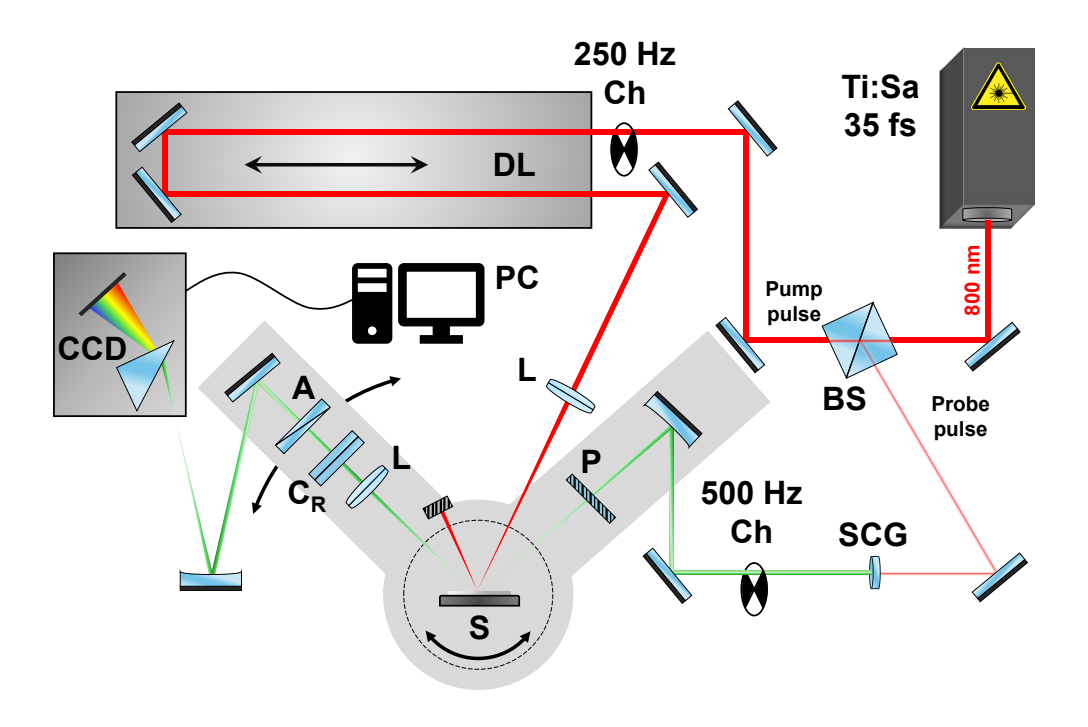


Figure 4: Schematic of the broadband femtosecond spectroscopic ellipsometry setup. A beam splitter **BS**) splits the initial (35 fs and 800 nm wavelength) pulse into the pump and probe. In the pump path, the pulse goes through a 250 Hz chopper **Ch**, the delay line **DL**, a focusing lens **L**, and the sample **S**. On the probe path, the pulse is redirected to CaF<sub>2</sub> plate that transforms the infrared pulse into white light via supercontinuum generation (**SCG**). This white light probe pulse then goes trough a **PSC**<sub>R</sub>**A** (polarizer, sample, rotating compensator, and analyzer) ellipsometry configuration stage, before hitting the **CCD** detector. rate.[91] This beam is then divided into the pump and probe pulses. The pump pulse is directed to a 250 Hz chopper before propagating through the delay line (**DL**). The temporal resolution of the **DL** is about 3 fs and is capable of up to a

6.67 ns pump-probe delay. After the **DL**, the beam is directed toward a focusing mirror, which adjusts the pump beam-spot diameter before it reaches the sample stage **S**. By adjusting this beam-spot, we are able to modulate the number of photons per unit area. The probe pulse, on the other hand, is focused by a lens onto a  $CaF_2$  plate, which generates white light from the initial IR pulse by means of supercontinuum generation (**SCG**). This probe pulse has a spectral range of 1.3 to 3.6 eV and accounts for only about 1  $\mu$ J of the energy of the original laser pulse. After passing through a 500 Hz chopper, the probe then goes through the conventional RCE stage in a PSC<sub>R</sub>A configuration. Polarizer and analyzer are set 90° from each other (+-, -+, --, and ++ are the possible configurations). The compensator will typically rotate for a total of 36 different angles. Finally, the probe pulse is dispersed by a prism before arriving to the CCD detector.

As it is the case in typical pump-probe spectroscopy setups, the measured signal is not the same as in the steady state case (in our case, the ellipsometric angles  $\Psi$  and  $\Delta$ ), but rather the reflectance-difference spectra  $\Delta R(E, \Delta t)$ . This reflectance-difference spectra is not only a function of wavelength (or photon energy E), but of time delay  $\Delta t$  as well. As depicted in Figure 7, the choppers of this setup create four intensity signals: Pump+probe,  $pump\ only$ ,  $probe\ only$ , and dark (we labeled these different intensities P1, P2, P3, and P4, respectively). The

four measured intensities are related to the reflectance-difference by

$$\frac{\Delta R(E, \Delta t)}{R^0(E)} = \frac{R^{\rm p}(E, \Delta t) - R^0(E)}{R^0(E)} = \frac{R^{\rm p}(E, \Delta t)}{R^0(E)} - 1 \equiv \frac{I_{\rm P1} - I_{\rm P2}}{I_{\rm P3} - I_{\rm P4}} - 1. \tag{43}$$

In Eq. (43),  $R^{\rm p}(E,\Delta t)\equiv I_{\rm P1}(E,\Delta t)-I_{\rm P2}(E,\Delta t)$  is the background-corrected

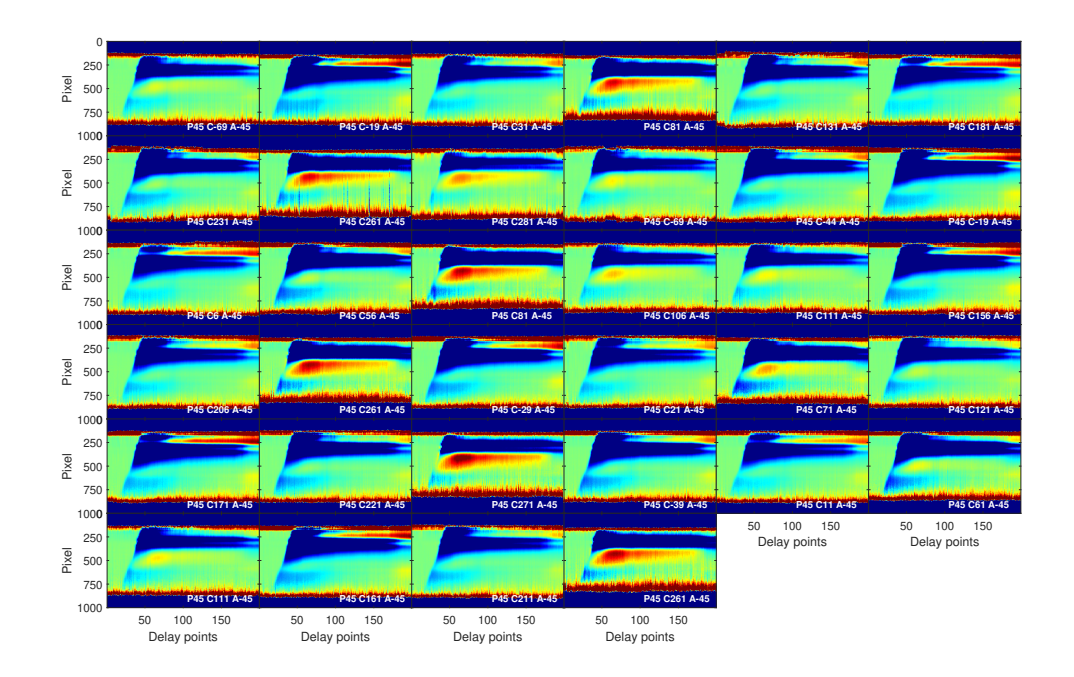


Figure 5: Reflectance-difference spectra recorded for each compensator angle. The y-axis shows detector pixel index (proportional to wavelength), and the x-axis shows the delay steps. Compensator, polarizer, and analyzer angles are indicated in the lower right corner of each panel.

pump+probe spectra and  $R^0(E) \equiv I_{P3}(E,\Delta t) - I_{P4}(E,\Delta t)$  is the probe only spectra. In effect, the recorded data consist of a series of reflectance difference intensities as a function of wavelength and delay time. Each intensity entry corresponds

to a set angle of the compensator. Figure 5 presents a total of 34 measurements at different compensator angles. The reflectance difference is displayed as a function of wavelength on the y-axis (the figure shows the number of pixel in the detector, rather than the wavelength or energy value) and delay time on the x-axis (the axis ticks correspond to the number of recorded delay point and not to actual delay time). The compensator, polarizer, and analyzer angles are indicated in white font at the bottom right corner of each measurement. Given that  $180^{\circ}$  constitutes a complete compensator cycle, notice that some of the recorded angles are redundant. This allows a direct comparison of the same angle after a certain amount of time, to ensure that the signal did not degrade over time.

Due to the dispersion of the  $CaF_2$ , the SCG stage induces a spectral chirp to the recorded intensity. To correct for the chirping in the probe pulse, we used a retroactive correction. The zero-delay for each energy channel is determined by fitting a polynomial to the energy dependence of the chirp, as shown in Figure 6. This fit was applied to selected Mueller matrix components (N, C, and S), which are explained below.

After the chirp correction, we use the reflectance-difference to obtain the intensity of Eq. (38) with the expression

$$I(E, \Delta t) = I^{0}(E) \left[ 1 + \left( \frac{\Delta R(E, \Delta t)}{R^{0}(E)} \right) \right], \tag{44}$$

where  $I^0(E)$  is the pseudo-intensity spectra computed using  $\Psi^0(E)$  and  $\Delta^0(E)$ 

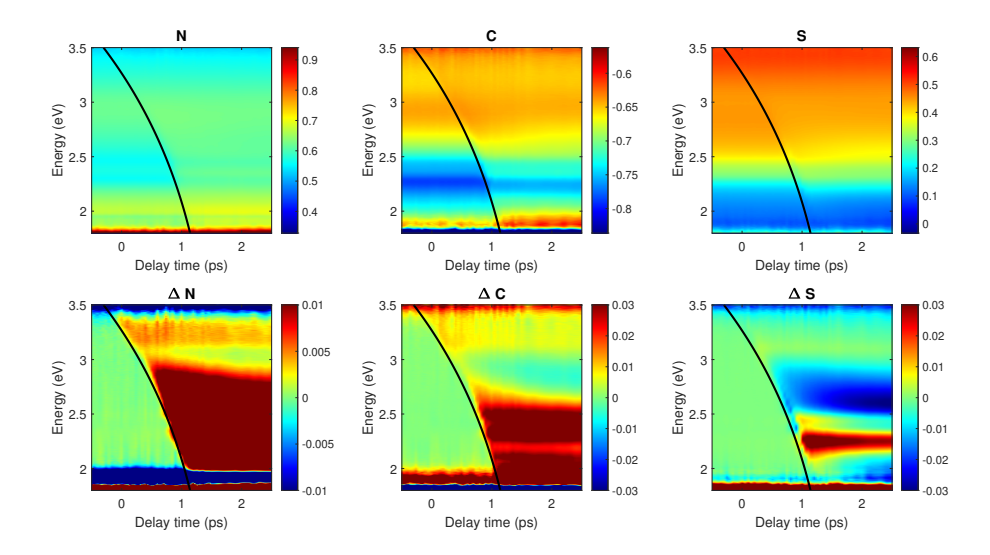


Figure 6: The spectral chirp correction polynomial (black line) fitted to the N, C, and S elements of the sample Mueller matrix. For reference, the differences of these matrix elements relative to their steady-state values,  $\Delta N$ ,  $\Delta C$ , and  $\Delta S$  are also shown.

from a reference steady-state ellipsometry measurement of the sample of interest. Using this intensity, we can obtain the Mueller matrix of the sample  $\mathbf{M}_S$  of Eq. (37) by the Moore-Penrose pseudo-inversion formalism.[66] The final Mueller matrix for an isotropic sample is given as

$$\mathbf{M}_{S} = \begin{bmatrix} 1 & -N & 0 & 0 \\ -N & 1 & 0 & 0 \\ 0 & 0 & C & S \\ 0 & 0 & -S & C \end{bmatrix}$$

$$= \begin{bmatrix} 1 & -\cos 2\Psi & 0 & 0 \\ -\cos 2\Psi & 1 & 0 & 0 \\ 0 & 0 & \sin 2\Psi \cos \Delta & \sin 2\Psi \sin \Delta \\ 0 & 0 & -\sin 2\Psi \sin \Delta & \sin 2\Psi \cos \Delta \end{bmatrix}. \tag{45}$$

We can use Eq. (45) to obtain the ellipsometric angles in terms of the sample

Mueller matrix components in the following form:

$$\Psi = \frac{1}{2}\arctan\left(\frac{\sqrt{C^2 + S^2}}{N}\right) \tag{46a}$$

$$\Delta = \frac{1}{2}\arctan\left(\frac{S}{C}\right). \tag{46b}$$

Once the ellipsometric angles are known, we can use Eq. (42) to obtain the pseudo-DF as a function of delay-time and energy.

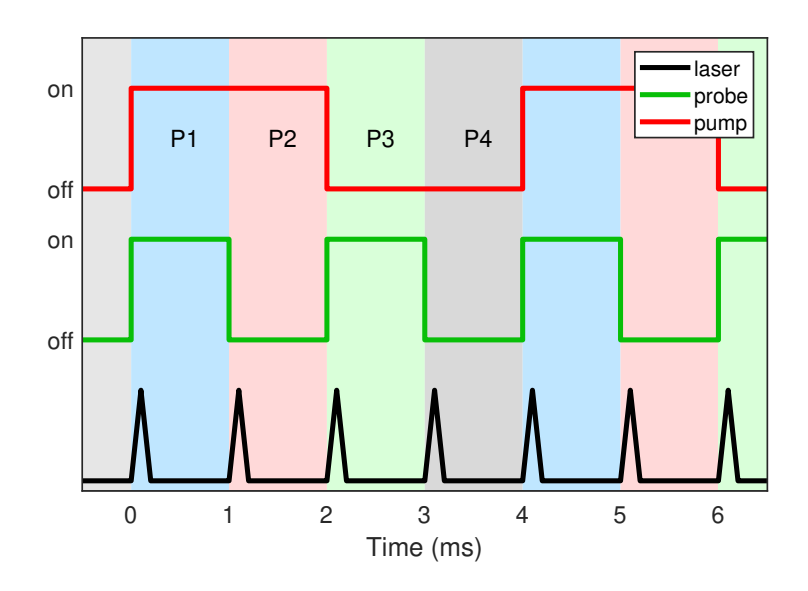


Figure 7: The two choppers of the femtosecond setup give rise to four different intensities. P1: Pump+probe, P2: Pump only, P3: Probe only, and P4: Dark.

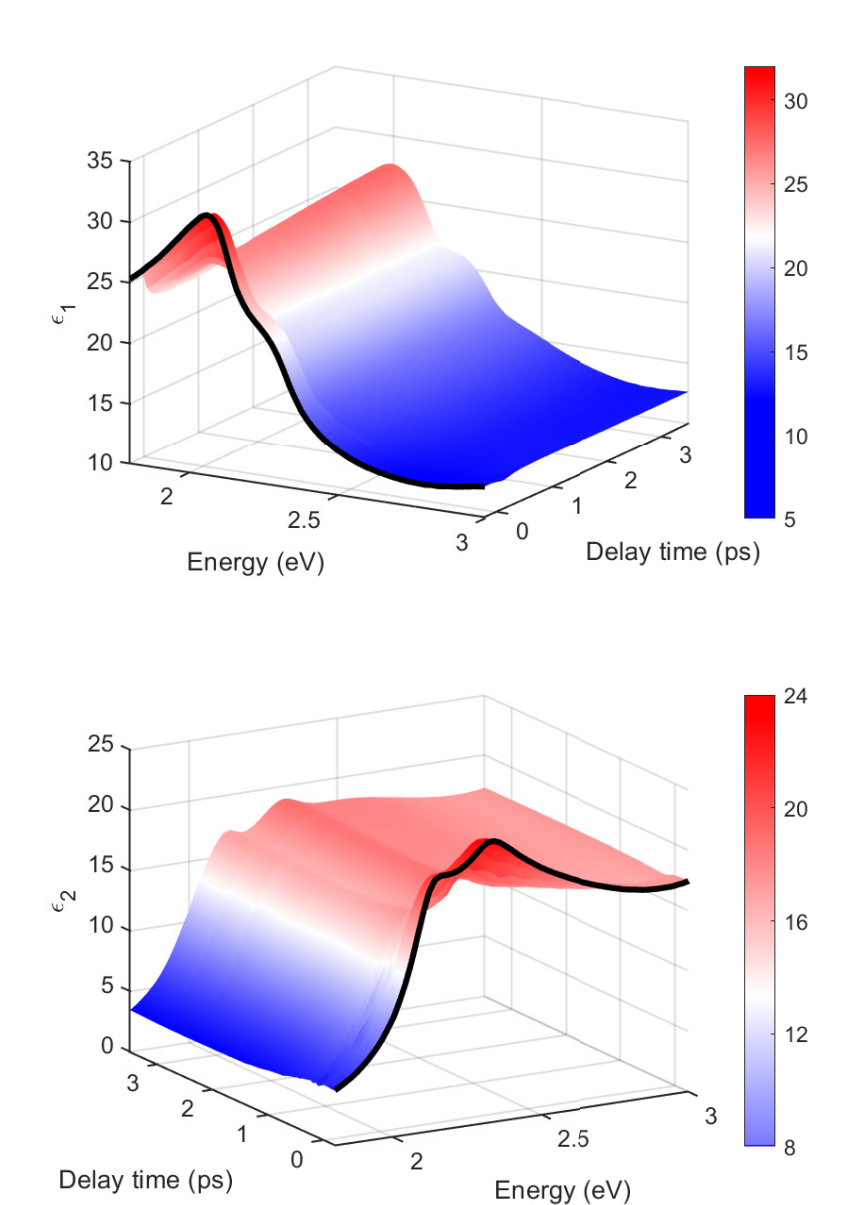


Figure 8: Real (left) and imaginary (right) part of the point-by-point dielectric function fit as a function of energy from 1.8 eV to 3 eV and delay-time from -0.25 ps to 3.5 ps.

Because we are interested in only the bulk material, it is necessary to correct for the oxide overlayer that is present at the moment of the measurement. To make this oxide correction, we can use the optical properties of  $GeO_2$  published by Nunley et al.[33] The procedure consists of simulating the pseudo-DF using Nunley's  $GeO_2$  and Emminger's parametric semiconductor oscillator models.[33, 32] In this manner, we construct a point-by-point fit that extracts the DF of the bulk material and removes any effects from the oxide layer. We achieved this with the aid of the commercial software WVASE32, from the J. A. Woollam company.[92]

A sample of bulk Ge was measured at an AOI of 65° and with p-polarization state for the pump. Delay times ranged from -5 ps to 1 ns with varying step size. The smallest step size measured was 50 fs (from -0.5 ps to 1.5 ps). The total number of 34 compensator angles were measured. Figure 8 shows the real and imaginary part of  $\epsilon$  on an energy range of 1.8 eV to 3 eV. To overcome statistical fluctuations, about 400 reflectance-difference spectra per data point (after clearing outliers) are averaged.

Figure 9 shows pictures of the most important part of the experimental setup:
(a) the delay line, (b) the SCG stage, where the CaF<sub>2</sub> plate and one of the choppers are pointed out, and (c) the spectroscopy ellipsometry stage. From the pointed components, it can be seen in the last picture that the ellipsometry stage is in a RCE configuration, as previously stated. Additionally, the picture also shows the

focusing lens for the pump beam, which is used to adjust the beam diameter.

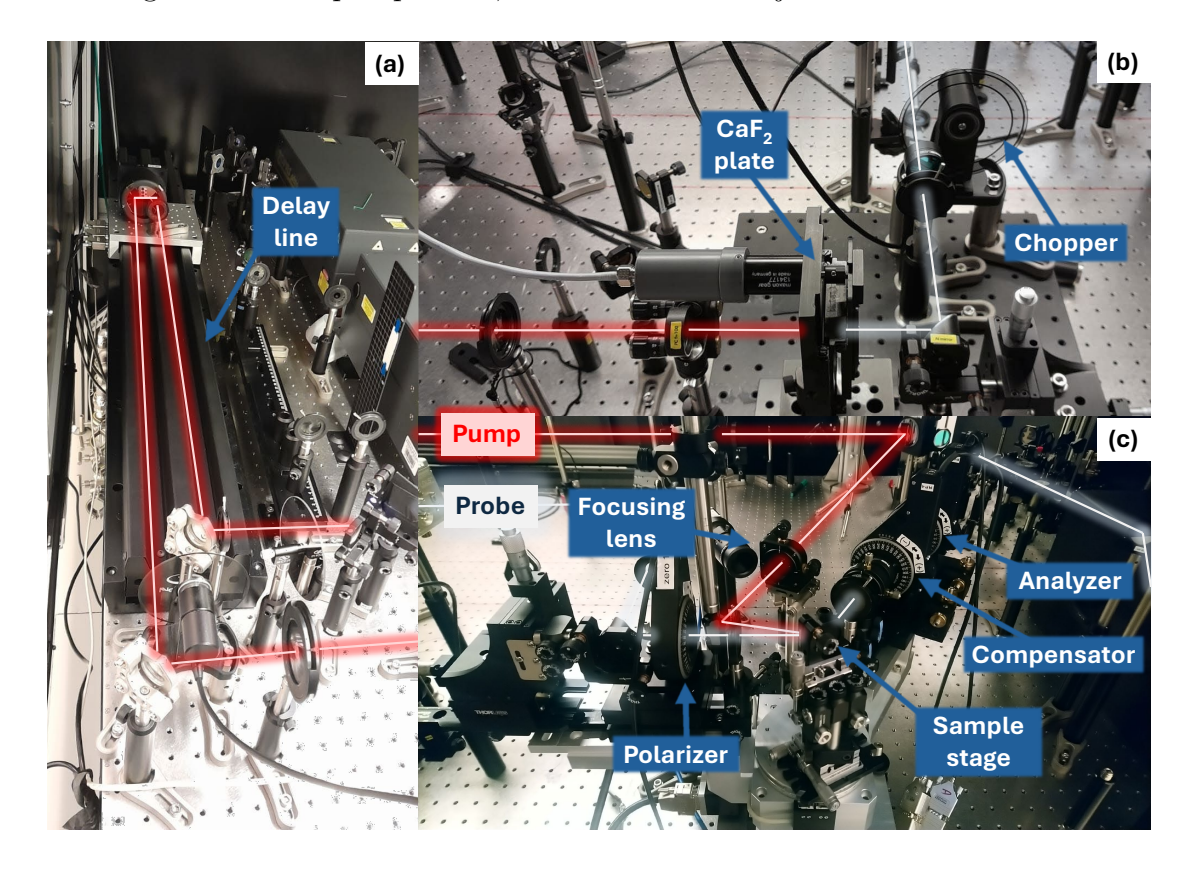


Figure 9: Photographs of key components of the experimental setup: (a) the delay line, (b) the supercontinuum generation stage, and (c) the spectroscopic ellipsometry stage. In each panel, the red line indicates the 800 nm pump beam path, while the white line traces the probe beam path.

# 4 MODELING THE STEADY-STATE DIELECTRIC FUNCTION OF GE

### 4.1 Two-dimensional excitons

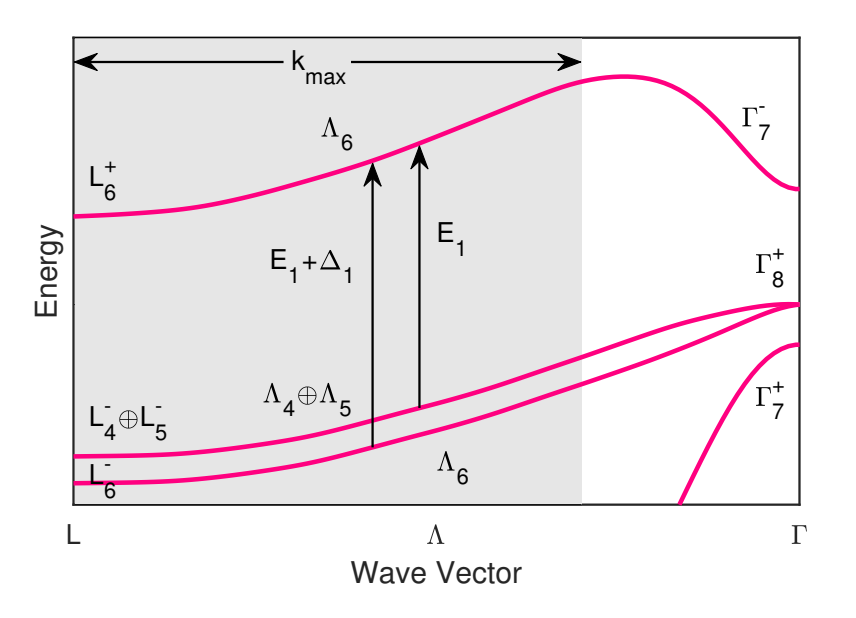


Figure 10: Band structure of Ge in the  $\Lambda$ -direction, where the  $E_1$  and  $E_1 + \Delta_1$  transitions (black arrows) are located. The range of wave vectors  $\mathbf{k}$  where these transitions take place is labeled  $k_{\text{max}}$  (grey region).

The electronic band structure of Ge presents two van Hove singularities in the [111]-direction ( $\Lambda$ ) of the wave vector  $\mathbf{k}$  in the Brillouin zone (see Fig. 10).[81] These critical points (CPs) arise due to the conduction band (CB) running parallel to the valence band (VB) over a certain range of  $\mathbf{k}$ -vectors. Labeled as  $E_1$  and  $E_1 + \Delta_1$ , these CPs are transitions occurring from the heavy-hole (hh) and light-

hole (lh) VBs to the CB, respectively. Categorized[81, 13] as a two-dimensional minimum critical point  $M_0$ , the literature gives the dielectric function (DF) versus photon energy  $\varepsilon(E)$  for such CPs as[14, 15, 16, 18, 17]

$$\varepsilon(E) = C - Be^{i\phi} \ln(E - E_1 + i\Gamma), \tag{47a}$$

with 
$$\frac{\mathrm{d}^2 \varepsilon(E)}{\mathrm{d}E^2} = \frac{Be^{i\phi}}{(E - E_1 + i\Gamma)^2}$$
. (47b)

In CP analysis, typically only Eq. (47b) is fitted to the data with amplitude B, phase angle  $\phi$ , energy  $E_1$ , and broadening  $\Gamma$  as its free parameters.[19] Variable C in Eq. (47a) is a constant. Unfortunately, this type of analysis only provides information about the energy and broadening for the structures of interest, while leaving the form of the DF without an accurate description. Eq. (47a) does not yield a good description of the dielectric function or the CP parameters.[20]

Conversely, in cases where the calculation of the DF has been attempted, the description of this CP lineshape has been limited to a qualitative discussion.[106, 107] A major pitfall in these calculations is the omission of the Coulomb interaction between the electrons excited to the CB and the holes left in the VB. These electron-hole pairs tend to form excitons (bound together in a hydrogen-like system). Because of the joint density of states (JDOS) of these transitions, the excitonic systems for  $E_1$  and  $E_1 + \Delta_1$  are confined to a two-dimensional plane. Equation (78) shows the JDOS for the  $E_1$  CP in a coordinate system where the

z-axis points along the [111]-direction. Naturally, in this coordinate system, the x- and y-axis would be along the [1 $\overline{1}0$ ]- and [11 $\overline{2}$ ]-direction, respectively.

$$J_{\rm CV}(E) \propto \int \frac{\mathrm{d}\mathbf{k}}{8\pi^3} \delta \left[ E_1 + \frac{\hbar^2}{2} \left( \frac{k_x^2 + k_y^2}{\mu_\perp} + \frac{k_z^2}{\mu_\parallel} \right) - E \right]. \tag{48}$$

The longitudinal reduced effective mass  $\mu_{\parallel}$  in Eq. (78) is significantly greater than the transverse reduced effective mass  $\mu_{\perp}$ .[107] As a result, the JDOS effectively confines the motion of the exciton to the x-y plane, as depicted in Fig. 11.

In essence, an accurate description of the aforementioned CPs must take into account the effects of the formation of these quasi-two-dimensional excitons. In recent years, great progress has been made in the implementation of the GW-method and the Bethe-Salpeter equations (BSE) to calculate the DF of different semiconductors.[22, 23, 24] This approach accounts for excitons by making quasi-particle energy corrections to the initial density functional theory calculations of the band structure. It also accounts for the Sommerfeld enhancement of excitonic absorption over the absorption by uncorrelated electron-hole pairs. Barker et al.,[23] for instance, correctly resolve the  $E_1$  and  $E_1 + \Delta_1$  CPs in the DF of GaSb. Unfortunately, this approach requires a significant amount of computing time and provides only limited agreement when compared with experiment. Instead, we aim to provide a closed-form expression for the DF that can easily be implemented on a personal computer.

Culminating prior efforts of finding a solution to this problem, [5, 25] Tanguy

provided an expression for the complex DF that incorporates the effects of twodimensional Wannier excitons.[26] Unlike GW-BSE, which requires large computational resources and provides only an approximation to the DF, Tanguy's model offers a fully analytical solution. [26] This allows for direct comparison with experimental data without the need for extensive numerical fitting. Still, despite Tanguy's work being published almost three decades ago, [26] comparison of theory with experiment is lacking in the literature. In the present work, we will bridge this gap by comparing Tanguy's model to the DF of Ge near the  $\mathcal{E}_1$  and  $E_1 + \Delta_1$  CPs. This model not only provides a better description of the DF than previous attempts, but also requires no fitting parameters apart from energy and broadening. Furthermore, having a reduced number of fitting parameters makes this model highly applicable to other areas of research, such as the description of band-filling effects [108, 109] and ultrafast phenomena. [68, 30, 31] Because of its compact form, the model can also be applied to other semiconductor materials of interest, such as InSb, GaAs, and  $Ge_{1-x}Sn_x$  alloys.

For comparison with experiment, we used data published by Emminger et al., [32] which comprises a temperature series of spectroscopic ellipsometry measurements, ranging from 4 to 800 K. We will briefly discuss the acquisition, reduction, and modeling of the data. We will also analyze Tanguy's DF expression, as well as how it can be adapted to the material of interest. The fixed parameters of the model tend to change with temperature, hence we will discuss the temperature

dependence of both, the fixed and free parameters. Finally we will point out the shortcomings of the model and how they can be improved upon.

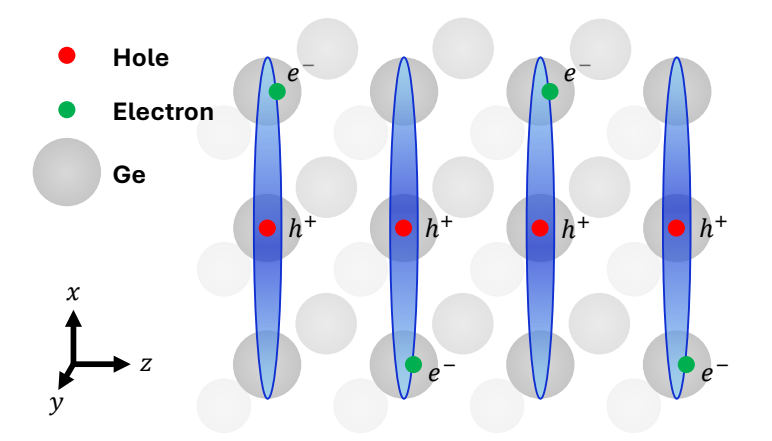


Figure 11: Because the longitudinal reduced mass  $\mu_{\parallel}$  is much larger than the transverse reduced mass  $\mu_{\perp}$  in the CPs  $E_1$  and  $E_1 + \Delta_1$ , the excitons are restricted to the plane perpendicular to the z-axis.

### 4.2 Experimental data

The experimental data consist of spectroscopic ellipsometry measurements of a wafer of bulk Ge with (100) surface orientation. With a separation of 10 meV, the data collected ranged from 0.7 to 6.3 eV. There were a total of 32 measurements ranging from 4 to 800 K. We will not discuss the details of these measurements any further. If interested in more information about the cleaning procedure, acquisition settings, and temperature control methods, we encourage the reader to look at the original publication. [32]

What is relevant for our purposes is the effect of the native oxide layer embedded in the data. Because we are interested in only the bulk material, it is necessary to correct for the oxide overlayer that is present at the moment of the measurement. To make this oxide correction, we can use the optical properties of GeO<sub>2</sub> published by Nunley et al.[33] The procedure consist of simulating the pseudo-DF using Nunley's GeO<sub>2</sub> and Emminger's parametric semiconductor oscillator models.[33, 32] In this manner, we construct a point-by-point fit that extracts the DF of the bulk material and removes any effects from the oxide layer. We achieved this with the aid of the commercial software WVASE32, from the J. A. Woollam company.[92] We note that the oxide layer thickness varied slightly at each temperature. Therefore, there could be small errors in the layer thickness estimated by this oxide correction. If the wrong oxide thickness is used, it could lead to surface effects that will affect the amplitude of the imaginary part of the DF. We will expand on these surface effects in Sec. 4.5.

### 4.3 Tanguy model

At a two-dimensional CP with energy  $E_1$ , Tanguy[26] provides the optical dispersion for a two-dimensional exciton by incorporating broadening to both, the continuum and discrete absorption spectra. This complex DF is given by[26]

$$\varepsilon(E) = \frac{A}{\pi(E + i\Gamma)^2} \left\{ g_a \left[ \xi(E + i\Gamma) \right] + g_a \left[ \xi(-E - i\Gamma) \right] - 2g_a \left[ \xi(0) \right] \right\}, \tag{49}$$

where

$$A = \frac{e^2 \mu_{\perp} |\mathbf{e} \cdot \mathbf{M}_{\text{CV}}|^2}{\pi \varepsilon_0 m_0^2}, \, \xi(z) = \sqrt{\frac{R}{E_1 - z}}, \tag{50a}$$

and 
$$g_a(\xi) = 2\ln(\xi) - 2\psi\left(\frac{1}{2} - \xi\right)$$
. (50b)

In Eq. (74), the amplitude A depends on the electron charge e, the free electron mass  $m_0$ , the permeability of free space  $\varepsilon_0$ , the reduced mass of the twodimensional exciton  $\mu_{\perp}$ , and the transition matrix element  $\mathbf{e} \cdot \mathbf{M}_{\text{CV}}$ , whereas the argument  $\xi$  depends on the exciton's binding energy R and the CP energy  $E_1$ . In Eq. (50b),  $\psi(z)$  is the complex digamma function

$$\psi(z) = \frac{\mathrm{d}}{\mathrm{d}z} \ln \Gamma(z) = \frac{\mathrm{d}}{\mathrm{d}z} \ln \left( \int_0^\infty t^{z-1} e^{-t} \mathrm{d}t \right), \tag{51}$$

where  $\Gamma(z)$  is the complex gamma function. In the case of the CPs  $E_1$  and  $E_1 + \Delta_1$  of Ge, we can replace the amplitude in Eq. (73) with [106, 108, 109]

$$A^{(E_1)} = \frac{4e^2 \mu_{\perp}^{(E_1)} \overline{P}^2}{3\pi \varepsilon_0 m_0^2} k_{\text{max}} \text{ for } E_1$$
 (52a)

and 
$$A^{(E_1 + \Delta_1)} = \frac{4e^2 \mu_{\perp}^{(E_1 + \Delta_1)} \overline{P}^2}{3\pi \varepsilon_0 m_0^2} k_{\text{max}} \text{ for } E_1 + \Delta_1,$$
 (52b)

where  $\mu_{\perp}^{(E_1,E_1+\Delta_1)}$  are the transverse reduced masses of the CPs,  $\overline{P}$  is the average transition matrix element, and  $k_{\text{max}}$  is the maximum range along the  $k_z$ -axis where interband transitions take place. For details about these amplitudes, refer to Appendix B. Previous calculations of the DF for these CPs neglected the correlation between electrons and holes, resulting in a step-like function[106, 107, 108, 109] [see Eq. (107) in Sec. B of the Appendix for details on this step function].

To illustrate these excitonic effects, Fig. 12 shows the comparison between the DF for uncorrelated electron-hole pairs (blue dashed line) and the two-dimensional excitonic line-shape (black solid line). Fig. 12 also shows the two components of Eq. (73), the continuum and discrete absorption (shown by the red and green dot-dashed lines, respectively). Fig. 12 shows that the DF for the uncorrelated electron-hole pairs is almost identical to the exciton continuum absorption spectra. We also observe that the peak absorption occurs at an energy equal to  $E_1 - R(1)$  for [84, 5, 36]

$$R(n) = \frac{\mu_{\perp}}{m_0 \varepsilon_{\rm st}^2 \left(n - \frac{1}{2}\right)^2} \text{Ry, where } n = 1, 2, 3, ...,$$
 (53)

 $\varepsilon_{\rm st}$  is the static dielectric constant, and Ry = 13.6 eV is the Rydberg energy constant. Equation (53) gives the binding energy of the 2D exciton, which is the same as for a 2D hydrogen-like system.[5, 84, 36] Fig. 12 also shows how the oscillator strength in the imaginary part of the DF is enhanced significantly by the discrete (bound exciton) absorption. This is a typical behavior of not only two-dimensional  $M_0$  excitons in bulk materials,[81] but also of excitonic absorption in two-dimensional materials, where the reduced dimensionality enhances the Coulomb interaction due to the confinement of the carriers.[25, 37, 38]

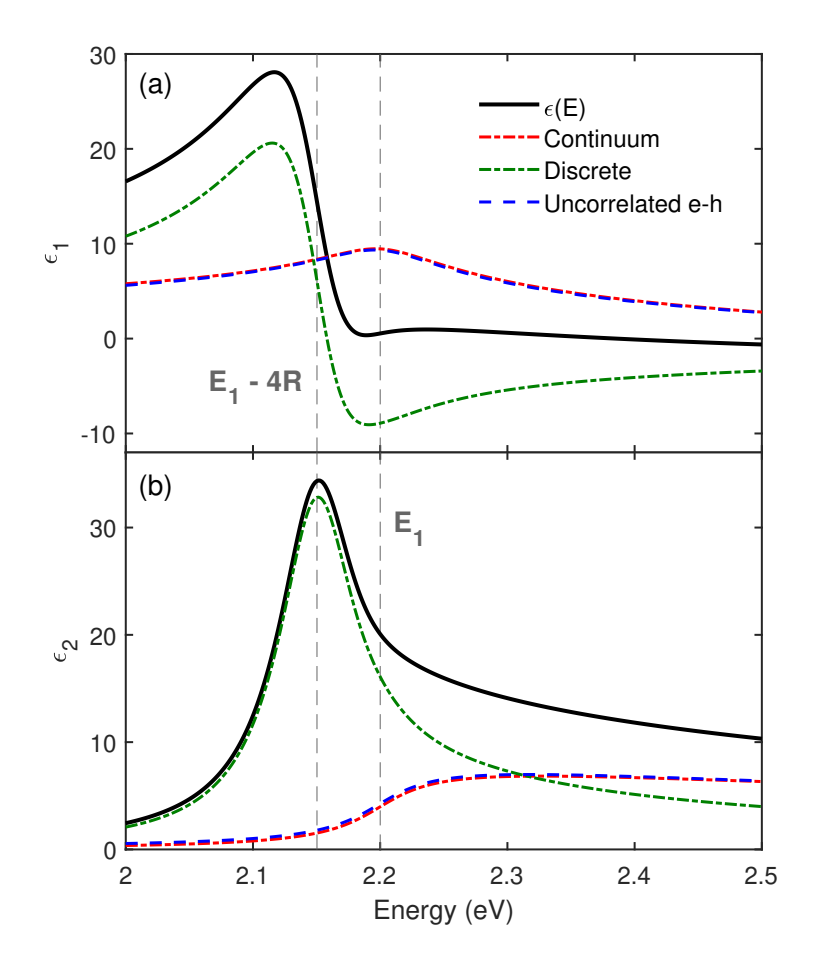


Figure 12: (a) Real and (b) imaginary part of the dielectric function of twodimensional Wannier excitons. This complex dielectric function (solid black line) is composed of the continuum (red dot-dashed line) and bound states (green dotdashed line) of the exciton. Notice the similarity between the continuum state and the optical dispersion for uncorrelated electron-hole pairs (blue dashed line). The arbitrary values for the parameters are  $E_1 = 2.2 \text{ eV}$ ,  $\Gamma = 37 \text{ meV}$ , and  $A = 41.8 \text{ eV}^2$ .

### 4.3.1 Temperature dependence of the fixed parameters

As previously stated, other than energy and broadening, Eq. (73) combined with the amplitudes in Eq. (52), provides a model absent of any fitting parameters for the CPs near the L-valley of Ge. The matrix element  $E_P = \overline{P}^2/m_0$  and the static dielectric constant  $\varepsilon_{\rm st}$  have well established values in the literature.[11, 108, 39, 40] Another required parameter is  $k_{\rm max}$ . In the rotated coordinate system, the total distance from  $\Gamma$  to L along the  $k_z$ -axis (the  $\Lambda$ -direction) is  $\pi\sqrt{3}/a_0$ . Under visual inspection, however, the  $k_{\rm max}$  value lies between  $3\pi\sqrt{3}/(5a_0)$  and  $3\pi\sqrt{3}/(4a_0)$ .[41, 109] Therefore, for our purposes, we allowed the  $k_{\rm max}$  parameter to vary within this range, but kept it fixed across all temperatures. Since we are interested in the temperature effects of the DF, we can follow the procedure described by Emminger et al.[70] to incorporate the temperature dependence of the lattice constant,[11, 42] matrix element,[11] and dielectric constant[81] in the following manner:

$$a_0(T) = a_0(0 \text{ K}) + \frac{1.315 \times 10^{-2} \text{ Å}}{\exp[(355.14 \text{ K})/T] - 1},$$
 (54)

$$E_P(T) = E_P(0 \text{ K}) \frac{a_0(0 \text{ K})^2}{a_0(T)^2},$$
 (55)

$$\varepsilon_{\rm st}(T) = 1 + \left[\frac{15.6 \text{ eV}}{E_{\rm Penn}(T)}\right]^2.$$
 (56)

The term  $E_{\text{Penn}}(T)$  in Eq. (56) is the Penn gap given by [81, 70]

$$E_{\text{Penn}}(T) = 4.146 \text{ eV} - (0.05 \text{ eV}) \left[ \frac{2}{e^{(217 \text{ K})/T} - 1} + 1 \right].$$
 (57)

For the values at zero temperature,  $E_P(0 \text{ K}) = 12.96 \text{ eV}[108, 11]$  and  $a_0(0 \text{ K}) = 5.6516 \text{ Å}.[42]$ 

#### 4.3.2 Unrenormalized effective mass

Yet another required parameter is the transverse reduced mass  $\mu_{\perp}$ , which is needed to calculate the exciton binding energy using Eq. (53), as well as the amplitudes in Eq. (52). While Dresselhaus *et al.* determined the effective electron mass  $m_{\perp}$ =0.082 of the CB from cyclotron resonance measurements,[43] to calculate  $\mu_{\perp}$ , we also require explicit values for the effective masses of the heavy and light holes at the L-valley, for which reliable values are not available. Menéndez *et al.* provide the reduced masses for both CPs as[11]

$$\frac{1}{\mu_{\perp}^{(E_1)}} = \frac{E_P}{m_0} \left[ \frac{2}{E_1^u} + \frac{1}{(E_1 + \Delta_1)^u} \right], \tag{58a}$$

and 
$$\frac{1}{\mu_{\parallel}^{(E_1 + \Delta_1)}} = \frac{E_P}{m_0} \left[ \frac{1}{E_1^u} + \frac{2}{(E_1 + \Delta_1)^u} \right].$$
 (58b)

These expressions come from a 6-band  $\mathbf{k} \cdot \mathbf{p}$ -theory model (see Appendix Sec. A for a derivation). In Eqs. (58), however, one must be careful with the energy values of  $E_1$  and  $E_1+\Delta_1$ . Zollner *et al.*[44] point out that to calculate the effective mass, one must use the unrenormalized energy values, rather than the experimental energies of the CPs. This is the meaning of the superscripts u. The unrenormalized values of the CPs incorporate the redshift due to thermal expansion, but not the self-energy due to the deformation-potential electron-phonon coupling. We can obtain

the unrenormalized energy as a function of temperature with the expression

$$E_{E_1,E_1+\Delta_1}^u(T) = E_{E_1,E_1+\Delta_1}^u(0 \text{ K}) - 3B \left(\frac{\partial E_{E_1,E_1+\Delta_1}^{\exp}}{\partial p}\right)_T \int_0^T \alpha(\theta) d\theta, \qquad (59)$$

where  $\alpha(T)$  is the temperature-dependent thermal expansion coefficient,  $B = 7.58 \times 10^{10} \,\mathrm{Pa}$  is the bulk modulus,[45] and  $(\partial E_{E_1}^{\mathrm{exp}}/\partial p)_T = 7.5 \times 10^{-6} \,\mathrm{eV} \cdot \mathrm{cm}^2 \cdot \mathrm{kg}^{-1}$  is the pressure coefficient of the  $E_1$  CP.[46] For this calculation, we take the value of  $(\partial E_1/\partial p)_T \approx [\partial (E_1 + \Delta_1)/\partial p]_T$ . We justify this assumption by noting that the spin-orbit splitting  $\Delta_1$  is related to atomic effects and it is, for the most part, unaffected by the distance of the atoms within the lattice. The thermal expansion coefficient[47]

$$\alpha(T) = \frac{1}{a_0(T)} \frac{\mathrm{d}a_0(T)}{\mathrm{d}T},\tag{60}$$

can be calculated from the expression for the lattice constant in Eq. (54). Finally, the unrenormalized energy at zero temperature can be obtained by the following procedure: We first determine experimentally the energy of the CPs as a function of temperature. These data points are then fitted with a Bose-Einstein (BE) model [17]

$$E_{E_1,E_1+\Delta_1}(T) = E_a - E_b \left( 1 + \frac{2}{e^{\theta_{\rm B}/T} - 1} \right).$$
 (61)

Once the fitted parameters  $E_a$ ,  $E_b$ , and  $\theta_B$  are determined, we set  $E^u_{E_1,E_1+\Delta_1}(0 \text{ K}) = E_a$ , where the parameter  $E_a$  differs for each CP. Since we do not know the value of  $E_a$  a priori, we used the experimental value  $E^{\text{exp}}_{E_1,E_1+\Delta_1}(0 \text{ K})$  from Ref. [18] as a starting point for the fit. We then refitted the data using the updated value of  $E_a$ 

obtained from the previous iteration. This process was repeated iteratively until  $E_a$  converged to a constant value.

# 4.3.3 Complete model

To encompass both CPs, we added two expressions similar to Eq. (73) with the appropriate amplitudes and binding energies for  $E_1$  and  $E_1 + \Delta_1$ . We also added a constant offset  $\varepsilon_{\text{off}}$  to the real part of the DF, to account for additional nonresonant contributions from other interband transitions. The complete form of our model is

$$\varepsilon(E) = \varepsilon_{\text{off}} + \frac{A^{(E_1)}}{[E + i\Gamma^{(E_1)}]^2} \left\{ g_a \left[ \sqrt{\frac{R^{(E_1)}}{E_1 - E - i\Gamma^{(E_1)}}} \right] + g_a \left[ \sqrt{\frac{R^{(E_1)}}{E_1 + E + i\Gamma^{(E_1)}}} \right] \right. \\
\left. - 2g_a \left[ \sqrt{\frac{R^{(E_1)}}{E_1}} \right] \right\} + \frac{A^{(E_1 + \Delta_1)}}{[E + i\Gamma^{(E_1 + \Delta_1)}]^2} \left\{ g_a \left[ \sqrt{\frac{R^{(E_1 + \Delta_1)}}{E_1 + \Delta_1 - E - i\Gamma^{(E_1 + \Delta_1)}}} \right] \right. \\
\left. + g_a \left[ \sqrt{\frac{R^{(E_1 + \Delta_1)}}{E_1 + \Delta_1 + E + i\Gamma^{(E_1 + \Delta_1)}}} \right] - 2g_a \left[ \sqrt{\frac{R^{(E_1 + \Delta_1)}}{E_1 + \Delta_1}} \right] \right\}. \tag{62}$$

It is worth pointing out that, in the parabolic approximation of the reduced masses of Eq. (58), the matrix element  $E_P$  cancels out in the amplitudes of Eq. (52). The resulting amplitudes have the form

$$A^{(E_1)} = \frac{4e^2 E_1^u (E_1 + \Delta_1)^u k_{\text{max}}}{3\pi\varepsilon_0 \left[2(E_1 + \Delta_1)^u + E_1^u\right]} \text{ for } E_1$$
 (63a)

and 
$$A^{(E_1 + \Delta_1)} = \frac{4e^2 E_1^u (E_1 + \Delta_1)^u k_{\text{max}}}{3\pi\varepsilon_0 \left[ (E_1 + \Delta_1)^u + 2E_1^u \right]} \text{ for } E_1 + \Delta_1.$$
 (63b)

With this definition, the ratio of the CPs amplitudes would be  $A^{(E_1)}/A^{(E_1+\Delta_1)} \propto (3E_1 + \Delta_1)/(3E_1 + 2\Delta_1)$ , or about 0.97 for a temperature of 4 K.

# 4.4 Results

# 4.4.1 Fitting procedure

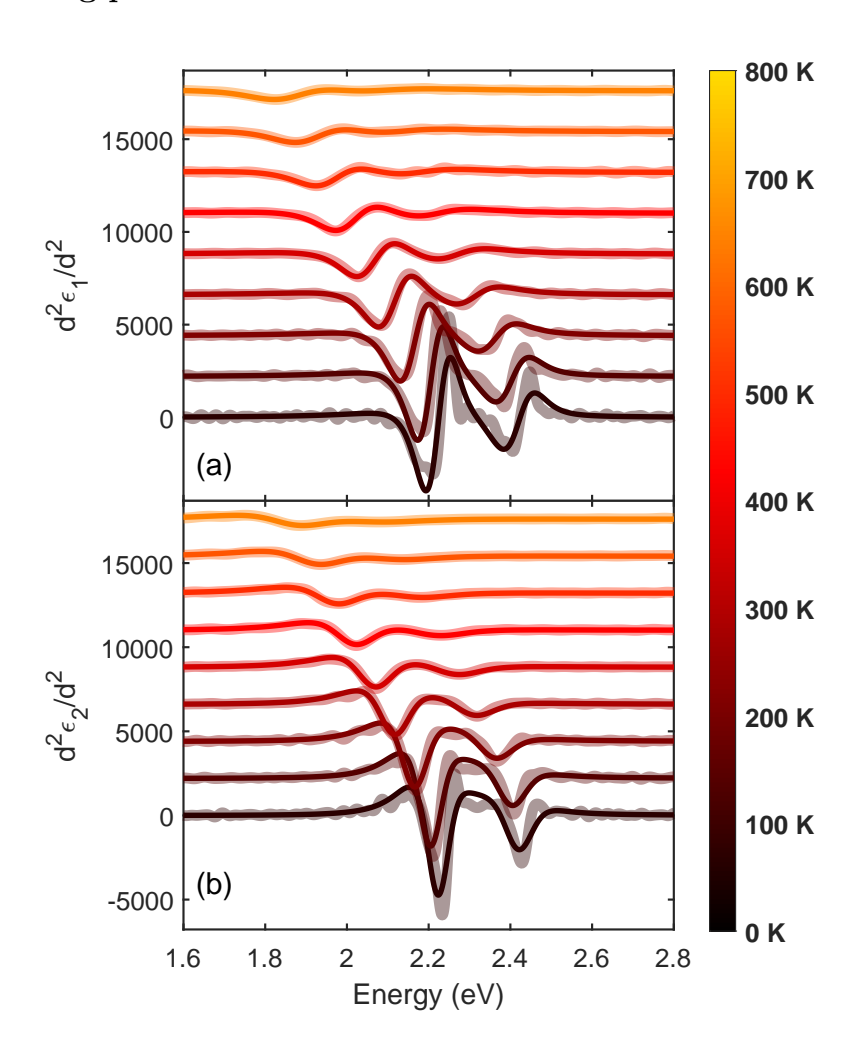


Figure 13: 2<sup>nd</sup> derivative of the real (a) and imaginary (b) part of the dielectric function. The derivatives of the experimental data (translucent lines) were calculated using the EG digital filter in Eq. (64). The fitted 2<sup>nd</sup> derivatives of Eq. (62) for each temperature are shown by the solid lines.

To fit the energy and broadening parameters, we performed a CP analysis by fitting the 2<sup>nd</sup> derivative of our model in Eq. (62) to the 2<sup>nd</sup> derivative of the experimental data. We then compared their respective DFs. To obtain the 2<sup>nd</sup> derivatives, we applied a digital filter to the DF to smooth the original signal and suppress the noise in the experimental data. We then convoluted the DF with the derivative of the filter to obtain the desired DF derivative (see Sec. D for more information on this procedure). For the digital filter, we used the extended Gauss (EG) filter, which is defined in direct space as[48, 49]

$$b_M(x) = \sum_{m=0}^{M} \left[ (-1)^m \frac{\Delta E^m}{m!} \frac{\mathrm{d}^m}{\mathrm{d}\Delta E^m} \right] \frac{\exp[-x^2/(4\Delta E^2)]}{2\sqrt{\pi \Delta E}},\tag{64}$$

where we selected M=4 according to the discussion in Ref. [48]. The filter width  $\Delta E$  was determined by identifying the white noise onset in the Fourier coefficients of the data. [70] In general, given that noise increases with temperature, the selected filter width also increased accordingly. To fit our model parameters, we minimized the residuals between the DF derivatives of the experimental data and the model. We performed this minimization procedure using MATLAB's nonlinear least-squares optimization function. [50] For consistency, the derivative of the model must be computed in the same manner as the derivative of the experimental data. [20] Therefore, we convoluted Eq. (62) with the same EG filter (and same filter width  $\Delta E$ ) while leaving the fitting parameters free. Fig. 13 shows that the fitted derivative of the model is in good agreement with the experimental data.

To make the critical point analysis more thorough, we repeated the minimization procedure with a Savitzky-Golay (SG) digital filter.[51] To generate the smoothing filter, we used MATLAB's SG built-in function.[50] The order of the polynomial to be fitted was selected according to the noise of the data. Again, similar to the EG filter, the order of the polynomial needed to be adjusted at each temperature. The frame length, on the other hand, was constrained to 5% of the total number of data points. The results were nearly identical to the EG digital filter. The values of the fitted parameters varied less than 1% between the two digital filters. Hence, the derivatives for the SG filter are not shown in Fig. 13. For a more in-depth discussion of the fitting procedure and comparison of the two digital filters, see Sec. D in the Appendix.

#### 4.4.2 Temperature dependence of the fitting parameters

We can use the fitted energies and broadenings of the entire temperature series to characterize these parameters as a function of temperature. We do this by fitting the BE model of Eq. (61) and (65) to the energy and broadening parameters:[17]

$$\Gamma^{(E_1, E_1 + \Delta_1)}(T) = \Gamma_1 + \Gamma_0 \left( 1 + \frac{2}{e^{\theta_B/T} - 1} \right).$$
 (65)

The squares in Fig. 14 show the fitted parameters from the 2<sup>nd</sup> derivative analysis. Along with the BE models of the present work, Fig. 14 also shows the BE models for these CPs from the literature for comparison.[17, 18, 32] It is clear from Fig.

14 that the energies of our model are greater than in the previous characterization efforts. This is to be expected, since the fitted absorption maximum in our model is not the energy of the CP, but rather the first discrete absorption peak of the exciton, which is lower than the CP energy by the exciton binding energy. Broadening also behaves differently. In Refs. [17, 18, 32], the broadenings of the CPs are fitted with Eq. (47b). In contrast, Eq. (73) incorporates broadening by convolution with a Lorentzian. Although they are difficult to compare quantitatively given the two extra parameters B and  $\phi$ , the broadening of Eq. (47b) tends to be larger than for a Lorentzian oscillator. Thus, our model requires a larger broadening than the references values to match the experimental data. Table 1 shows the fitted parameters for the BE model, along with the parameters in the literature.

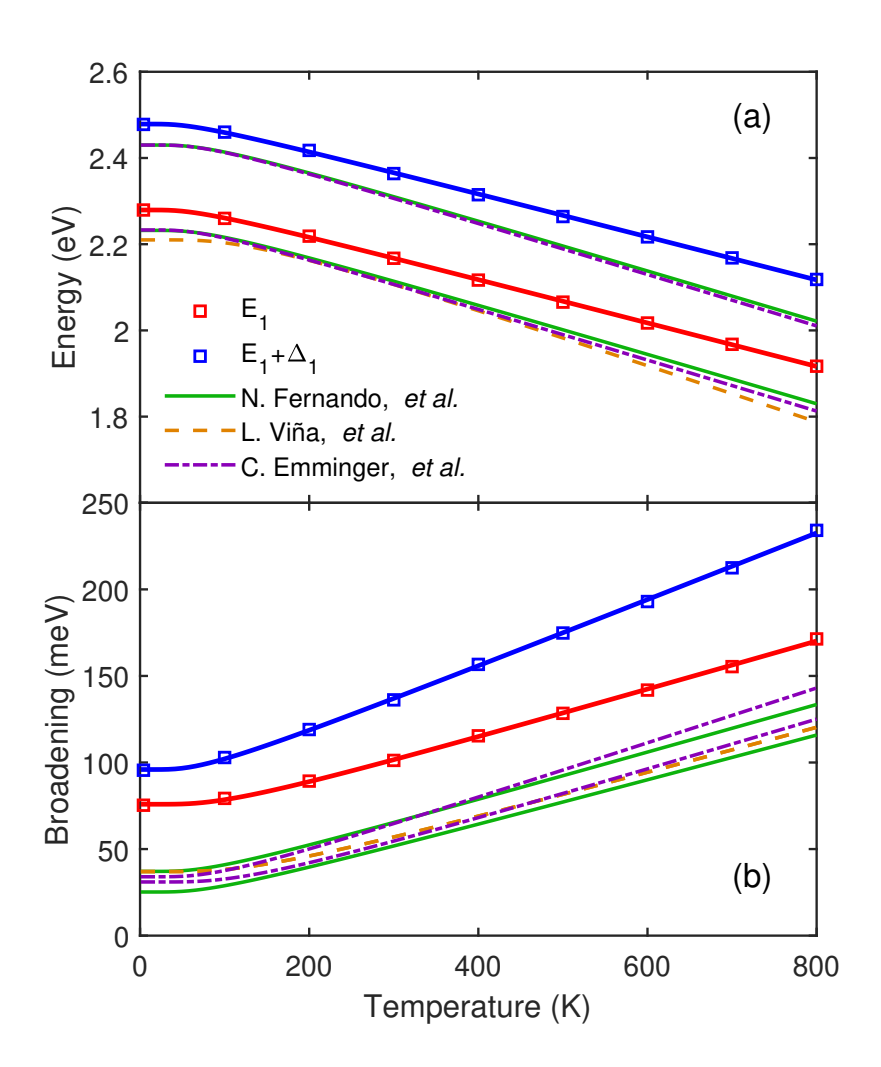


Figure 14: Bose-Einstein model fits for the energy (a) and broadening (b). Shown by the squares are the fitted parameters, while the blue and red solid lines are the Bose-Einstein models. For comparison, data from different references is also shown.[17, 18, 32]

Table 1: Fitted parameters of the Bose-Einstein model for the energy and broadening of the  $E_1$  and  $E_1 + \Delta_1$  critical points.

T. Carlotte	$E_{a}$ (eV)	$E_b$ (eV)	$\theta_{\mathrm{B}_{\mathrm{E}}}$ (K)	$\Gamma_1 \; (\mathrm{meV})$	$\theta_{B_F}$ (K) $\Gamma_1$ (meV) $\Gamma_0$ (meV)	$\theta_{\rm Br}$ (K)
	3		) A A A	`		
$E_1{}^a$	$2.32 \pm 0.01$	$0.04 \pm 0.01$	$176 \pm 54$	$56 \pm 7$	$19\pm10$	276(f)
$E_1$ (Ref. [17])	$2.33 \pm 0.03$	$0.12 \pm 0.04$	$360 \pm 120$	$12 \pm 9$	$25 \pm 3$	376(f)
$E_1 \; ({ m Ref.} \; [18])$	$2.295 \pm 0.002$	$0.063 \pm 0.004$	$218 \pm 14$	11 ± 1	$14.2 \pm 0.3$	218(f)
$E_1 \; ({ m Ref.} \; [32])$	$2.292 \pm 0.002$	$0.059 \pm 0.003$	$198 \pm 10$	$6\pm 2$	$25 \pm 3$	$341 \pm 34$
$E_1 + \Delta_1^{\mathrm{a}}$	$2.52 \pm 0.01$	$0.04 \pm 0.02$	$165 \pm 79$	77 ± 8	$19 \pm 11$	198(f)
$E_1 + \Delta_1 \; (\text{Ref. [17]})$	ı	ı	ı	8 ∓ 6	$43 \pm 5$	$484(\mathrm{sic})$
$E_1 + \Delta_1 \; (\text{Ref. [18]})$	$2.494 \pm 0.002$	$0.064 \pm 0.001$	218(f)	$22 \pm 3$	$15.1 \pm 0.6$	218(f)
$E_1 + \Delta_1 \text{ (Ref. [32])}$	$2.494 \pm 0.002$	$0.064 \pm 0.003$	$213\pm9$	$14 \pm 1$	20(f)	250(f)

 $^{a}$ Present work.

# 4.4.3 Dielectric function

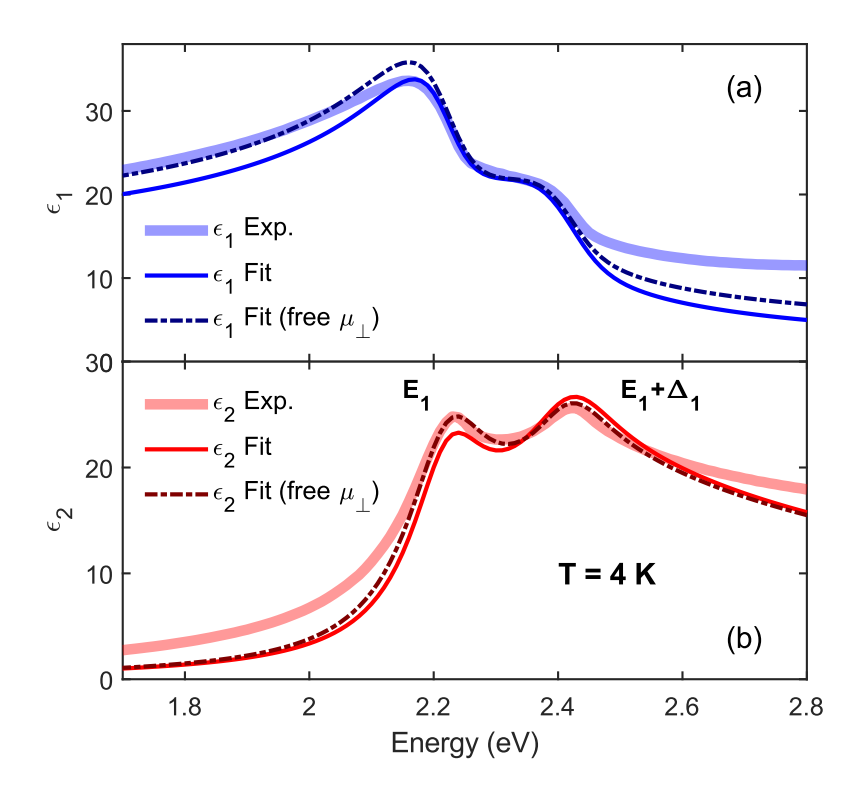


Figure 15: Real (a) and imaginary (b) part of the dielectric function of Ge at 4 K. The translucent lines are the experimental data, the fitted model with masses from the  $\mathbf{k} \cdot \mathbf{p}$ -model in Eqs. (58) is shown by the solid lines, and the model with the reduced mass as an additional free parameter is shown by the dot-dashed lines.

At a temperature of 4 K, Fig. 15 shows the model DF (62) in comparison to the experimental data. Fig. 16 shows the same comparison for temperatures from 100 to 600 K. These figures show an outstanding agreement between the theoretical model and the experimental DF across the entire temperature range.

This level of agreement is remarkable given that no free parameters other than energy and broadening are fitted. Nonetheless, it is evident from Figs. 15 and 16 that, while the model is in excellent agreement with the data near the CPs, it misses contributions from additional absorption processes. At lower energies, the model underestimates the value of  $\varepsilon_2$  by about 2 units. We attempted to reduce this mismatch by including the direct bandgap absorption of Ge. At around 0.9 eV, the direct bandgap of Ge  $E_0$  presents itself as the first CP contributing to the absorption. The DF near  $E_0$  is categorized as a three-dimensional  $M_0$ van Hove singularity.[81] A description of this CP that not only accounts for the formation of excitons, but also incorporates excitonic screening already exists in the literature. [9, 52] More importantly for our purposes, this lineshape has previously been applied to Ge in a temperature series similar to our data. [70] In their approach, Emminger et al. [70] used the experimental, rather than the unrenormalized  $E_0$  CP energies for the calculation of the effective masses. Unfortunately, even with the corrected energies and incorporating non-parabolicity effects,  $E_0$ contributes less than 1 unit to the amplitude of  $\varepsilon_2$ . Therefore, we did not include the CP  $E_0$  in our calculations (see Appendix Sec. E more information on  $E_0$ ). The  $E'_0$  and  $E_2$  CPs also contribute to  $\varepsilon_2$  at higher energies. However, unlike the direct bandgap  $E_0$ , there is no established lineshape for these CPs, hence these contributions to the absorption are omitted as well.

A more significant issue than the mismatch at high and low energies is the

deviation of  $\varepsilon_2$  at  $E_1$  (around 2.2 eV) and  $E_1 + \Delta_1$  (around 2.4 eV). At the  $E_1$  CP, the  $\varepsilon_2$  amplitude of our model is smaller than in the experimental data, whereas for  $E_1 + \Delta_1$ , the model overestimates the amplitude. This could be due to an incorrect value of  $k_{\text{max}}$ , which has been fixed at  $0.7\pi\sqrt{3}/a_0$  for all our calculations. As seen in Fig. 10, the range over which the hh-band ( $\Lambda_4 \oplus \Lambda_5$ -band) is parallel to the CB ( $\Lambda_6$ -band) could be different than for the lh-band ( $\Lambda_6$ -band). This would lead to different values of  $k_{\text{max}}$  for  $E_1$  and  $E_1 + \Delta_1$ . Moreover, with increasing temperature, the bands renormalize and change their curvature slightly, which would ultimately result in a different value of  $k_{\text{max}}$  at each temperature. As the temperature increases, the agreement in the amplitude of the model and experiment improves for both CPs (see Fig. 16). This could be explained by the temperature dependence of  $k_{\text{max}}$ . Nevertheless, a different  $k_{\text{max}}$  value for  $E_1$  and  $E_1 + \Delta_1$  is likely to have a small effect, considering how similar the hh and lh bands are to each other near the L-point.

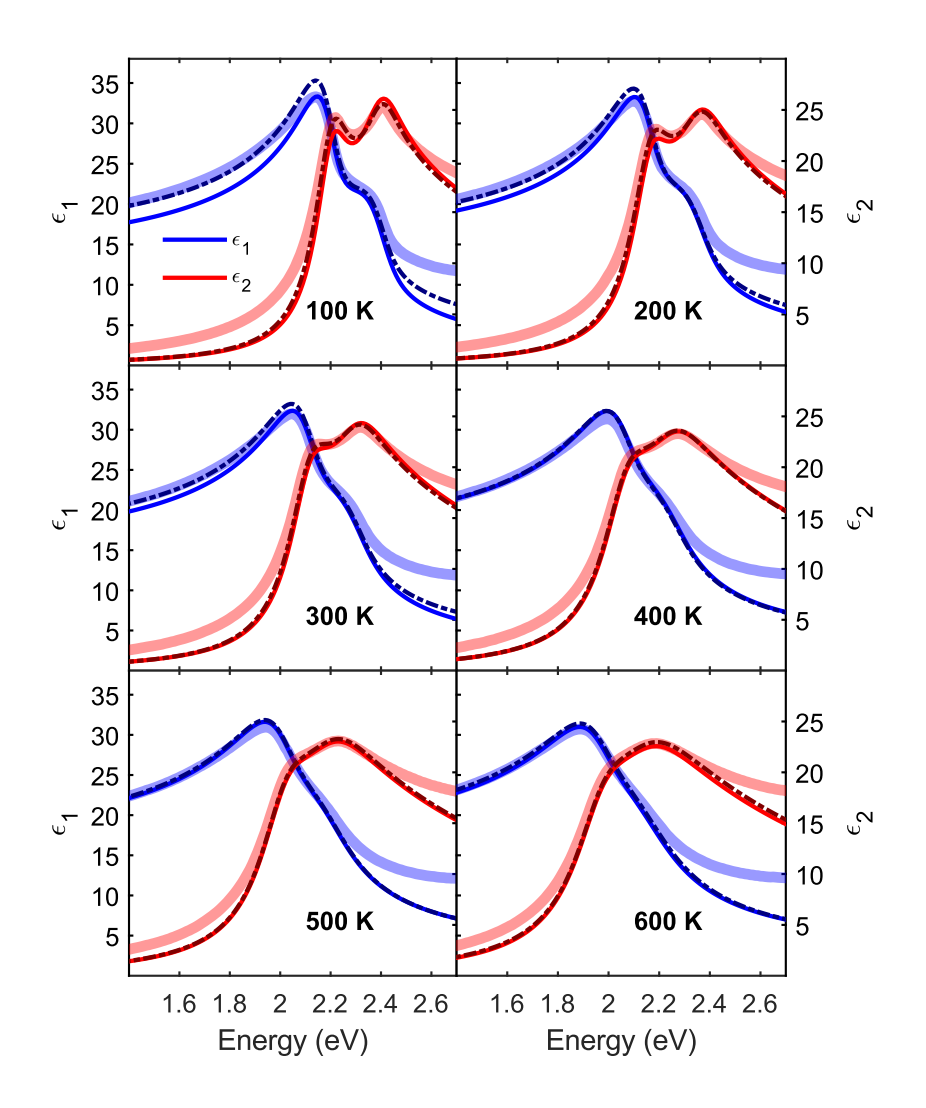


Figure 16: Dielectric function of Ge from 100 to 600 K. The translucent lines are the experimental data, the fitted model from the  $\mathbf{k} \cdot \mathbf{p}$ -model in Eqs. (58) is shown by the solid lines, and the model with the reduced mass as an additional free parameter by the dot-dashed lines.

#### 4.4.4 Fitting the effective mass

A bigger factor in the disagreement between model and experiment could be the calculated reduced masses. The amplitudes in Eqs. (63) are only valid in the 6-band  $\mathbf{k} \cdot \mathbf{p}$ -theory model at the L-point, where the reduced masses are given by Eq. (58). We resort to this definition of the masses in the absence of any known values for the hh and lh effective masses. For the standard definition of the reduced mass,

$$\frac{1}{\mu_{\perp}^{(E_1, E_1 + \Delta_1)}} = \frac{1}{m_{\perp}^{(L_6^+)}} + \frac{1}{m_{\perp}^{(L_4^- \oplus L_5^-, L_6^-)}},\tag{66}$$

the amplitudes of the DF in Eq. (62) revert to their original forms of Eq. (52). To improve the agreement between theory and experiment, we can treat the reduced masses for both CPs as additional free parameters and refit our data. To avoid inconsistencies with the previously fitted values of broadening and energy, we divided the fitting process in two steps. Initially, to fit the broadening and energy, we performed a  $2^{\rm nd}$  derivative fitting while holding the reduced masses constant and equal to their theoretical values. Subsequently, we fitted  $\mu_{\perp}^{(E_1,E_1+\Delta_1)}$  and  $\varepsilon_{\rm off}$  to the DF. If any discrepancies in their corresponding  $2^{\rm nd}$  derivatives appeared between the model and experimental data, the two-step procedure was repeated until no further change was observed.

The effective masses obtained from this new fitting procedure can be seen in the dot-dashed lines of Figs. 15 and 16. Although the agreement between

the model and the data improved significantly, there is no physical basis behind the fitted reduced mass values. Fig. 17 shows the fitted masses in comparison with the values calculated from Eq. (58). It also shows literature values of the reduced masses at 4 K[11, 53] and at room temperature. [54] It can be seen that the difference between the fitted masses of the CPs is larger than in any reference. Furthermore, the fit suggests that the reduced mass for  $E_1$  should be larger than the mass for  $E_1 + \Delta_1$ , which is not the case according to the literature values.[55] Nonetheless, it has been pointed out by Cardona that, in the  $\Lambda$ -direction, but not at the L-point, linear terms proportional to  $k_{\perp}$  in the bands tend to increase the reduced mass of  $E_1$  while decreasing it for  $E_1 + \Delta_1$ .[56, 17] This trend is also seen in Fig. 17. In our calculations, we used the masses at the L-point calculated from Eq. (58). However, this expression might not necessarily describe the masses in the  $k_{\text{max}}$ -region of the band structure (grey area in Fig. 10). In this region, Cardona states that including linear  $k_{\perp}$  terms in the band structure would increase the reduced mass  $\mu_{\perp}^{(E_1)}$ . We would like to stress to the reader that, while the fitted reduced masses improve significantly the agreement between model and data, the strong temperature dependence seen in these fitted values should not be overinterpreted. As discussed, these masses serve purely as empirical parameters within the fitting procedure, and the effect of these linear terms in the reduced masses needs a more thorough study, perhaps in comparison with larger  $\mathbf{k} \cdot \mathbf{p}$ models. In effect, this additional fitting parameter can be used to improve the agreement between model and data, but until further research clarifies the effects of additional terms in the reduced masses of these CPs, we are unable to justify this additional free parameter on theoretical grounds. Still, even without treating the masses as free parameters, we emphasize the excellent agreement between the theoretical model and the experimental data. Put another way, while the empirical fitting of the masses improves the match in the DF, it is not essential for obtaining remarkable results.

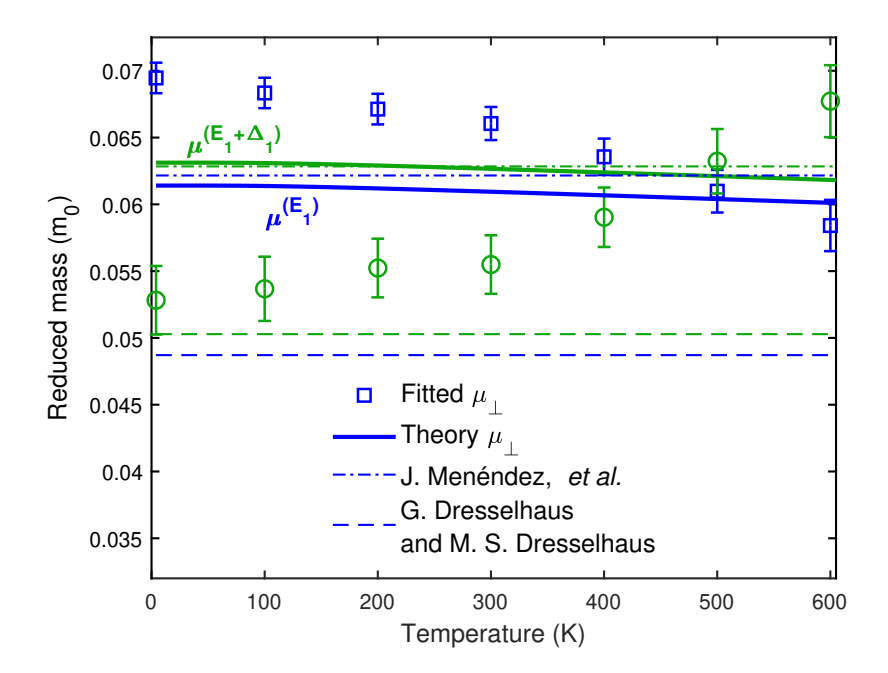


Figure 17: Fitted reduced masses as a function of temperature for  $E_1$  ( $\square$ ) and  $E_1 + \Delta_1$  ( $\bigcirc$ ). The solid lines show results from Eqs. (58). The dot-dashed and dashed lines are literature values at 4 K[11, 53] and room temperature,[54] respectively.

## 4.5 Discussion

One possibility for the difference between the measured and calculated DF is that near the energy of  $E_1$ , there are interband transitions that do not occur along the  $\Lambda$ -direction of the Brillouin zone (in the  $\Sigma$ -direction, for example). While there is no CP present in this region, there is an energy separation between the CB and VB similar to the energy of  $E_1$ . Depending on the strength of these additional absorption processes, they could affect the amplitude of each CP differently.

Additionally, surface effects could have an impact on the quality of the agreement between model and experiment. The physical and numerical removal of the oxide layer described in Sec. 4.2 has been proven to be effective previously.[33, 32, 70] Hence, there is no reason to think that our point-by-point fit has large errors, or that temperature changes would affect this procedure significantly. Nonetheless, it is worth noting how this oxide layer affects the pseudo-DF  $\langle \varepsilon \rangle$ . As the oxide layer gets thicker, it tends to increase the amplitude of  $E_1$  in  $\langle \varepsilon_2 \rangle$ , while leaving the amplitude of  $E_1 + \Delta_1$  constant. In other words, an underestimation of the oxide layer thickness will give an  $E_1$  amplitude greater than it should be in the extracted point-by-point fit for the substrate. Fig. 18 shows the DF of the point-by-point fit with different oxide layer thicknesses compared to our model. While the model resembles closer to the 30 Å oxide layer fit, the previously mentioned procedure to estimate the oxide thickness yielded a GeO<sub>2</sub> layer of 11 Å. Therefore there is no evidence from the fitting that this layer should be as thick as 30 Å. Hence, the match between our model and the overlayer fit seems to be purely coincidental. On the other hand, different surface orientations of the bulk Ge material lead to a different surface reconstructions, which also affects interband transitions due to the different lattice periodicity at the surface.[57] These effects, however, are too small to make a difference in the discrepancies between our model and the experimental data (see Appendix Sec. F for data differences depending on surface orientation).

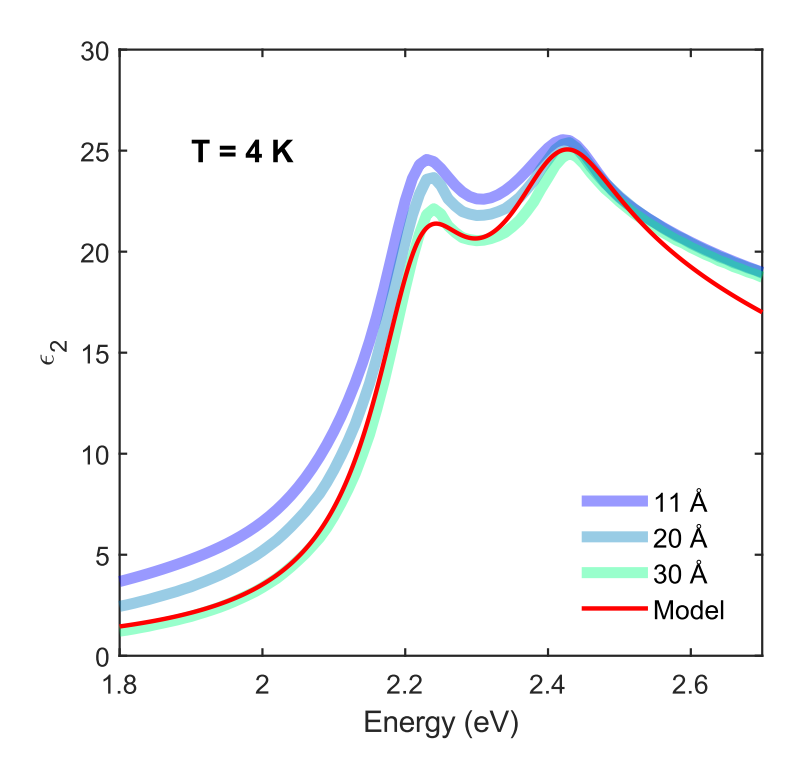


Figure 18: Comparison between the model at 4 K (red solid line) and the pointby-point fits with different thicknesses for the oxide correction (translucent lines).

Yet another factor to consider is excitonic screening. In the presence of excited electrons in the CB, the Coulomb interaction between the carriers gets partially screened. In his DF expression for three-dimensional excitons, Tanguy accounts for excitonic screening by solving the Schrödinger equation for the Hulthén potential. [52] In contrast, such a solution for screened two-dimensional excitons does not exist in the literature. [60, 61, 62, 63] For this reduced dimensionality problem, recent efforts have found the binding energy for screened excitons in two-dimensional materials (these are solutions to the Rytova-Keldysh potential). [58, 59] Unfortunately, an expression of the DF for this potential is yet to be found. Moreover, given the low carrier densities at play, it is unlikely that including excitonic screening effects would improve our model.

Therefore, we conclude that the most probable sources of the difference between experiment and theory are nonresonant interband transitions and the precise values of the reduced masses of the CPs.

## 5 RESULTS AND ANALYSIS

## 5.1 Data presentation

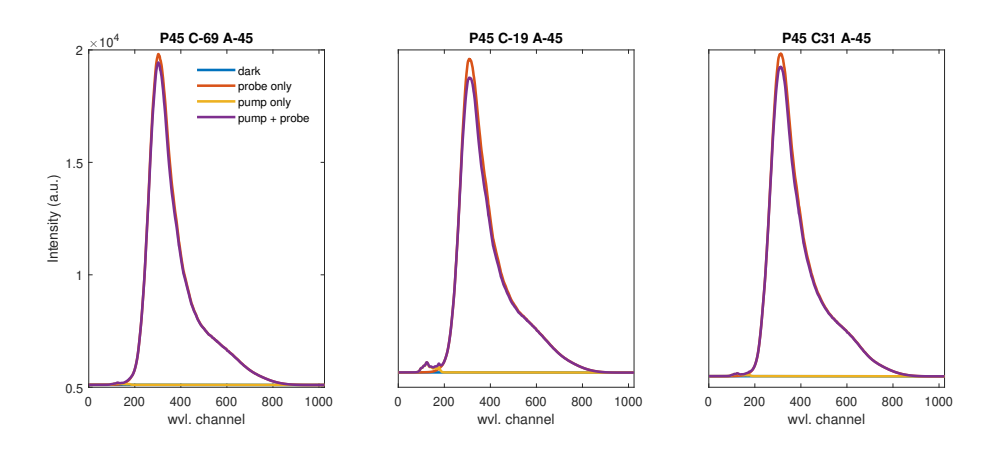


Figure 19: Intensities of the four acquisition channels: dark (blue), probe only (red), pump only (yellow), and pump+probe (purple). The intensities are shown for three compensator angles.

We recorded time-resolved reflectance-difference spectra over a delay range of -5 ps to 1 ns and a spectral range of 1.8 eV to 3.0 eV. Each delay point was sampled by averaging approximately 400 laser shots after removing outliers exceeding three standard deviations from the mean. Although extended delay times were acquired, the carrier dynamics described in the following sections occur primarily within the first picosecond. Consequently, time delays beyond 3 ps will not be considered further in this analysis.

Figure 19 displays the intensities of the four acquisition channels generated by the synchronized choppers: dark, probe only, pump only, and pump+probe, at three representative compensator angles. Using Eq. (43), these recorded intensities were converted into the reflectance difference  $\Delta R/R$  shown in Figure 20.

Before measurements were performed, the pump beam power and diameter were measured at 3.0 mW and 305  $\mu$ m, respectively. Using this quantities, we can estimate a carrier density of  $2.5 \times 10^{21}$  cm<sup>-3</sup> using Eq. (34). This calculated density, however, is an overestimation which yields unphysical results, as will be explained later in the chapter.

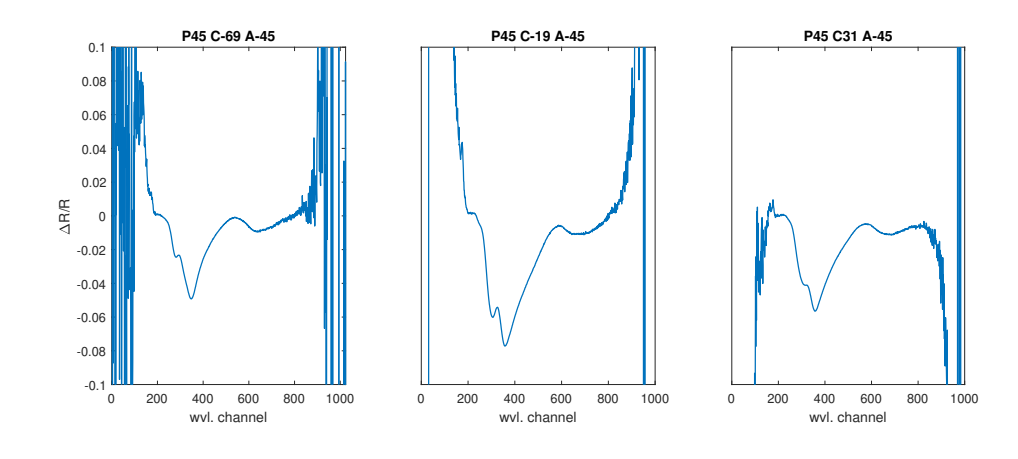


Figure 20: Reflectance difference for three compensator angles.

A reference measurement of the sample was obtained with a commercial ellipsometer. This reference, combined with Eq. (38), provided the time-resolved ellipsometric angles, which in turn yield the dielectric function. Figure 21 presents the resulting dielectric function after applying the oxide correction described in Section 3.2.

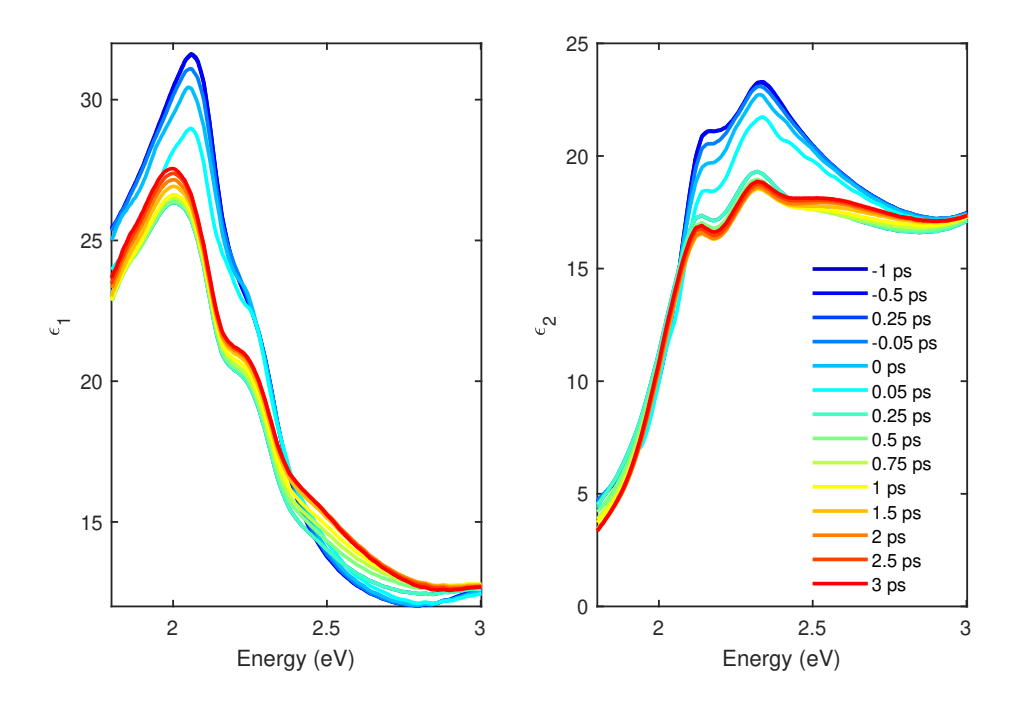


Figure 21: Real (left) and imaginary (right) parts of the experiential dielectric function after an oxide correction from -1 to 3 ps delay time.

# 5.2 Ultrafast dynamics and band filling

The decoherence and thermalization timescales of Ge vary within the literature. [69, 93, 94] Nonetheless, the upper limit for the thermalization time of the initial population of photo-excited carriers is agreed upon as less than 100 fs. [94, 95] Once thermalized, the carriers can be described by a distribution function which, given the carrier densities generated in our experiment, is degenerate. Consequently, we simulated the ultrafast dynamics of the carriers using Fermi-Dirac statistics, which in turn enabled us to model the measured DF. Figure 22 provides a quali-

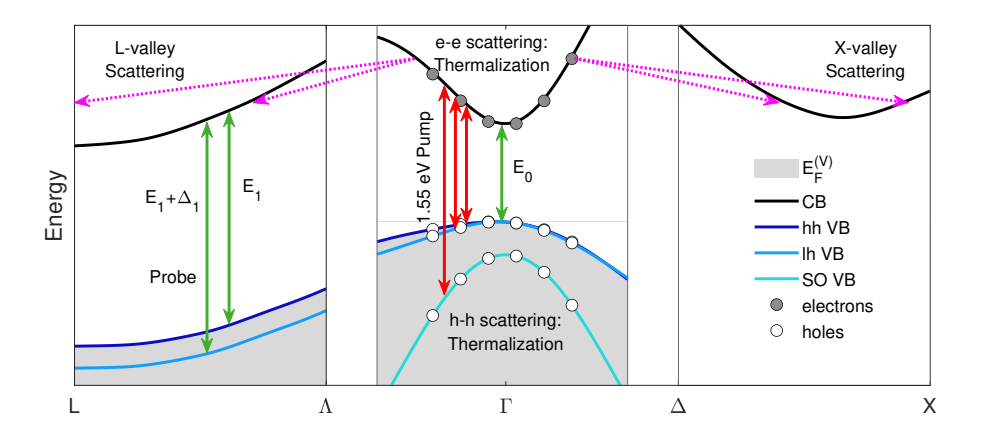


Figure 22: The initial 1.55 eV pump pulse (red arrows) promotes electrons (gray circles) from the heavy-hole (blue line), light-hole (light blue line), and split-off (cyan line) valence band to the conduction band (black line) near the Γ-point. The pump pulse also creates holes (white circles) in the valence bands. Once in the conduction band, the electrons thermalize and scatter to the L- and X-valley. tative overview of the initial dynamics induced by the high-intensity laser during the measurements. At 1.55 eV, the infrared pump laser is energetic enough to promote electrons from the hh, lh, and SO VBs to the CB. This excitation of carriers occurs near the Γ-point of the Brillouin zone. The excess energy of the carriers in the CB of Eq. (31) has previously been correlated with the effective electron temperature as [73]

$$E_{\rm c} = 3k_{\rm B}T_{\rm c}. (67)$$

Since this expression is valid for both electrons and holes, we used the subscript c (which stands for carriers  $\equiv e,h$ ). However, at high carrier densities, where the

distribution is degenerate, obtaining the effective carrier temperature becomes a more involved process. Nevertheless, by equating the energy of the total number of absorbed photons  $n_{\text{photons}}$  to the total energy of the electron-hole distribution,

$$\sum_{\text{CB}} \sum_{\mathbf{k}} E_{\text{e}}(\mathbf{k}) f_e(\mathbf{k}) + \sum_{\text{VB}} \sum_{\mathbf{k}} E_{\text{h}}(\mathbf{k}) f_h(\mathbf{k}) = n_{\text{photons}} \hbar \omega_{\text{pump}},$$
 (68)

Smirl obtained a similar expression for the effective carrier temperature in a Fermi-like distribution.[99] Therefore, for the present work, we used Eq. (67) to estimate the initial effective temperature of the carriers. The terms  $f_{e,h}(\mathbf{k}) =$  $\{e^{[E_{e,h}(\mathbf{k})\pm\mu]/k_{\mathrm{B}}T_{e,h}}+1\}^{-1}$  in Eq. (68) are the Fermi-Dirac distributions for the electrons and holes, respectively. As the initial hot electrons cool down, they rapidly scatter to the satellite valleys (L- and X-valley), eventually accumulating in the L-valley due to its lower energy. [68, 69] Intervalley scattering in Ge has been studied extensively over the years and the rates of scattering have (for the most part) an agreed upon value. 80, 93, 94, 95, 96, 97, 98 However, we will not concern ourselves with these scattering rates. Instead, our approach will be to calculate the density of carriers that each valley allows as a function of temperature. The carrier population at each valley will depend on their corresponding density of states. Once we know how the carrier density behaves throughout the temperature of the carriers, we can calculate the optical response as a function of this carrier density and then compare it with the experimental data.

## 5.2.1 Carrier statistics

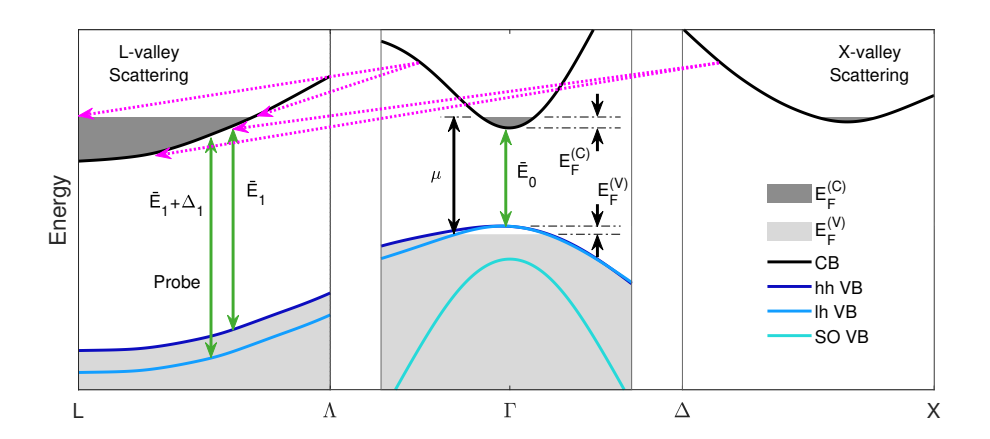


Figure 23: Once the hot electrons (and holes) thermalize to a distribution with a defined temperature, they raise the quasi-Fermi energy of the conduction band  $E_F^{(C)}$  (dark gray area) [and of the valence band  $E_F^{(V)}$  (gray area)]. Because Ge is an indirect semiconductor, the electrons do not return to the  $\Gamma$ -valley. Instead, they eventually relocate from the X-valley to the L-valley (the lowest conduction valley). At this stage, the energy required to move the electrons from the valence band to the conduction band is given by the quasi-Fermi energy  $E_F^{(C)}$  [and  $E_F^{(V)}$ ] plus the renormalized bandgap [this is the definition of the chemical potential  $\mu$  (black arrow)]. In the case of the L-valley, it is the renormalized energy of the critical points  $\overline{E}_1$  and  $\overline{E}_1 + \Delta_1$ , not the renormalized bandgap that influence the interband transitions (green arrows).

As shown in Figure 23, the change in the electron population of the CB (and hole population of the VB) yields a quasi-Fermi level  $E_F^{\rm (C)}$  above the CB minimum [and

 $E_F^{(V)}$  below the VB maximum]. After intervalley scattering takes place, the excited electrons will populate the different valleys of the CB. When electrons occupy the previously empty CB states, the band becomes partially filled, which reduces interband transitions into those states. As a result, the material's absorption is diminished. Therefore, to account for band-filling effects, we must first estimate the initial carrier density, which determines the shift in the Fermi level.

Previous studies have shown that, due to its higher density of states, electrons scatter to the X-valley before settling at the L-valley.[69] Within a few picoseconds, however, almost the entire X-valley electron population scatters out of this valley and relocates to the L-valley.[98] This is shown by the dotted magenta arrows in Figure 23. As a side note, in the present work, we will ignore the change in the quasi-Fermi energy in the VB. This is because, while we are interested in the chemical potential of Eq. (32), the photo-generated holes are confined to the  $\Gamma$ -valley and do not influence the VB at other points in the band structure. The zone at which we are probing, on the other hand, is near the L-valley (the  $E_1$  and  $E_1 + \Delta_1$  CPs). Therefore, the change in  $E_F^{(V)}$  does not affect the interband transitions in the probing region.

Although intervalley scattering redistributes the carriers among the entire CB, the initial carrier density is determined solely by direct bandgap transitions (since we are ignoring indirect bandgap transitions, only the  $\Gamma$ -valley generates photoexcited carriers). By measuring the power and beam-spot diameter of the pump,

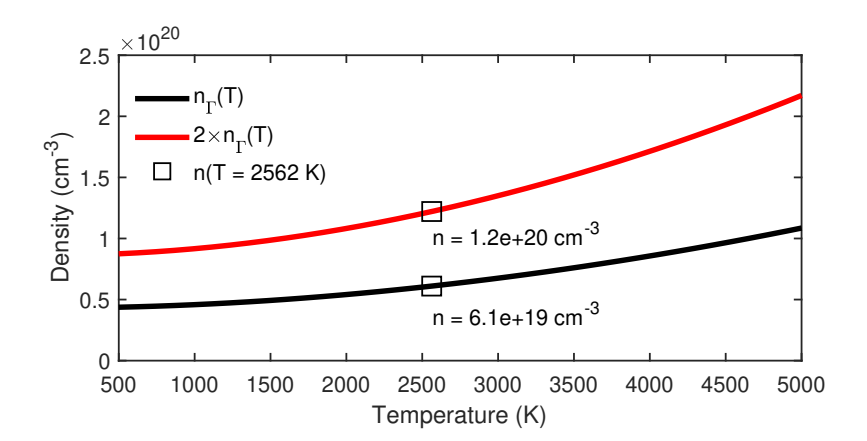


Figure 24: Charge carrier density as a function of temperature. The black line is given by Eq. (71a), and the red line is the same density multiplied by 2. The squares  $(\Box)$  show the density at the effective carrier temperature given in Eq. (67).

we can use Eq. (34) to estimate the initial carrier density. With this estimation, we can use the expression[100]

$$n_{\Gamma}(T) = \frac{1}{4} \left( \frac{2m_{\Gamma} k_{\rm B} T}{\pi \hbar^2} \right)^{3/2} F_{1/2} \left( \frac{\mu - E_0}{k_{\rm B} T} \right), \tag{69}$$

to solve for the chemical potential  $\mu$  at a given temperature and carrier density. The terms  $k_{\rm B}$ ,  $\hbar$ , and  $F_{1/2}$  in Eq. (69) are the Boltzmann constant, reduced Planck constant, and the complete Fermi integral of order 1/2, respectively. Although Eq. (69) is not analytically invertible, we can use Eq. (67) to calculate the effective carrier temperature and transform the dependence of the carrier density from  $n_{\Gamma}(\mu, T) \to n_{\Gamma}(\mu)$ . We then create the dummy function

$$f(\mu) = n_0 - n_{\Gamma}(\mu), \tag{70}$$

where  $n_0$  is the initial density. By finding the root of Eq. (70), we can determine the chemical potential at a given density and temperature. We can find this root by using the MATLAB built-in function bisection(f,LB,UB,target).[101] In this function, f is the dummy function of Eq. (70), LB and UB are the lower and upper bounds of the root, respectively, and target is the value to find. In our case, the target is  $n_0$ . To compute the complete Fermi integral, we note that  $F_j(x) = -\text{Li}_{j+1}(-e^x)$ , where Li is the polylogarithm function. This allows us to use the MATLAB polylogarithm function polylog(n,x), where n is the order of the polylogarithm and x is the argument. Unfortunately, the chemical potential obtained in this manner yields unphysical results. Therefore, we take a different approach to calculate the change in the chemical potential. Instead, we limit the chemical potential in Eq. (69) to the excess energy induced by the pump (shown in Eq. (31)). We also incorporate non-parabolicity effects by using the expressions for the carrier densities at each valley given by Menéndez et al.:[102]

$$n_{\Gamma}(T) = \frac{1}{4} \left( \frac{2m_{\Gamma} k_{\rm B} T}{\pi \hbar^2} \right)^{3/2} \left[ F_{1/2} \left( \frac{\mu - E_0}{k_{\rm B} T} \right) + \frac{15}{8} \left( \frac{k_{\rm B} T}{\Delta_{\Gamma}} \right) F_{3/2} \left( \frac{\mu - E_0}{k_{\rm B} T} \right) \right]$$
(71a)

$$n_{\rm L}(T) = \left(\frac{2m_{\rm L}k_{\rm B}T}{\pi\hbar^2}\right)^{3/2} \left[F_{1/2}\left(\frac{\mu - E_{\rm ind}}{k_{\rm B}T}\right) + \left(\frac{k_{\rm B}T}{\Delta_{\rm L}}\right)F_{3/2}\left(\frac{\mu - E_{\rm ind}}{k_{\rm B}T}\right)\right]$$
(71b)

$$n_{\Delta}(T) = \frac{3}{2} \left( \frac{2m_{\Delta}k_{\rm B}T}{\pi\hbar^2} \right)^{3/2} \left[ F_{1/2} \left( \frac{\mu - E_{\Delta}}{k_{\rm B}T} \right) \right],$$
 (71c)

where the terms  $\Delta_{\Gamma} = (3/2)[2/E_0 + 1/(E_0 + \Delta_0)]^{-1}$  and  $\Delta_{L} = [1/E_1 + 1/(E_1 + \Delta_1)]^{-1}$  are the characteristic non-parabolicity energies. With the chemical poten-

tial limited by the excess energy of the pump, the argument of the Fermi integrals in Eq. (71a) becomes  $F_j(E_e/k_{\rm B}T_e)$ . Figure 24 shows the carrier density at the  $\Gamma$ -valley as a function of the effective carrier temperature. Again, this temperature is calculated using Eq. (67). Because electrons quickly scatter to the L- or X-valley (at a rate of up to  $10^{14}$  s<sup>-1</sup>), we do not expect saturation of carriers at the  $\Gamma$ -valley.[103] Therefore, to account for the additional carriers enabled by intervalley scattering, we also plot  $2 \times n_{\Gamma}(T)$ , the same density of Eq. (71a) multiplied by 2. The result is a density range between  $5 \times 10^{19}$  and  $10^{20}$  cm<sup>-3</sup> at an effective carrier temperature of about 2500 K.

With this carrier density estimate, we include intervalley scattering by summing the carrier densities across all valleys,

$$n_e(T) = n_L(T) + n_\Gamma(T) + n_X(T),$$
 (72)

where  $n_{\rm L}(T)$ ,  $n_{\rm T}(T)$ , and  $n_{\rm X}(T)$  are given by Eq. (71). Since we know the effective temperature of the carriers, we can solve for the chemical potential  $\mu$  in Eq. (72) as a function of temperature in the same manner as before. It is important to remark that, independently of the relative density of carriers at each valley, the chemical potential is the same for all valleys. We make this assumption based on the discussions of Ref. [103, 104]. Plot (a) in Figure 25 shows the chemical potential as a function of the carrier temperature for the estimated densities (5 × 10<sup>19</sup> and  $10^{20}$  cm<sup>-3</sup>). At low temperatures, the chemical potential lies above the indirect

bandgap, as expected and shown in Figure 23. At higher temperature, however, the chemical potential drops below the bandgap. We can interpret this as follows: elevated temperatures promote a larger number of carriers into states above the chemical potential. Nonetheless, the number of occupied states above the bandgap in the CB remains fixed. As a result, the chemical potential must decrease to allow the presence of carriers above this energy but below the bandgap. The cooling of the initial hot carriers in our experiment should lead to an increase in the chemical potential, as indicated by the curves shown in plot (a). Plot (b) of Figure 25 shows the percentage of carriers at each valley as a function of temperature for the aforementioned carrier densities. At high temperatures, the carriers are roughly equally distributed between the L- and X-valley. However, as the carrier cool down, they relax toward the L-valley. The density at the  $\Gamma$ -valley, on the other hand, remains close to zero at all temperatures. This confirms previous observations of the insignificant role that the central valley plays in allocating carriers. [103] Ultimately, any saturation in the absorption at the  $\Gamma$ -valley is a direct result of the buildup of the population of carriers at the satellite valleys.

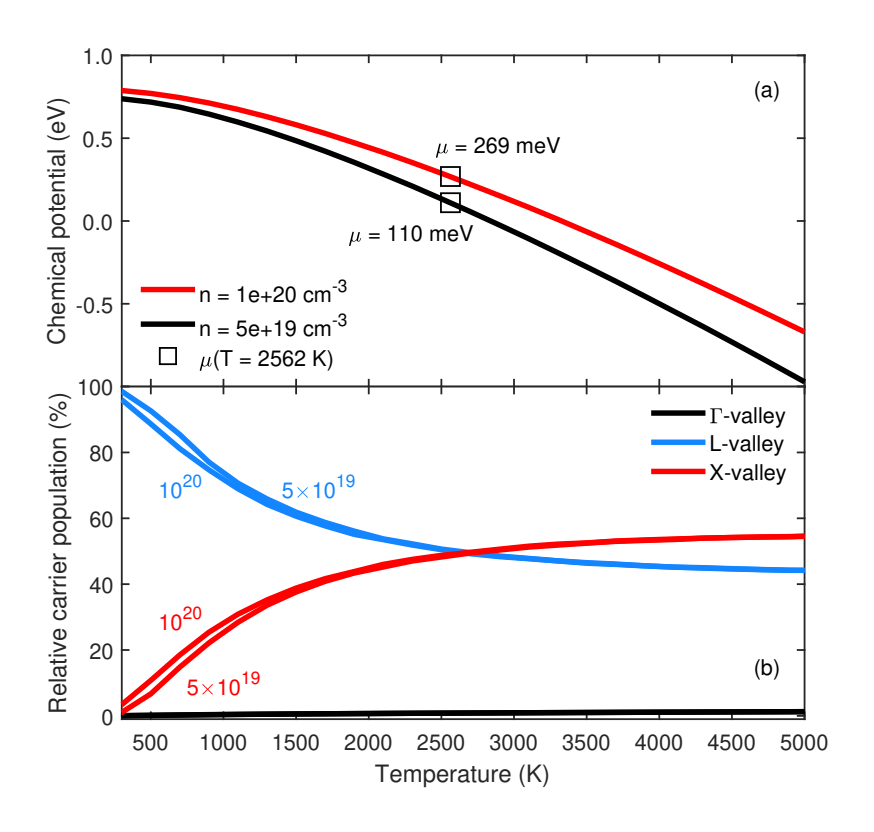


Figure 25: (a) Chemical potential as a function of temperature for a density of  $5 \times 10^{19}$  cm<sup>-3</sup> (black line) and  $10^{20}$  cm<sup>-3</sup> (red line). The squares ( $\square$ ) show the chemical potential at the effective carrier temperature given in Eq. (67). (b) The relative population density  $\Gamma$ -, L-, and X-valley (black, blue, and red line, respectively) with respect to the total density of Eq. (72).

# 5.2.2 Dielectric function

As seen in Figure 10, the VBs run parallel to the CB in the  $\Lambda$ -direction. This creates the van Hove singularities  $E_1$  and  $E_1 + \Delta_1$ . These transitions occur from the

hh and lh band to the CB, respectively. Once the carriers are photo-generated, the interaction between the electron-hole pairs tends to form excitons. Furthermore, because of the joint density of states (JDOS) of these transitions, the excitonic systems for  $E_1$  and  $E_1 + \Delta_1$  are confined to a two-dimensional plane. To describe the optical response for this system, Tanguy provided an expression for the complex DF that incorporates the effects of two-dimensional Wannier excitons. [26] More importantly for the present work, Tanguy's model has already been adapted for the aforementioned CPs of Ge. For the CP  $E_1$ , the DF takes the form [105]

$$\varepsilon(E) = \frac{A}{\pi(E + i\Gamma)^2} \left\{ g_a \left[ \xi(E + i\Gamma) \right] + g_a \left[ \xi(-E - i\Gamma) \right] - 2g_a \left[ \xi(0) \right] \right\}, \tag{73}$$

where

$$A = \frac{4e^2 \mu_{\perp} \overline{P}^2}{3\pi \varepsilon_0 m_0^2} k_{\text{max}}, \quad g_a(\xi) = 2\ln(\xi) - 2\psi\left(\frac{1}{2} - \xi\right), \quad \text{and} \quad \xi(z) = \sqrt{\frac{R}{E_1 - z}}.$$
(74)

In Eq. (74), the amplitude A depends on the electron charge e, the free electron mass  $m_0$ , the permeability of free space  $\varepsilon_0$ , the reduced mass of the two-dimensional exciton  $\mu_{\perp}$ , the average momentum matrix element  $\overline{P}$ , and the maximum wave vector range  $k_{\text{max}}$  where transitions take place, whereas the argument  $\xi$  depends on the exciton's binding energy R and the CP energy  $E_1$ .  $\psi$  is the complex digamma function. Unfortunately, this model is only valid for steady-state measurements and must be modified for non-equilibrium conditions.

To incorporate band-filling effects, we begin with the expression for the imag-

inary part of the dielectric tensor[81, 3]

$$\varepsilon_{2}(E)^{\mu\nu} = \left(\frac{1}{4\pi\varepsilon_{0}}\right) \frac{4\pi^{2}e^{2}\hbar^{2}}{m_{0}^{2}E^{2}} \sum_{CV} \langle V|p_{\mu}|C\rangle\langle C|p_{\nu}|V\rangle$$

$$\times \int \frac{d\mathbf{k}}{4\pi^{3}} \left\{1 - f[E_{C}(\mathbf{k})]\right\} f[E_{V}(\mathbf{k})]\delta(E_{C}(\mathbf{k}) - E_{V}(\mathbf{k}) - E). \tag{75}$$

where  $\langle V | p_{\mu} | C \rangle \langle C | p_{\nu} | V \rangle$  is the element of row  $\mu$  and column  $\nu$  of the momentum transition matrix between the CB state  $|C\rangle$  and VB state  $|V\rangle$ . We have incorporated the occupation probability of the CB and VB states with the Fermi functions  $f[E_{\rm C}(\mathbf{k})]$  and  $f[E_{\rm V}(\mathbf{k})]$ , respectively. Since we are dealing with a cubic system, only the diagonal components of the tensor are non-zero. Therefore, we can replace the dielectric tensor with the dielectric function by averaging the contributing components  $\varepsilon_2 = (\varepsilon_{xx} + \varepsilon_{yy} + \varepsilon_{zz})/3$ . Moreover, from  $\mathbf{k} \cdot \mathbf{p}$  theory, the matrix elements reduce to [106]

$$\sum_{CV} \langle V | p_{\mu} | C \rangle \langle C | p_{\nu} | V \rangle = \underbrace{\left| \langle C | P_{x} | V \rangle \right|^{2}}_{\overline{P}^{2}/2} + \underbrace{\left| \langle C | P_{y} | V \rangle \right|^{2}}_{\overline{P}^{2}/2} + \underbrace{\left| \langle C | P_{z} | V \rangle \right|^{2}}_{0} = \overline{P}^{2}. \quad (76)$$

In addition, we multiply the DF by 4 to account for the L-valley degeneracy. Finally, we set  $f[E_V(\mathbf{k})] \to 1$ , since the VB is full at the L-point. The result is

$$\varepsilon_2(E) = \frac{4\pi e^2 \hbar^2 \overline{P}^2}{3\varepsilon_0 m_0^2 E^2} \int \frac{d\mathbf{k}}{4\pi^3} \left\{ 1 - f[E_{\mathcal{C}}(\mathbf{k})] \right\} \delta\left[ E_{\mathcal{C}}(\mathbf{k}) - E_{\mathcal{V}}(\mathbf{k}) - E \right]. \tag{77}$$

In a cylindrical coordinate system where the x-, y-, and z-axis point along the cubic  $[1\overline{1}0]$ -,  $[11\overline{2}]$ -, and [111]-direction, respectively, the difference between the CB and the VB is given by

$$E_{\rm C}(\mathbf{k}) - E_{\rm V}(\mathbf{k}) = E_1 + \frac{\hbar^2}{2} \left( \frac{k_\rho^2}{\mu_\perp} + \frac{k_z^2}{\mu_\parallel} \right).$$
 (78)

Because the longitudinal reduced effective mass  $\mu_{\parallel}$  in Eq. (78) is significantly greater than the transverse reduced effective mass  $\mu_{\perp}$ , we set  $k_z^2/\mu_{\parallel} \rightarrow 0.[107]$  The DF in Eq. (111) then simplifies to:

$$\varepsilon_2(E) = \frac{4\pi e^2 \hbar^2 \overline{P}^2}{3\varepsilon_0 m_0^2 E^2} \iiint \frac{k_\rho \mathrm{d}k_\rho \mathrm{d}k_\phi \mathrm{d}k_z}{4\pi^3} \left\{ 1 - f[E_{\mathrm{C}}(\mathbf{k})] \right\} \delta\left(E_1 + \frac{\hbar^2 k_\rho^2}{2\mu_\perp} - E\right). \tag{79}$$

Before solving this integral, we note that the only nonzero values of the integral are when  $E_1 + \hbar^2 k_\rho^2 / 2\mu_\perp - E = 0$ . Therefore, by solving for  $k_\rho^2$  in the argument of the delta function, we can express the CB at the L-point as follows:

$$E_{\rm C}(\mathbf{k}) = E_{\rm ind} + \frac{\hbar^2}{2} \left( \frac{k_{\rho}^2}{m_{\perp}} + \frac{k_z^2}{m_{\parallel}} \right)$$

$$= E_{\rm ind} + \frac{\hbar^2 k_z^2}{2m_{\parallel}} + \frac{\hbar^2}{2m_{\perp}} \left[ \frac{2\mu_{\perp}}{\hbar^2} \left( E - E_1 \right) \right]$$

$$= E_{\rm ind} + \frac{\hbar^2 k_z^2}{2m_{\parallel}} + \left( E - E_1 \right) \frac{\mu_{\perp}}{m_{\perp}}, \tag{80}$$

which simplifies  $f[E_{\rm C}(\mathbf{k})] \to f[E_{\rm C}(E,k_z^2)]$ . The integral  $\int \mathrm{d}k_\varphi = 2\pi$  is trivial. To integrate over  $k_\rho$ , we make the substitution  $u = \hbar^2 k_\rho^2/2\mu_\perp$ , which transforms the integral

$$\int_0^\infty k_\rho \mathrm{d}k_\rho \delta \left( E_1 + \frac{\hbar^2 k_\rho^2}{2\mu_\perp} - E \right) \to \frac{\mu_\perp}{\hbar^2} \int_0^\infty \mathrm{d}u \delta \left( E_1 + u - E \right). \tag{81}$$

Evaluating this integral yields the Heaviside step function  $H(E_1-E)$ . The integral over  $k_z$  needs to be limited to the range where the transitions take place  $(k_{\text{max}})$ . The final form of the DF for  $E_1$  is [108, 109]

$$\varepsilon_2(E) = \frac{2e^2 \mu_{\perp}^{(E_1)} \overline{P}^2}{3\pi\varepsilon_0 m_0^2 E^2} H(E - E_1) \int_{-k_{\text{max}}}^{k_{\text{max}}} dk_z \left\{ 1 - f[E_{\text{C}}(E, k_z^2)] \right\}$$
(82)

where  $E_{\rm C}(E,k_z^2)$  is given in Eq. (80).

The DF in Eq. (126) is valid for uncorrelated electron-hole pairs only. We can incorporate excitonic effects into the band-filling model by noting that the integral in Eq. (126) only modifies the amplitude of the DF. Therefore, we can replace the amplitude in the excitonic DF with the one obtained from band-filling considerations. The result for the CP  $E_1$  is

$$\varepsilon_{2}(E) = \frac{2e^{2}\mu_{\perp}^{(E_{1})}\overline{P}^{2}}{3\pi\varepsilon_{0}m_{0}^{2}}\operatorname{Im}\left\{\frac{g_{a}\left[\xi(E+i\Gamma)\right] + g_{a}\left[\xi(-E-i\Gamma)\right] - 2g_{a}\left[\xi(0)\right]}{(E+i\Gamma)^{2}}\right\} \times \int_{-k_{\max}}^{k_{\max}} dk_{z}\left\{1 - f\left[E_{C}(E,k_{z}^{2})\right]\right\},$$
(83)

where  $E_{\rm C}(E,k_z^2)$  is given by Eq. (80), and  $g_a(\xi)$  and  $\xi(z)$  are given in Eq. (74). The real part of Eq. (83) can be computed with a Kramers–Kronig transformation. Our probing region is where the CPs  $E_1$  and  $E_1 + \Delta_1$  are located. Therefore, we require two expressions similar to Eq. (83) to account for both CPs. The CP energies, reduced masses, and exciton binding energies need to be adjusted separately for each CP.

## 5.2.3 Thermal equilibrium

To validate our band-filling model, we need to verify that the shape of Eq. (83) at thermal equilibrium looks identical to Eq. (73). Before we can plot the DF, however, we need to find the chemical potential at room temperature. For the

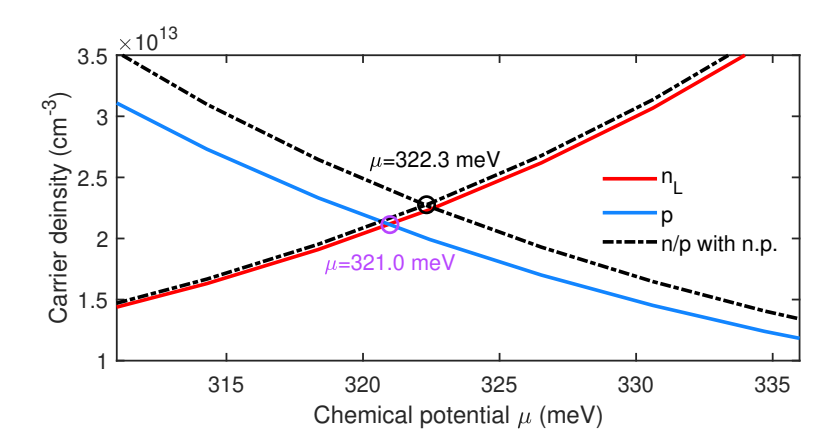


Figure 26: Density of electrons and holes at 300 K as a function of chemical potential in the parabolic (red and blue lines, respectively) and non-parabolic approximation (dot-dashed black lines). The circles ( $\bigcirc$ ) show the corresponding intrinsic chemical potential for both approximations (purple for parabolic and black for non-parabolic approximation).

non-degenerate case at temperature T, the chemical potential is given by [100]

$$\mu = \frac{E_{\rm V} + E_{\rm C}}{2} + \frac{k_{\rm B}T}{2} \ln \left(\frac{m_h}{m_e}\right). \tag{84}$$

At zero temperature, the chemical potential lies halfway between the top of the VB  $E_{\rm V}$  and the bottom of the CB  $E_{\rm C}$ . At room temperature and with no excess of charge carriers, the chemical potential in the degenerate case should reduce to Eq. (84). Nonetheless, it is illustrative to go through the exercise of finding this chemical potential using Fermi-Dirac statistics. For the degenerate case, the parabolic approximation for the density of electrons in the CB is given by

$$n_{\rm L}(T) = \frac{1}{4} \left( \frac{2m_{\rm L}k_{\rm B}T}{\pi\hbar^2} \right)^{3/2} F_{1/2} \left( \frac{\mu - E_{\rm ind}}{k_{\rm B}T} \right),$$
 (85)

which is similar to the density expressed in Eq. (69). The density of Eq. (85), however, gives the density at the L-valley. We use the lower valley because, regardless of the zone in which the carriers were generated, at thermal equilibrium the electrons will lie in the lowest point of the CB. Similarly, the holes will lie in the highest point of the VB. In the case of Ge, these are the L-valley and  $\Gamma$ -point, respectively. Eq. (71b) incorporates non-parabolicity effects to the L-valley density. For the density of the holes, the parabolic approximation is

$$p(T) = \frac{1}{4} \left( \frac{2m_h k_B T}{\pi \hbar^2} \right)^{3/2} F_{1/2} \left( -\frac{\mu}{k_B T} \right), \tag{86}$$

where the DOS mass of the holes is[110]

$$m_h = \left(m_{\rm hh}^{3/2} + m_{\rm lh}^{3/2} + e^{-\Delta_0/k_{\rm B}T} m_{\rm SO}^{3/2}\right)^{2/3}.$$
 (87)

We can also incorporate non-parabolicity effects into the density of holes by using the expressions for the VBs

$$p_{\rm lh}(T) = \frac{1}{4} \left( \frac{2m_{\rm lh}k_{\rm B}T}{\pi\hbar^2} \right)^{3/2} \left[ F_{1/2} \left( -\frac{\mu}{k_{\rm B}T} \right) - 6.0186 \left( k_{\rm B}T \right) \frac{3}{2} F_{3/2} \left( -\frac{\mu}{k_{\rm B}T} \right) + 128.22 \left( k_{\rm B}T \right)^2 \frac{15}{4} F_{5/2} \left( -\frac{\mu}{k_{\rm B}T} \right) \right], \tag{88a}$$

$$p_{\rm hh}(T) = \frac{1}{4} \left( \frac{2m_{\rm hh}k_{\rm B}T}{\pi\hbar^2} \right)^{3/2} \left[ F_{1/2} \left( -\frac{\mu}{k_{\rm B}T} \right) + 3.8263 \left( k_{\rm B}T \right) \frac{3}{2} F_{3/2} \left( -\frac{\mu}{k_{\rm B}T} \right) -4.7446 \left( k_{\rm B}T \right)^2 \frac{15}{4} F_{5/2} \left( -\frac{\mu}{k_{\rm B}T} \right) \right], \tag{88b}$$

$$p_{\rm SO}(T) = \frac{1}{4} \left( \frac{2m_{\rm SO}k_{\rm B}T}{\pi\hbar^2} \right)^{3/2} F_{1/2} \left( -\frac{\Delta_0 + \mu}{k_{\rm B}T} \right),$$
 (88c)

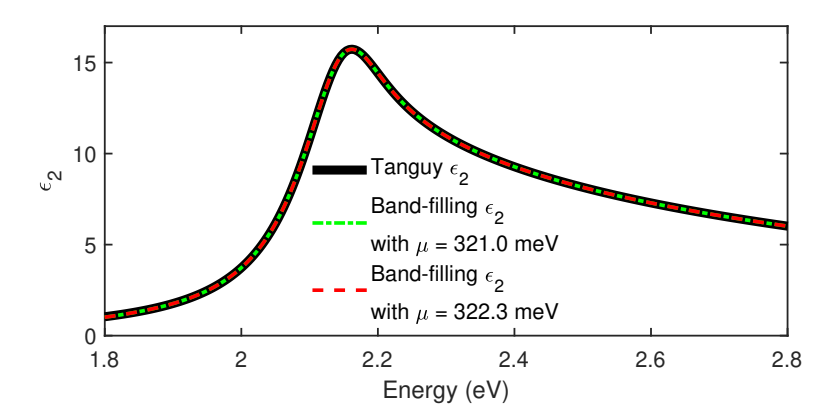


Figure 27: Imaginary part of the two-dimensional excitonic dielectric function (black solid line) along with the band-filling model using the chemical potential in the parabolic and non-parabolic approximation (green dot-dashed and red dashed lines, respectively).

given by Menéndez et al.[102] We then sum over the three VBs:

$$p(T) = p_{\text{lh}}(T) + p_{\text{hh}}(T) + p_{\text{SO}}(T).$$
 (89)

We note that electron and hole densities in an intrinsic semiconductor should be the same. Therefore, we can equate the density of electrons and holes at a constant temperature to find the corresponding chemical potential. Figure 26 shows the density of electrons (red line) and holes (blue line) at room temperature (300 K), along with their corresponding non-parabolicity expressions (black dot-dashed lines). The circles indicate the intrinsic chemical potential for the parabolic (purple) and non-parabolic (black) cases. For reference, in the non-degenerate approximation of Eq. (84), the chemical potential at room temperature is 324.0

eV.

Once we know the intrinsic chemical potential at room temperature, we can evaluate our band-filling model of Eq. (83) and then compare it with the two-dimensional excitonic DF of Eq. (73). Figure 27 shows the steady state DF (black solid line) alongside our band-filling model using the chemical potential obtained from the parabolic and non-parabolic approximations (green dot-dashed and red dashed lines, respectively). As seen in the figure, both models yield equivalent results under thermal equilibrium conditions.

## 5.3 Final model and interpretation

As stated previously, since there are two CPs in the spectral region of interest, we need to combine two expressions similar to Eq. (83). Our final model is

$$\varepsilon_{2}(E) = A^{(E_{1})} \operatorname{Im} \left\{ \frac{g_{a} \left[ \xi^{(E_{1})}(E + i\Gamma) \right] + g_{a} \left[ \xi^{(E_{1})}(-E - i\Gamma) \right] - 2g_{a} \left[ \xi^{(E_{1})}(0) \right]}{\left[ E + i\Gamma^{(E_{1})} \right]^{2}} \right\} \\
\times \int_{-k_{\max}}^{k_{\max}} dk_{z} \left\{ 1 - f \left[ E_{C}^{(E_{1})}(E, k_{z}^{2}) \right] \right\} \\
+ A^{(E_{1} + \Delta_{1})} \operatorname{Im} \left\{ \frac{g_{a} \left[ \xi^{(E_{1} + \Delta_{1})}(E + i\Gamma) \right] + g_{a} \left[ \xi^{(E_{1} + \Delta_{1})}(-E - i\Gamma) \right] - 2g_{a} \left[ \xi^{(E_{1} + \Delta_{1})}(0) \right]}{\left[ E + i\Gamma^{(E_{1} + \Delta_{1})} \right]^{2}} \right\} \\
\times \int_{-k_{\max}}^{k_{\max}} dk_{z} \left\{ 1 - f \left[ E_{C}^{(E_{1} + \Delta_{1})}(E, k_{z}^{2}) \right] \right\}, \tag{90}$$

where

$$A^{(E_1)} = \frac{2e^2\mu_{\perp}^{(E_1)}\overline{P}^2}{3\pi\varepsilon_0 m_0^2}, \ \xi^{(E_1)}(z) = \sqrt{\frac{R^{(E_1)}}{E_1 - z}},$$
 and  $E_{\rm C}^{(E_1)}(E, k_z^2) = E_{\rm ind} + \frac{\hbar^2 k_z^2}{2m_{\parallel}} + (E - E_1)\frac{\mu_{\perp}}{m_{\perp}}$ 

for  $E_1$ , and

$$A^{(E_1+\Delta_1)} = \frac{2e^2\mu_{\perp}^{(E_1+\Delta_1)}\overline{P}^2}{3\pi\varepsilon_0 m_0^2}, \ \xi^{(E_1+\Delta_1)}(z) = \sqrt{\frac{R^{(E_1+\Delta_1)}}{E_1 + \Delta_1 - z}},$$
 and 
$$E_{\rm C}^{(E_1+\Delta_1)}(E, k_z^2) = E_{\rm ind} + \frac{\hbar^2 k_z^2}{2m_{\parallel}} + (E - E_1 - \Delta_1)\frac{\mu_{\perp}}{m_{\parallel}}.$$

for  $E_1 + \Delta_1$ . The real part  $\varepsilon_1$  can be computed with a Kramer-Kronig transformation (typically, e also add a constant offset  $\varepsilon_{\text{off}}$  to the real part of the DF, to account for additional non-resonant contributions from other interband transitions).<sup>[105]</sup> The black curves in Eq. (28) show the imaginary part of the steady state DF for  $E_1$  and  $E_1 + \Delta_1$ . The additional curves in the figure show how the DF changes with chemical potential and temperature as calculated in Sec. 5.2.1. Plot (a) presents the evolution of the DF for a carrier density of  $10^{20}$  cm<sup>-3</sup> and plot (b) for  $5 \times 10^{19}$  cm<sup>-3</sup>. The smaller plots to the right show the corresponding color-matched chemical potential and temperature values for each of the curves.

#### 5.4 Fitting procedure

We now proceed to fit our model to the experimental data. The expression in Eq. (90) has six fitting parameters: carrier temperature  $T_c$ , carrier density n, and energies and broadening of the critical points  $E_1$ ,  $E_1 + \Delta_1$ ,  $\Gamma^{(E_1)}$ , and  $\Gamma^{(E_1+\Delta_1)}$ . At first glance, it might appear that the chemical potential  $\mu$  is another free parameter, however, Eq. (72) restricts the values to be dependent on  $T_c$  and n. Moreover, based on our carrier density estimates in Eq. (5.2.1), the value

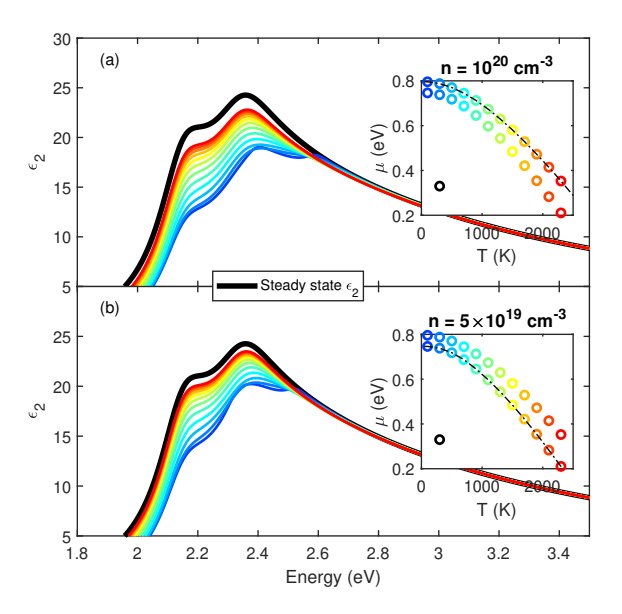


Figure 28: Imaginary part of the dielectric function for the band-filling model shown in Eq. (90). The black solid lines show the steady state dielectric function. The colored curves shows the dielectric function at different points in the evolution of the chemical potential [shown in the circles (o) of the right-side plots]. The temperature and chemical potential for the steady-state DF is shown by the black circle (o) in the right-side plots. (a) presents the evolution of the dielectric function for a density of  $10^{20}$  cm<sup>-3</sup>. (b) shows the same dielectric function for a density of  $5 \times 10^{19}$  cm<sup>-3</sup>.

of the carrier density must be restrained to be between  $5 \times 10^{19}$  and  $10^{20}$  cm<sup>-3</sup>. Conventionally, the energies and broadenings of the critical points are extracted by fitting the second derivative of the DF, rather than the DF itself. In contrast, the change in chemical potential induced by variations in the carrier temperature and

density affects primarily the DF, not its  $2^{nd}$  derivative. Furthermore, to capture the induced reduction in the amplitude of the DF, we need a near perfect match of the fitted model at the critical point absorption peaks.

To overcome these challenges, we introduced the reduced masses  $\mu_{\perp}^{(E_1,E_1+\Delta_1)}$  as additional fitting parameters and divided the fitting process into two steps. Initially, we performed a 2<sup>nd</sup> derivative fitting of Eq. (90) onto the negative delays while holding the chemical potential to its theoretical value at room temperature  $(T_c = 295 \text{ K})$ . This yielded the values for the energies and broadenings of the critical points. Subsequently, we fitted  $\mu_{\perp}^{(E_1,E_1+\Delta_1)}$  to the DF. If any discrepancies in their corresponding 2<sup>nd</sup> derivatives appeared between the model and experimental data, the two-step procedure was repeated until no further change was observed. In this manner, we ensured that the final values of the reduced masses were those required to achieve an accurate fit to both the DF and its second derivative. The obtained values for the reduced masses were  $\mu_{\perp}^{(E_1)} = 0.0566$  and  $\mu_{\perp}^{(E_1+\Delta_1)} = 0.0558$ .

While the energies and broadenings of the critical points may vary with carrier temperature and density, we assume that the reduced masses will remain constant. This assumption is based on the influence that temperature has on the reduced masses. In essence, the reduced masses are only affected by the redshit of the thermal expansion. [44, 105] Hence, they are not directly influenced by the photoexcited carriers. Nevertheless, this additional free parameter is simply an empirical parameter to improve the fittings and should not be overinterpreted.

With this in mind, the positive delay data were fitted using the reduced masses obtained from the previous fitting procedure. As before, the fitting was performed in two steps: First, the critical point energies and broadenings were extracted via  $2^{\text{nd}}$  derivative analysis. Then, the DF itself was fitted using the chemical potential and carrier temperature as the free parameters. This process was repeated iteratively until no further change was observed. Figure 29 (a) and (b) show the experimental data and fitting results for the the imaginary part of the DF  $\varepsilon_2$  from -0.5 ps to 2 ps. The model captures the decrease in the amplitude near the  $E_1$  and  $E_1 + \Delta_1$  CPs very well. In (c), the fitted chemical potential is plotted against carrier temperature.

## 5.5 Carrier relaxation

Figure 30 shows the same fitted chemical potential that is plotted in Figure 29 (c). The figure also shows the theoretical curves of Figure 25 from Sec. 5.2.1 for comparison. The fitted chemical potential (circles) follows the chemical potential for a carrier density of  $10^{20}$  cm<sup>-3</sup> quite closely. At 1 ps, the cooling of the carriers seems to slow down, indicating the relaxation in energy of the electrons to the bottom of the conduction band. By using the relation

$$\left\langle \frac{\mathrm{d}E}{\mathrm{d}t} \right\rangle = 3k_{\mathrm{B}} \left\langle \frac{\mathrm{d}T}{\mathrm{d}t} \right\rangle,$$
 (91)

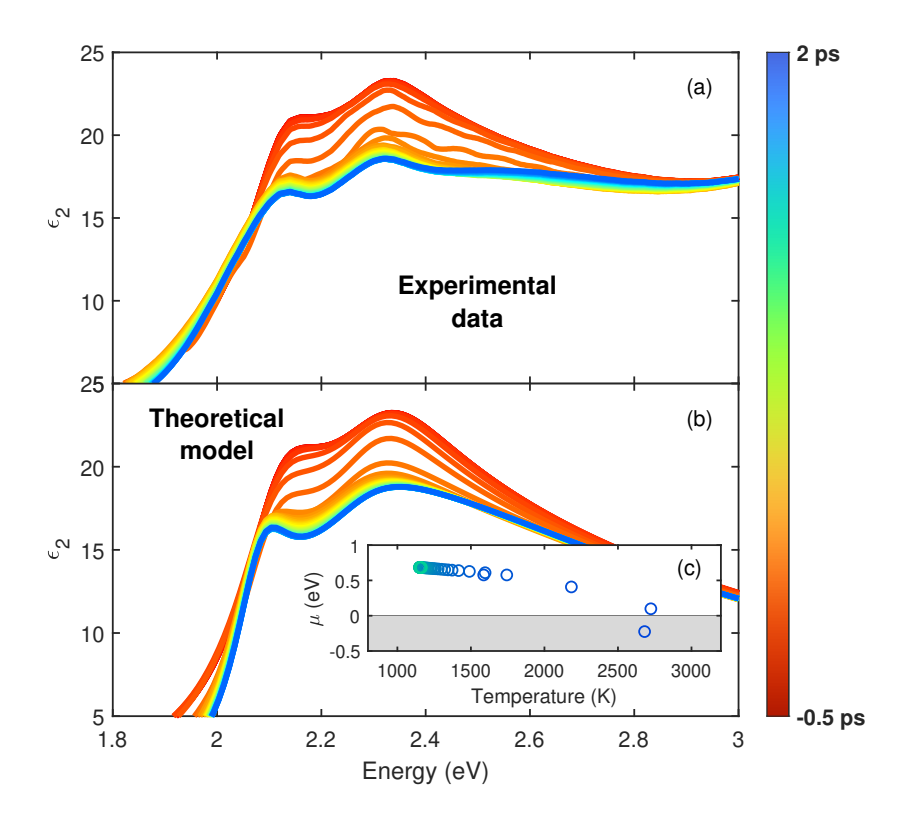


Figure 29: (a) Transient dielectric function of Ge. Delay times range from -0.5 ps up to the first 2 ps. (b) The model shown for the fitted chemical potentials and carrier temperatures. (c) Experimentally fitted chemical potential of the model as a function of the carrier temperature.

we can estimate the energy relaxation rate as a function of delay time, shown in Figure 31. The solid red line shows an exponential fit for these values of the form

$$T_{\rm c}(t) = Ae^{\frac{t-b}{\tau}} + T_0.$$
 (92)

As stated before, the cooling of the carriers comes to a stall at around 1 ps. This is emphasized by the relaxation rate (shown by the green line) calculated with

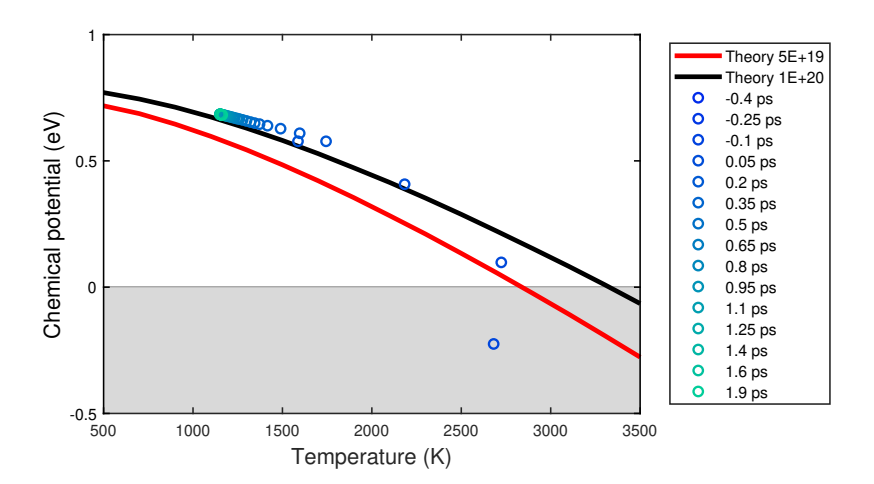


Figure 30: Experimentally fitted chemical potential of the model as a function of the carrier temperature shown by the circles (o). For comparison, the theoretically calculated chemical potential for the carrier densities  $5 \times 10^{19}$  (red line) and  $10^{20}$  cm<sup>-3</sup> (black line).

Eq. (91). At delay times close to zero, we see the highest energy relaxation rate on the order of  $\sim 2 \text{ meV} \cdot \text{fs}^{-1}$ . The phonon branches associated with the intervalley scattering differ for each relaxation pathway (see Figure 22 and 23). At room temperature, forbidden transverse acoustic (TA) and longitudinal optical (LO) phonons dominate the  $\Gamma \to L$  scattering mechanism over the allowed transverse acoustic (TA) phonons.[116, 12] For  $\Gamma \to X$  and  $X \to L$  scattering, the LO and transverse optical (TO) phonon are the dominant branches.[118] At the L-point, the phonon energies range from 8 to 36 meV,[119, 120] whereas for the X-point, phonon energies range from 10 to 34 meV.[120] Quantitatively, we can infer that, at the highest relaxation rate, energy is being dissipated by emitting a phonon

around every 4 to 18 femtoseconds.

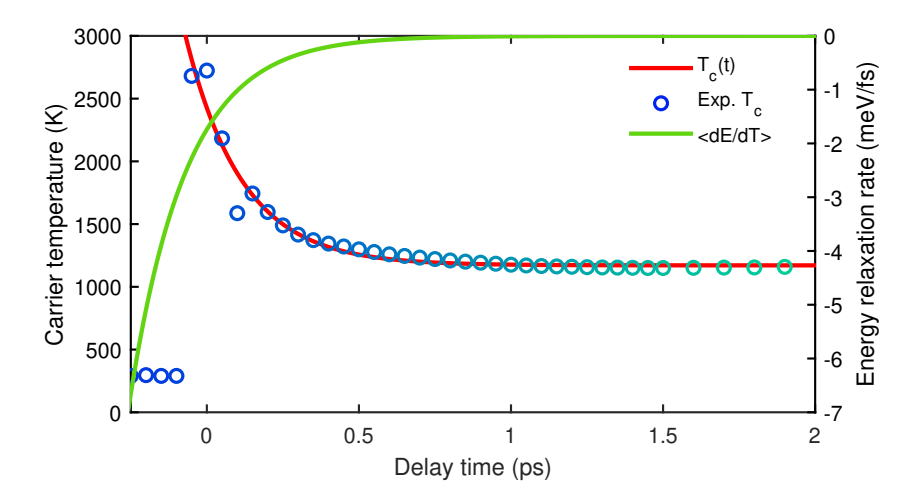


Figure 31: The fitted carrier temperature is shown on the left axis by the circles (o) as a function time delay. These experimentally obtained values are fitted with an exponential function, shown by the red line. On the right axis, the rate of energy relaxation is shown by the green line.

Finally, the fitted energies and boradenings of the CPs are presented in Figure 32. Under equilibrium conditions, the fitted critical point energies were found to be approximately 2.175 eV and 2.37 eV for the  $E_1$  and  $E_1+\Delta_1$  transitions, respectively, with corresponding broadenings of 100 meV and 135 meV. These values are consistent with previously reported room temperature ellipsometry measurements of Ge.<sup>5</sup> Following photoexcitation, the CP energies exhibited a transient red-shift of approximately 25 meV within the first few hundred femtoseconds, consistent with bandgap renormalization effects. As stated in Sec. 2.4.2, the filling of con-

<sup>&</sup>lt;sup>5</sup>See Sec. 4.4.2 and appendix D for the precise values of these parameters.

duction band states tends to have the oppsite effect on the transition energies. However, as discussed in appendix G, band-filling effects do not affect the transition energies for Ge. Hence, we only observe an energy red-shift. The broadenings increased by roughly 30 meV compared to the equilibrium values for  $E_1$  and 10 meV for  $E_1 + \Delta_1$ . This indicates an enhanced scattering and reduced quasiparticle lifetimes during this initial regime. Over the subsequent 3 ps, energies and broadenings for both CPs remain approximately constant.

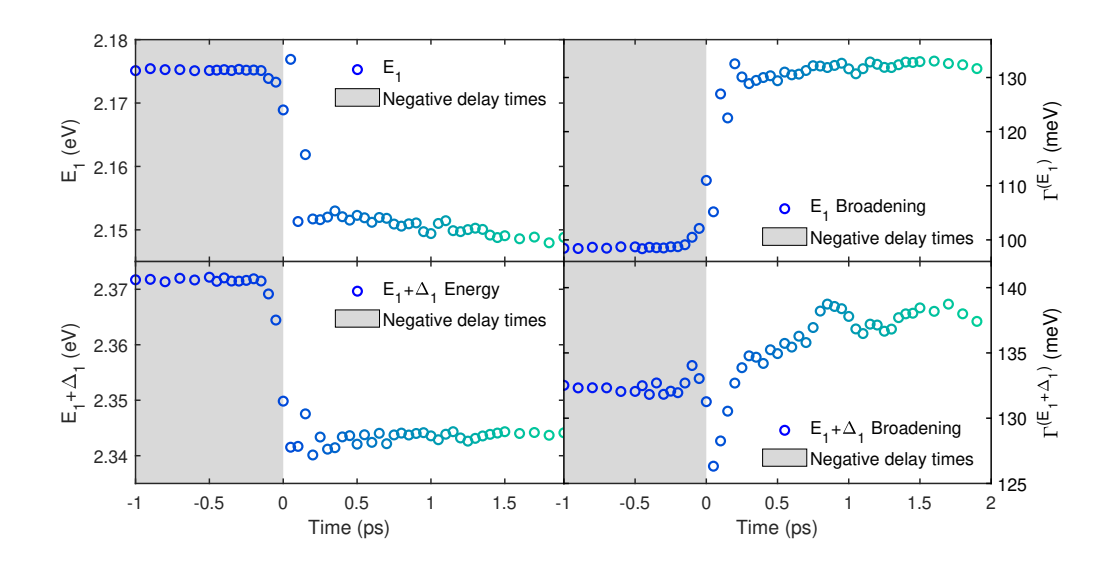


Figure 32: Fitted energy and broadening parameters for the critical points  $E_1$  and  $E_1 + \Delta_1$ . Negative delays (grey area) show the parameters for a steady state measurement.

Overall, the combination of broadband femtosecond ellipsometry measurements and the developed band-filling model provides a comprehensive picture of the ultrafast carrier dynamics in Ge. The extracted time-dependent DF reveals

clear signatures of state filling, bandgap renormalization, and enhanced dephasing during the initial picoseconds following excitation. The temporal evolution of the chemical potential and carrier temperature is consistent with intervalley scattering simulated in the previous sections. These findings establish a quantitative framework for understanding nonequilibrium optical properties in indirect bandgap semiconductors and lay the foundation for further studies of carrier relaxation and excitonic effects under high excitation densities.

#### 6 CONCLUSION AND OUTLOOK

# 6.1 Summary of main findings

In this work, a broadband femtosecond spectroscopic ellipsometry approach was developed and applied to investigate the ultrafast carrier dynamics in Ge. A model incorporating band filling and excitonic effects near the  $E_1$  and  $E_1 + \Delta_1$  CPs was implemented to reconstruct the time dependent DF. The model successfully reproduced the main features of the transient optical response, including the decrease in the amplitude of  $\varepsilon_2$  due to the filling of the bands and red shift of the bandgap renormalization. From the fits, quantitative estimates of carrier temperature, chemical potential, and energy relaxation rates were extracted. These results provide a consistent framework for interpreting the influence of hot carriers on the complex DF.

#### 6.2 Limitations of the model

Although the model captures the principal features of the transient response, several limitations should be mentioned. In particular, the incorporation of excitonic effects was restricted to their equilibrium states. However, at such high carrier densities, Coulomb interaction between electron-hole pairs is screened by the presence of additional carriers. Under strong excitation conditions, screening can significantly reduce exciton binding energies and alter the oscillator strength of the absorption states near CPs.[64] As stated in Sec. 4.5, a solution to the optical response for screening of 2D excitons is yet to be published in the literature. For 3D excitons, the optical response for Ge is given in Eq. (121), which introduces a screening parameter g. Figure 33 shows the effects of excitonic screening on the imaginary part of the DF. Excitonic screening increases as the value of g decreases. The figure indicates that the reduction on the amplitude of  $\varepsilon_2$  should be induced excitonic screening in addition to band-filling effects. A more sophisticated model is needed to account for these additional effects.

Moreover, the high carrier densities induce a transition of the carriers to an electron-hole plasma. There exists several formulas for the value of the density limit that induces this transition (known as **Mott density**). Additionally, the model assumes a single effective carrier temperature and Fermi–Dirac distribution at each time delay, thereby ignoring possible non-thermal carrier distributions

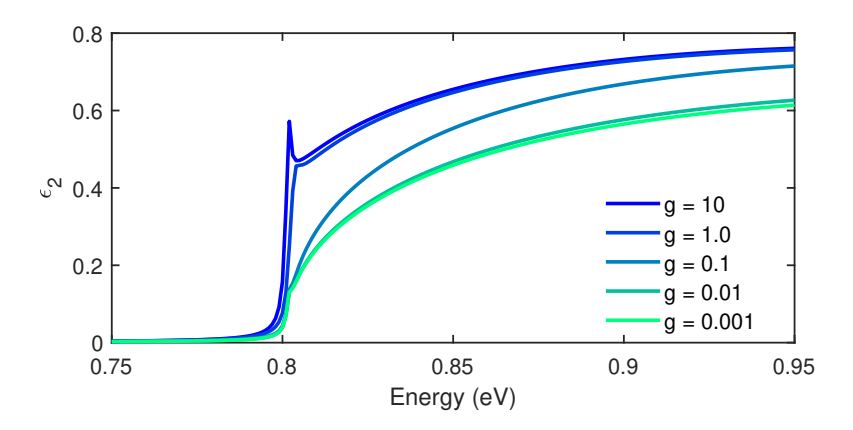


Figure 33: Imaginary part of the dielectric function for the screening of 3D excitons shown in Eq. (121). Smaller values of g give greater excitonic screening. immediately after excitation. These simplifications, while necessary for our model, limit the ability to describe the optical response in the earliest relaxation stages.

### 6.3 Future work

Several directions remain for improving and extending this study. First, measurements over longer delay times beyond 3 ps would enable characterization of carrier recombination and trapping dynamics, as well as recovery of excitonic absorption features. Second, performing measurements varying pump energy and excitation density would allow a more systematic assessment of screening effects, bandgap renormalization, and many-body interactions. Incorporating a dynamic excitonic model that explicitly accounts for screening and binding energy reduction is another important objective for refining the accuracy of the extracted carrier parameters. Finally, extension of the technique to lower temperatures could help disentangle phonon-limited relaxation from intervalley scattering contributions.

#### 6.4 Preliminary results on additional samples

To explore the applicability of this approach to other materials of interest, preliminary measurements were performed on three additional samples: a Ge film on a Si substrate, doped Ge on a Ge film on a Si substrate, and GeSn alloy on a Si substrate. All measurements had similar settings to the bulk Ge measurement. Table 2 shows the nominal thickness (and the thickness determined with WVASE32), power of the pump, and beam-spot diameter. After extracting the ellipsometric angles, we corrected for the effects of the oxide surface overlayer in all samples using the same GeO<sub>2</sub> model. Future work should probe the additional complexities that arises from strain-induced shifts in the CP energies, substrate contributions to the measured signal, and alloy disorder broadening in GeSn.

Sample	Film thickness (nm)	Power (mW)	Beam diameter $(\mu m)$
Doped Ge on Ge on Si	200(169)	1.0	270
Ge on Si	600(661)	5.0	586
$\mathrm{Ge}_{0.908}\mathrm{Sn}_{0.092}$ on Si	345(344)	1.0	241

Table 2: Samples with the pump power and beam diameter used for the measurement. The thickness in parenthesis was determined with WVASE32.

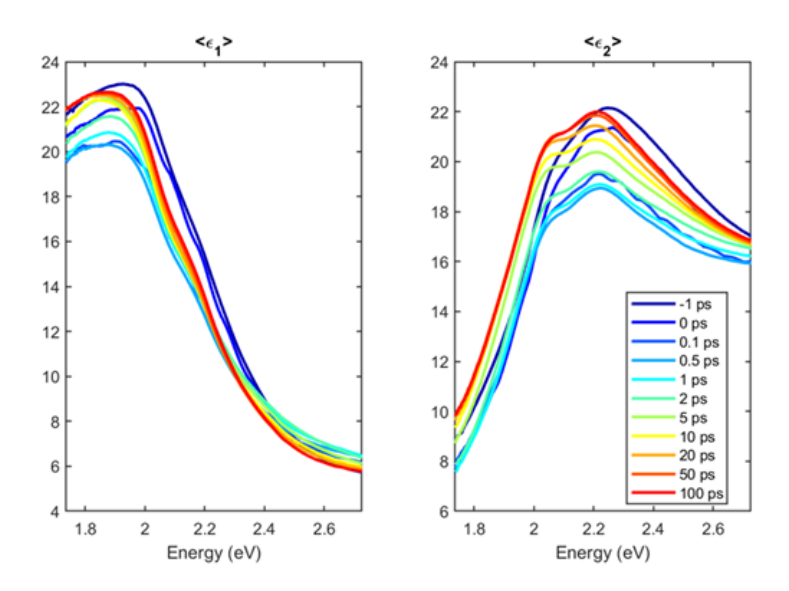


Figure 34: Transient dielectric function of 200 nm of n-dopped Ge on 840 nm of Ge on Si (001). The time delays show data from -1 to 100 ps.

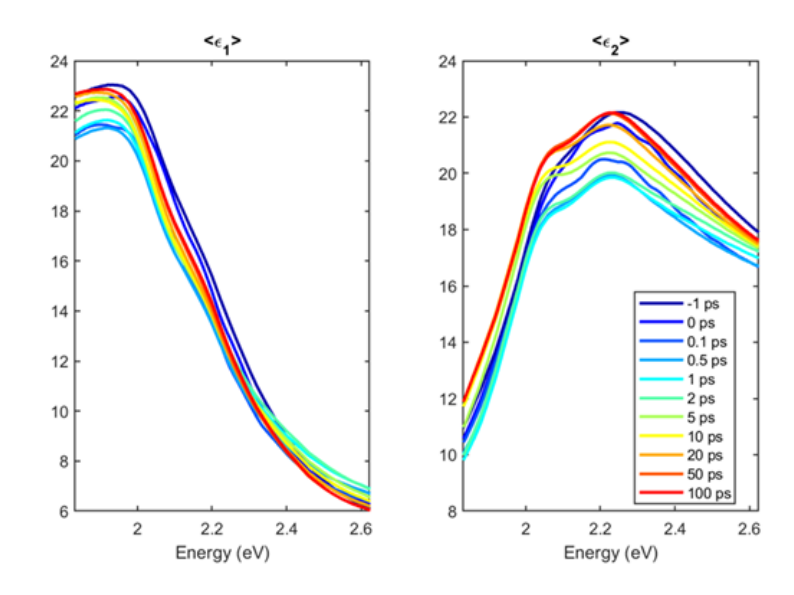


Figure 35: Transient dielectric function 345 nm of  $Ge_{0.908}Sn_{0.092}$  on Si (001). The time delays show data from -1 to 100 ps.

# 6.5 Conclusion

In conclusion, the present work establishes broadband femtosecond ellipsometry as a powerful technique for probing ultrafast carrier dynamics in semiconductors. The results provide quantitative insight into the optical response of band filling, intervalley scattering, and excitonic effects in Ge, while highlighting areas where more comprehensive modeling of excitonic screening and many-body effects is needed. Future measurements to additional materials and excitation regimes will further advance the understanding of nonequilibrium processes crucial for the progress of the field.

#### **APPENDIX**

## A Effective masses

#### A.1 Parabolic approximation at the L-point

The  $E_1$  and  $E_1 + \Delta_1$  critical points (CPs) presented in Fig. 10 arise from interband transitions taking place from the heavy-hole ( $L_4^- \oplus L_5^-$ -band) and light-hole ( $L_6^-$ -band) valence band (VB) to the  $L_6^+$  conduction band (CB), respectively. The symmetries associated with these bands correspond to the set of wave function basis vectors[81, 106]

$$L_{6}^{+}: \qquad |Z\uparrow\rangle, |Z\downarrow\rangle,$$

$$L_{4}^{-} \oplus L_{5}^{-}: \qquad \frac{1}{\sqrt{2}}|X+iY\uparrow\rangle, \frac{1}{\sqrt{2}}|X-iY\downarrow\rangle,$$

$$L_{6}^{-}: \qquad \frac{1}{\sqrt{2}}|X+iY\downarrow\rangle, \frac{1}{\sqrt{2}}|X-iY\uparrow\rangle.$$

$$(93)$$

Just like in Sec. 4.1, the z-axis was chosen along the  $\Lambda$ -direction. In this basis, and with the aid of  $\mathbf{k} \cdot \mathbf{p}$  theory, we can explicitly calculate the matrix  $\langle u_{n\mathbf{0}} | \mathbf{k} \cdot \mathbf{p} | u_{n'\mathbf{0}} \rangle$  to get an expression for the effective masses of the bands (n is the index of the band). We note that the only non-zero momentum matrix elements are [81, 106]

$$-i\langle Z|p_x|X\rangle = -i\langle Z|p_Y|Y\rangle = \overline{P}.$$
(94)

Naturally, the states in (93) with opposite spins will not couple. Hence, the 6-band  $\mathbf{k} \cdot \mathbf{p}$  Hamiltonian will become a  $3 \times 3$  matrix represented as follows:[81, 106]

$$\langle u_{n0} | \mathbf{k} \cdot \mathbf{p} | u_{n'0} \rangle = \begin{bmatrix} \langle L_6^+ | \mathbf{k} \cdot \mathbf{p} | L_6^+ \rangle & \langle L_6^+ | \mathbf{k} \cdot \mathbf{p} | L_4 \rangle & \langle L_6^+ | \mathbf{k} \cdot \mathbf{p} | L_6^- \rangle \\ \langle L_4 | \mathbf{k} \cdot \mathbf{p} | L_6^+ \rangle & \langle L_4 | \mathbf{k} \cdot \mathbf{p} | L_4 \rangle & \langle L_4 | \mathbf{k} \cdot \mathbf{p} | L_6^- \rangle \\ \langle L_6^- | \mathbf{k} \cdot \mathbf{p} | L_6^+ \rangle & \langle L_6^- | \mathbf{k} \cdot \mathbf{p} | L_4 \rangle & \langle L_6^- | \mathbf{k} \cdot \mathbf{p} | L_6^- \rangle \end{bmatrix}$$

$$= \begin{bmatrix} 0 & \frac{i\overline{P}}{\sqrt{2}} k_{\perp} & \frac{i\overline{P}}{\sqrt{2}} k_{\perp} \\ -\frac{i\overline{P}}{\sqrt{2}} k_{\perp} & 0 & 0 \\ -\frac{i\overline{P}}{\sqrt{2}} k_{\perp} & 0 & 0 \end{bmatrix}. \tag{95}$$

Since the only matrix elements that are nonzero are perpendicular to  $|Z\rangle$ , the wave vector  $\mathbf{k}$  reduces to  $k_{\perp}$  and the motion of the carriers gets restricted to a two-dimensional plane. The full Hamiltonian is given by [81, 106]

$$\mathcal{H}_{\mathbf{0}} + \tilde{\mathcal{H}}_{\mathbf{k}} = \begin{bmatrix} E_{1} & \frac{i\hbar\overline{P}}{m_{0}\sqrt{2}}k_{\perp} & \frac{i\hbar\overline{P}}{m_{0}\sqrt{2}}k_{\perp} \\ -\frac{i\hbar\overline{P}}{m_{0}\sqrt{2}}k_{\perp} & 0 & 0 \\ -\frac{i\hbar\overline{P}}{m_{0}\sqrt{2}}k_{\perp} & 0 & -\Delta_{1} \end{bmatrix}.$$
(96)

After diagonalizing the matrix (96), we get the characteristic equation

$$\tilde{E}^{3} - (E_{1} - \Delta_{1}) \,\tilde{E}^{2} - \left(E_{1} \Delta_{1} + \frac{\hbar^{2} \overline{P}^{2} k_{\perp}^{2}}{m_{0}^{2}}\right) \tilde{E} - \frac{\hbar^{2} \overline{P}^{2} k_{\perp}^{2} \Delta_{1}}{2m_{0}^{2}} = 0, \tag{97}$$

where  $\tilde{E} = E - \hbar^2 k^2 / 2m_0$  is the modified energy parameter introduced by Kane[111] (where the kinetic energy of the free electron has been subtracted). For small values of  $k_{\perp}$ , we can solve Eq. (97) perturbatively to get the 3 solutions (one for

each band):[11, 53]

$$E_{\rm CB} = E_1 + \frac{\hbar^2 k_\perp^2}{2} \left[ \frac{1}{m_0} + \frac{E_P}{m_0} \left( \frac{1}{E_1} + \frac{1}{E_1 + \Delta_1} \right) \right]$$
(98)

$$E_{\rm hh} = \frac{\hbar^2 k_{\perp}^2}{2} \underbrace{\left(\frac{1}{m_0} - \frac{E_P}{m_0 E_1}\right)}_{1/(\frac{L_A^- \oplus L_5^-)}{2}} \tag{99}$$

$$E_{\rm lh} = -\Delta_1 + \frac{\hbar^2 k_\perp^2}{2} \left[ \frac{1}{m_0} - \frac{E_P}{m_0 (E_1 + \Delta_1)} \right]$$

$$\frac{1/m_\perp^{(L_6^-)}}{}$$
(100)

To simplify the notation, we have made the substitution  $E_P = \overline{P}^2/m_0$ . Systems of correlated electron-hole pairs generated at the L-point will have a transverse reduced effective mass:[106]

$$\mu_{\perp}^{(E_1)} = \left[ \frac{1}{m_{\perp}^{(L_6^+)}} - \frac{1}{m_{\perp}^{(L_4^- \oplus L_5^-)}} \right]^{-1} = \left[ \frac{E_P}{m_0} \left( \frac{2}{E_1} + \frac{1}{E_1 + \Delta_1} \right) \right]^{-1}$$
(101)

and 
$$\mu_{\perp}^{(E_1 + \Delta_1)} = \left[ \frac{1}{m_{\perp}^{(L_6^+)}} - \frac{1}{m_{\perp}^{(L_6^-)}} \right]^{-1} = \left[ \frac{E_P}{m_0} \left( \frac{1}{E_1} + \frac{2}{E_1 + \Delta_1} \right) \right]^{-1}$$
 (102)

corresponding to the two CPs  $E_1$  and  $E_1 + \Delta_1$ , respectively.

# A.2 Non-parabolicity at the L-point with small spin-orbit interaction

Instead of approximating for small values of  $k_{\perp}$ , we can solve the characteristic Eq. (97) exactly with Vieta's solution for a cubic equation. These solutions, however, are not useful for our purposes given that they cannot be inverted to get the density of states as a function of energy. Instead, we can use the small

spin-orbit (SO) approximation by letting  $\Delta_1 \to 0$ . If we do this, the characteristic equation becomes

$$\tilde{E}^3 - E_1 \tilde{E}^2 - \frac{\hbar^2 k_\perp^2}{m_0} E_P \tilde{E} = 0, \tag{103}$$

with one solution  $\tilde{E}_{\rm hh}=0$ , and the other two

$$\tilde{E}_{\text{CB,lh}} = \frac{E_1 \pm \sqrt{E_1^2 + 4\frac{\hbar^2 k_{\perp}^2}{m_0} E_P}}{2}.$$
(104)

We can expand the square roots in Eq. (104) in  $k_{\perp}^2$  to obtain

$$E_{\text{CB}} = E_{1} + \frac{\hbar^{2}k_{\perp}^{2}}{2m_{0}} + \frac{E_{1}}{2} \left( 1 + \sqrt{1 + \frac{4\hbar^{2}k_{\perp}^{2}}{m_{0}}} \frac{E_{P}}{E_{1}^{2}} \right)$$

$$\approx E_{1} + \frac{\hbar^{2}k_{\perp}^{2}}{2m_{0}} \left( 1 + \frac{E_{P}}{E_{1}} - \frac{\hbar^{2}k_{\perp}^{2}}{2m_{0}} \frac{E_{P}^{2}}{E_{1}^{3}} + 2\frac{\hbar^{4}k_{\perp}^{4}}{2m_{0}^{2}} \frac{E_{P}^{3}}{E_{1}^{5}} \right)$$

$$E_{\text{lh}} = \frac{\hbar^{2}k_{\perp}^{2}}{2m_{0}} + \frac{E_{1}}{2} \left( 1 - \sqrt{1 + \frac{4\hbar^{2}k_{\perp}^{2}}{m_{0}} \frac{E_{P}}{E_{1}^{2}}} \right)$$

$$\approx \frac{\hbar^{2}k_{\perp}^{2}}{2m_{0}} \left( 1 - \frac{E_{P}}{E_{1}} + \frac{\hbar^{2}k_{\perp}^{2}}{2m_{0}} \frac{E_{P}^{2}}{E_{1}^{3}} - 2\frac{\hbar^{4}k_{\perp}^{4}}{2m_{0}^{2}} \frac{E_{P}^{3}}{E_{1}^{5}} \right).$$

$$(105)$$

FIG. 36 shows the bands of the exact solution, the parabolic, and the small SO approximation. The CB in the small SO approximation is almost identical to the 6-band solution. For the lh-band, the curvature of the small SO approximation is similar to the exact solution, however, the parabolic approximation is in better agreement to the exact solution. On the other hand, even in the 6-band model solution, the hh-band shows the wrong curvature. The band seems almost flat, indicating a nearly infinite transverse mass. Cardona states that including non-parabolicity terms linear in  $k_{\perp}$  make the transverse reduce mass for  $E_1$  infinite.[56] However, this is in the  $\Lambda$ -region (and not at the L-valley). Unfortunately, this

solution does not resemble what we see in  $\mathbf{k} \cdot \mathbf{p}$ -theory calculations with higher number of bands.[108] Further calculations probing not only the bottom of the L-valley, but also the  $\Lambda$ -direction away from the L-valley are needed.

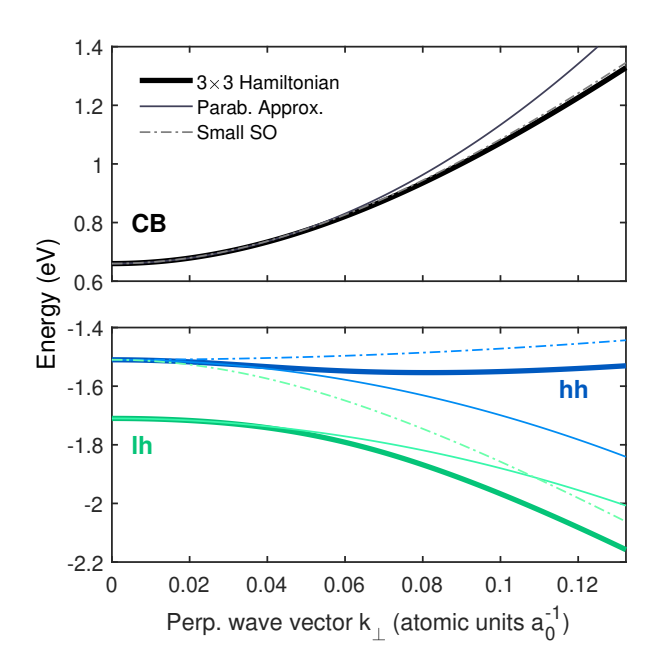


Figure 36: Band structure of Ge at the L-valley. The perpendicular  $k_{\perp}$ -vector is shown in atomic units where  $a_0 = 0.53$  Å. The thick solid lines represent the exact solution to the  $3 \times 3$  Hamiltonian in Eq. (96), the thin solid lines show the parabolic approximation, and the dot-dashed lines are the small spin-orbit approximation.

# B Dielectric function of Ge

Previous attempts to describe the CPs of interest give the line shape of the DF as a step function[106]

$$\varepsilon_2^{(E_1)} = \left(\frac{1}{4\pi\varepsilon_0}\right) \frac{16k_{\text{max}}e^2 \overline{P}^2 \mu_{\perp}^{(E_1)}}{3m_0^2 E^2} H(E_1 - E), \tag{107a}$$

$$\varepsilon_2^{(E_1 + \Delta_1)} = \left(\frac{1}{4\pi\varepsilon_0}\right) \frac{16k_{\text{max}}e^2\overline{P}^2 \mu_{\perp}^{(E_1 + \Delta_1)}}{3m_0^2 E^2} H(E_1 + \Delta_1 - E), \tag{107b}$$

where H is the Heaviside step function,  $k_{\text{max}}$  is the maximum range in the k-axis where transitions take place, and  $\overline{P}$  is the average momentum matrix element.[108, 109] The real part  $\varepsilon_1$  can be calculated from the expression for  $\varepsilon_2$  with a Kramers-Kronig transformation. Alternatively, Humlíček gives the full expression for the DF while adding broadening to Eq. (107) as[107]

$$\varepsilon^{(E_1)}(E) = -\left(\frac{1}{4\pi\varepsilon_0}\right) \frac{16k_{\text{max}}e^2\overline{P}^2\mu_{\perp}^{(E_1)}}{3m_0^2\pi E^2} \ln\left[\frac{2(E_1 - i\Gamma - E)}{E_1 - i\Gamma}\right], \qquad (108a)$$

$$\varepsilon^{(E_1 + \Delta_1)}(E) = -\left(\frac{1}{4\pi\varepsilon_0}\right) \frac{16k_{\text{max}}e^2\overline{P}^2\mu_{\perp}^{(E_1 + \Delta_1)}}{3m_0^2\pi E^2} \ln\left[\frac{2(E_1 + \Delta_1 - i\Gamma - E)}{E_1 + \Delta_1 - i\Gamma}\right]. \qquad (108b)$$

Eqs. (108) give the DF for uncorrelated electron-hole pairs shown by the blue dashed lines in Figure 12.

In the following, we briefly describe how to derive Eq. (107a). We start by computing the amplitude in Eq. (73) for the  $E_1$  CP of Ge from the expression for the imaginary part of the dielectric tensor[81, 3]

$$\varepsilon_2(E)^{\mu\nu} = \left(\frac{1}{4\pi\varepsilon_0}\right) \frac{4\pi^2 e^2 \hbar^2}{m_0^2 E^2} \sum_{CV} \langle V|p_\mu|C\rangle \langle C|p_\nu|V\rangle \int \frac{d\mathbf{k}}{4\pi^3} \delta(E_C(\mathbf{k}) - E_V(\mathbf{k}) - \hbar\omega). \tag{109}$$

Since we are dealing with a cubic system, only the diagonal components of the tensor are non-zero. Therefore, we can replace the dielectric tensor with the dielectric function by averaging the contributing components  $\varepsilon_2 = (\varepsilon_{xx} + \varepsilon_{yy} + \varepsilon_{zz})/3$ . Moreover, from  $\mathbf{k} \cdot \mathbf{p}$  theory, the matrix elements reduce to [106]

$$\sum_{CV} \langle V | p_{\mu} | C \rangle \langle C | p_{\nu} | V \rangle = \underbrace{\left| \langle C | P_{x} | V \rangle \right|^{2}}_{\overline{P}^{2}/2} + \underbrace{\left| \langle C | P_{y} | V \rangle \right|^{2}}_{\overline{P}^{2}/2} + \underbrace{\left| \langle C | P_{z} | V \rangle \right|^{2}}_{0} = \overline{P}^{2}, \quad (110)$$

hence we can replace the matrix element in Eq. (109) with the average transition matrix element  $\overline{P}$ . Finally, we multiply the DF by 4 to account for the L-valley degeneracy. The result is

$$\varepsilon_2(E) = \left(\frac{1}{4\pi\varepsilon_0}\right) \frac{4\pi^2 e^2 \hbar^2}{m_0^2 E^2} \left(\frac{4\overline{P}^2}{3}\right) \int \frac{d\mathbf{k}}{4\pi^3} \delta(E_{\mathcal{C}}(\mathbf{k}) - E_{\mathcal{V}}(\mathbf{k}) - \hbar\omega). \tag{111}$$

To solve the integral in Eq. (111), we replace it with the JDOS in Eq. (78) and switch to cylindrical coordinates. In the new coordinate system, the DF looks like

$$\varepsilon_2(E) = \left(\frac{1}{4\pi\varepsilon_0}\right) \frac{16\pi^2 e^2 \overline{P}^2 \hbar^2}{3m_0^2 E^2} \iiint \frac{k_\rho \mathrm{d}k_\rho \mathrm{d}k_\varphi \mathrm{d}k_z}{4\pi^3} \delta\left(E_1 + \frac{\hbar^2 k_\rho^2}{2\mu_\perp} - E\right). \tag{112}$$

The integral  $\int dk_{\varphi} = 2\pi$  is trivial. To integrate over  $k_{\rho}$ , we make the substitution  $u = \hbar^2 k_{\rho}^2 / 2\mu_{\perp}$ , which transform the integral

$$\int_0^\infty k_\rho \mathrm{d}k_\rho \delta\left(E_1 + \frac{\hbar^2 k_\rho^2}{2\mu_\perp} - E\right) \to \frac{\mu_\perp}{\hbar^2} \int_0^\infty \mathrm{d}u \delta\left(E_1 + u - E\right). \tag{113}$$

Its solution yields the Heaviside step function  $H(E_1 - E)$ . Finally, the integral over  $k_z$  needs to be limited to the range where the transitions take place. We call this  $k_{\text{max}}$ . The final result for  $E_1$  is

$$\varepsilon_2^{(E_1)} = \frac{A}{E^2} H(E_1 - E), \text{ with } A = \frac{4e^2 \overline{P}^2 \mu_{\perp}^{(E_1)}}{3\pi \varepsilon_0 m_0^2} k_{\text{max}},$$
(114)

which is simply Eq. (107a). Notice the similarity between the amplitudes in Eq. (114) and Eq. (74). These amplitudes are the same if we simply replace the transition matrix element  $\mathbf{e} \cdot \mathbf{M}_{\text{CV}} \to \overline{P}^2 k_{\text{max}}/3$  and multiply by the valley degeneracy (multiply by 4 for L-valley).

#### C Unrenormalized energies

To get the unrenormalized energies of the CPs, we will follow the procedure by Zollner et al. [44] where they give the unrenormalized value for the direct bandgap  $E_0$  as

$$E_0^u(T) = E_0^u(T = 0 \text{ K}) - 3B \left(\frac{\partial E_0^{\text{exp}}}{\partial p}\right)_T \int_0^T \alpha(\theta) d\theta, \tag{115}$$

where the superscript u stands for unrenormalized, B is the bulk modulus,  $\alpha(T)$  is the temperature-dependent thermal expansion coefficient, and p is the pressure. For our purposes, we will replace the unrenormalized energy at zero temperature with the fitted parameter  $E_a$  in the Bose-Einstein model of Eq. (61). The fitted parameters  $E_a$ ,  $E_b$ , and  $\theta_B$  in Table 1 are obtained by fitting the experimental CP energies of Table 3. Fig. 37 (b) shows the experimental energy of the  $E_1$  and  $E_1 + \Delta_1$  CPs as a function of temperature (dot-dashed lines). To subtract the thermal effect, we use the thermal expansion coefficient given by Eq. (60). Menéndez et al. obtained the values in Eq. (54) by fitting the experimental thermal expansion data from Ma and Tse.[42] As an alternative to Eq. (54), we could also use a more sophisticated expression for the thermal expansion coefficient

provided by Roucka et al. as[112]

$$\alpha(T) = \frac{4k_{\rm B}}{a_0^3 B} \left[ \frac{2}{3} \gamma_{\rm TA} \left( \frac{\Theta_{\rm TA}}{T} \right)^2 \frac{e^{\Theta_{\rm TA}/T}}{\left( e^{\Theta_{\rm TA}/T} - 1 \right)^2} + \gamma_{\rm LA} \left( \frac{T}{\Theta_{\rm LA}} \right)^3 \int_0^{\Theta_{\rm LA}/T} \frac{x^4 e^x}{\left( e^x - 1 \right)^2} \mathrm{d}x + \gamma_{\rm opt} \left( \frac{\Theta_{\rm opt}}{T} \right)^2 \frac{e^{\Theta_{\rm opt}/T}}{\left( e^{\Theta_{\rm opt}/T} - 1 \right)^2} \right], \tag{116}$$

where  $a_0 = 5.6568$  Å is the lattice constant,[113]  $\gamma$  is the Grüneisen parameter, and  $\Theta$  is the Debye temperature. The subscripts LA, TA, and opt stand for the longitudinal acoustic, transverse acoustic, and optical modes, respectively. As seen in Fig. 37 (a), the more complicated expression in Eq. (116) yields an almost identical result to Eq. (60). Therefore, we settle on using Eq. (54) for this work. Fig. 37 (a) also shows experimental thermal expansion coefficients from the literature.[114, 115]

The result of the unrenormalized energy in Eq. (115) is shown in Fig. 37 (b) (solid lines). For this calculation, we take the value of  $(\partial E_1/\partial p)_T \approx [\partial (E_1 + \Delta_1)/\partial p]_T$ . We justify this assumption by noting that the SO shift  $\Delta_1$  is related to atomic effects and it is, for the most part, unaffected by the distance of the atoms within the lattice. Finally, Fig. 37 (c) shows the exciton binding energies for both CPs in the left axis (solid lines), as well as the reduced masses on the right axis (dashed lines).

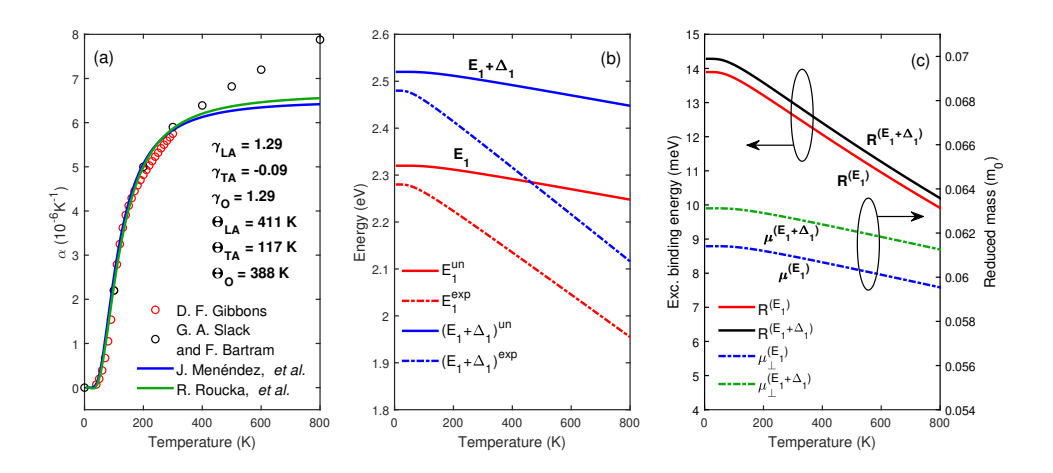


Figure 37: (a) Thermal expansion coefficient from Eq. (60)[38] (blue solid line) and Eq. (116)[112] (green solid line) compared to experimental data ( $\bigcirc$ ).[114, 115] (b) The experimental values for  $E_1$  and  $E_1 + \Delta_1$  (blue and red dot-dashed line, respectively) are shown along with their respective unrenormalized energy (red and blue solid lines, respectively). (c) On the left axis is the binding energy of the excitons of the critical points (black and red solid lines). On the right axis is the transverse reduced effective masses (green and blue dot-dashed lines).

### D Fitting procedure

To suppress the noise of the experimental data, we used a direct space convolution of the experimental DF with a digital filter. The convolution  $\overline{f}$  between f(x) and b(x) has the following property:

$$\overline{f}(x) = \int_{-\infty}^{\infty} \mathrm{d}x' f(x - x') b(x') = \int_{-\infty}^{\infty} \mathrm{d}x' f(x') b(x - x'). \tag{117}$$

Note that, in light of Eq. (117), operations such as  $d\overline{f}(x)/dx$  produce the same outcome whether they act on f(x-x') or b(x-x'). To compute the second derivative of the experimental data, we take full advantage of this property by differentiating the digital filter (an analytical function) instead of the experimental data (a set of discrete points). To perform the convolution, we used MATLAB's built-in function conv(u,v), where u and v are the vectors being convoluted. For the fitting procedure, we created a residual vector function with five free parameters  $[E_1, \Delta_1, \Gamma^{(E_1)}, \Gamma^{(E_1+\Delta_1)}, \text{ and } \varepsilon_{\text{off}}]$ . The two components of this vector function consisted of the real and imaginary part of the experimental 2<sup>nd</sup> derivative of the DF minus the corresponding parts of the numerical derivative of the model:

$$residual = \begin{bmatrix} Re \left\{ \frac{d^{2}\varepsilon^{exp}(E)}{dE^{2}} \right\} - Re \left\{ \frac{d^{2}\varepsilon^{model}(E_{1},\Delta_{1},\Gamma^{(E_{1})},\Gamma^{(E_{1}+\Delta_{1})},\varepsilon_{off},E)}{dE^{2}} \right\} \\ Im \left\{ \frac{d^{2}\varepsilon^{exp}(E)}{dE^{2}} \right\} - Im \left\{ \frac{d^{2}\varepsilon^{model}(E_{1},\Delta_{1},\Gamma^{(E_{1})},\Gamma^{(E_{1}+\Delta_{1})},\varepsilon_{off},E)}{dE^{2}} \right\} \end{bmatrix}.$$
(118)

After creating the residual vector function (118), we minimized it with the MAT-LAB function lsqnonlin(fun,x0,lb,ub), where the input fun is the function to be minimized, x0 is the vector with the initial guess for the fitting parameters, lb, and ub are the vectors with the lower and upper bounds for the fitting parameters, respectively.

Table 3: Value of the fitting parameters and filter width  $\Delta E$  for the extended Gauss digital filter. The step size selected was 1 meV from 1.0 to 3.2 eV (2201 points). (f) indicates a fixed parameter.

T	$\Delta E \text{ (meV)}$	$E_1 \text{ (eV)}$	$E_1 + \Delta_1 \text{ (eV)}$	$\Gamma^{(E_1)} \; (\mathrm{meV})$	$\Gamma^{(E_1+\Delta_1)} \text{ (meV)}$	$arepsilon_{ ext{off}}$
4 K	12.0	$2.2793 \pm 0.0009$	$2.4779 \pm 0.002$	$75 \pm 1$	$96 \pm 2$	6(f)
100 K	14.5	$2.2599 \pm 0.0008$	$2.4600 \pm 0.002$	$79 \pm 1$	$103 \pm 2$	6(f)
200 K	17.5	$2.2187 \pm 0.0009$	$2.4176 \pm 0.002$	$89 \pm 1$	$119 \pm 2$	7(f)
300 K	21.5	$2.1674 \pm 0.0009$	$2.3638 \pm 0.002$	$101\pm1$	$136 \pm 2$	7(f)
400 K	27.5	$2.1167 \pm 0.0006$	$2.3147 \pm 0.002$	$115 \pm 1$	$157 \pm 2$	8(f)
500 K	27.5	$2.0656 \pm 0.0007$	$2.2642 \pm 0.003$	$128\pm1$	$175 \pm 2$	8(f)
600 K	25.0	$2.0172 \pm 0.0009$	$2.2170 \pm 0.003$	$142\pm1$	$193 \pm 3$	8(f)
700 K	33.0	$1.968 \pm 0.001$	$2.1683 \pm 0.004$	$155 \pm 1$	$212 \pm 4$	8(f)
800 K	35.0	$1.917 \pm 0.002$	$2.1182 \pm 0.006$	$171\pm2$	$243 \pm 6$	9(f)

Table 4: Value of the fitting parameters and order of polynomial n for the Savitzky-Golay digital filter. The frame length was constrain to 5% of the number of points (11 points). (f) indicates a fixed parameter.

T	n	$E_1$ (eV)	$E_1 + \Delta_1 \text{ (eV)}$	$\Gamma^{(E_1)} \; (\mathrm{meV})$	$\Gamma^{(E_1+\Delta_1)} \; (\mathrm{meV})$	$arepsilon_{ ext{off}}$
4 K	7	$2.279 \pm 0.002$	$2.478 \pm 0.006$	$76 \pm 3$	$96 \pm 6$	6(f)
100 K	7	$2.260 \pm 0.002$	$2.460 \pm 0.006$	$80 \pm 2$	$103 \pm 5$	6(f)
200 K	7	$2.219 \pm 0.003$	$2.418 \pm 0.005$	$89 \pm 3$	$119 \pm 7$	7(f)
300 K	5	$2.167 \pm 0.003$	$2.364 \pm 0.005$	$102\pm2$	$137 \pm 5$	7(f)
400 K	5	$2.117 \pm 0.002$	$2.315 \pm 0.005$	$116\pm2$	$157 \pm 6$	8(f)
500 K	5	$2.066 \pm 0.002$	$2.264 \pm 0.007$	$129\pm2$	$175 \pm 6$	8(f)
600 K	4	$2.017 \pm 0.002$	$2.217 \pm 0.008$	$142\pm3$	$193 \pm 9$	8(f)
700 K	3	$1.968 \pm 0.003$	$2.17 \pm 0.01$	$155 \pm 3$	$212\pm12$	8(f)
800 K	3	$1.917 \pm 0.006$	$2.12 \pm 0.02$	$171 \pm 6$	$234 \pm 18$	9(f)

## D.1 Extended Gaussian digital filter

The extended Gaussian (EG) digital filter of Eq. (64) for M=4 has the form [48, 49]

$$b_4(x) = \frac{1}{12288\Delta E\sqrt{\pi}} \left( 15120 - \frac{10080x^2}{\Delta E^2} + \frac{1512x^4}{\Delta E^4} - \frac{72x^6}{\Delta E^6} + \frac{x^8}{\Delta E^8} \right) \exp\left(-\frac{x^2}{4\Delta E^2}\right).$$
(119)

However, since we are interested in the  $2^{\rm nd}$  derivative of the data, we can compute the second derivative of Eq. (119) and perform the convolution with  $\varepsilon^{\rm exp}(E)$  afterwards.

$$\frac{\mathrm{d}^2 b_4(x)}{\mathrm{d}x^2} = \frac{1}{49152\Delta E^3 \sqrt{\pi}} \left( -110880 + \frac{188496x^2}{\Delta E^2} - \frac{45936x^4}{\Delta E^4} + \frac{3608x^6}{\Delta E^6} - \frac{106x^8}{\Delta E^8} + \frac{x^{10}}{\Delta E^{10}} \right) \exp\left( -\frac{x^2}{4\Delta E^2} \right).$$
(120)

To select the filter width  $\Delta E$ , we Fourier-transform the experimental data and plot the natural logarithm of the amplitude  $C_n$  of the coefficients as seen Figure 38 (a). We then eliminate the higher order coefficients (noise) and retain the lower ones which preserve the information of the original signal. The same cutoff of the coefficients is also applied to the Fourier transform of the EG filter  $B_4(n)$ , shown in Figure 38 (a) as well. In this figure, we show the Fourier coefficients of the experimental data as a function of the order of coefficients n at 200 K, along with the Fourier transform of the extended Gaussian filter  $B_4(n)$  for two different filter widths. For this particular measurement, we selected the cutoff at the  $31^{\text{st}}$  coefficient. The reader might find this cutoff too conservative and that such a large

filter width could suppress a portion of the signal. To address these concerns, we repeated the fitting procedure with the cutoff at the 41<sup>st</sup> coefficient [see the cyan dash-dotted line in Figure 38 (a)]. We find that including higher-order coefficients increases noise but does not change the fitted energy and broadening parameters beyond their uncertainty. Therefore, we settled with the larger filter width. The dark circles in Figure 38 (b) show the EG derivatives for this measurement. One of the advantages of this method is the increase in the number of points available in the derivative. In our case, the EG filter produces 2201 derivative points, resulting from the chosen energy step size of 1 meV over the range from 1.0 to 3.2 eV. This is in contrast to the Savitsky-Golay (SG) derivative [shown by the red and blue lines in Figure 38 (b)], where the derivative is limited to the number of points of the original signal. Once the filter width has been selected, we can minimize the residual function in Eq. (118) to fit the energy and broadening parameters. Table 3 shows the fitted parameters for this method.

#### D.2 Savitzky-Golay digital filter

To obtain the SG digital filter, we employed the built-in MATLAB function sgolay(m,fl). This function gives a matrix of a finite impulse response smoothing filter. The input m is the polynomial order and fl is the frame length. We used 11 points for the frame length, which is approximately 5% of the total number of data points (this number must be odd). The order of the polynomial is listed in Table 4 for

each temperature series. Once we have generated the SG filter, we can obtain the  $n^{\text{th}}$  derivative by convolving the experimental data with the  $(n+1)^{\text{th}}$  column of the filter matrix. The solid lines in Figure 38 (b) show the SG derivatives for the experimental data at 200 K. Table 4 shows the final values of the fitted parameters with the SG filter. Notice the similarity of the fitted values for energy and broadening between the two filters.

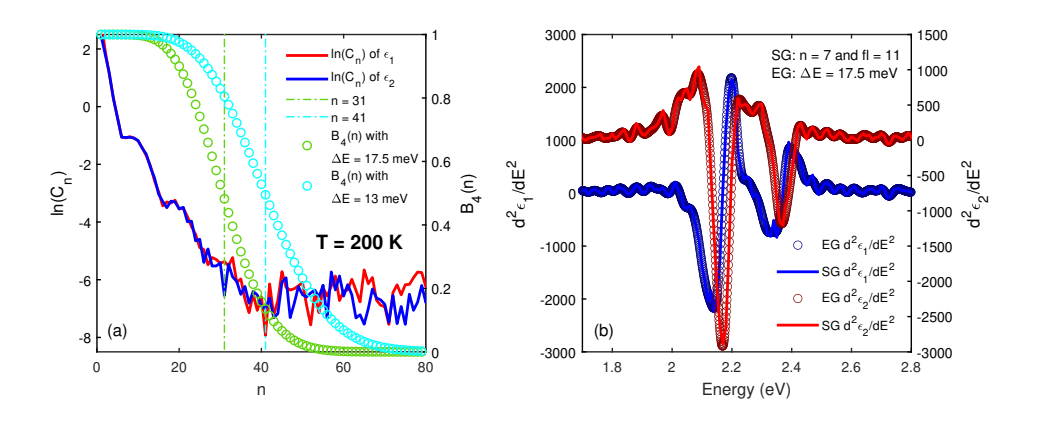


Figure 38: (a) Natural logarithm of the Fourier coefficient amplitude  $C_n$  of the real (red) and imaginary (blue) parts of the dielectric function at 200 K. The same plot also shows the Fourier transform of the extended Gaussian filter ( $\bigcirc$ ) for different filter widths. (b)  $2^{nd}$  derivative of the dielectric function calculated with the extended Gauss filter ( $\bigcirc$ ) and with the Savitzky-Golay filter (solid).

# E Direct bandgap

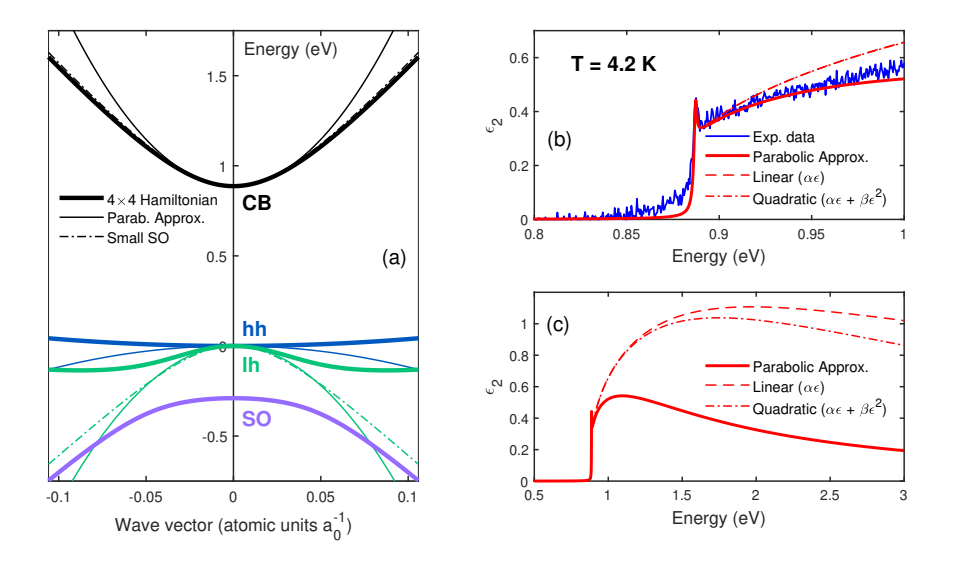


Figure 39: (a) In addition to the parabolic approximation (thin solid line), we show the exact solution (thick solid line) and the small spin-orbit approximation (dot-dashed) to the 8-band model of the band structure of Ge. (b) Imaginary part of the dielectric function at 4 K in the parabolic approximation (solid) and including non-parabolicity linear terms in  $\alpha\epsilon$  (dashed) and quadratic terms in  $\beta\epsilon^2$  (dot-dashed) of the density of states mass. (c) Parabolic (solid) and non-parabolic (dashed, dot-dashed) models extended up to 3 eV.

The lineshape of the  $E_0$  CP was presented previously by Emminger et al. as[70]

$$\varepsilon(E) = \frac{A\sqrt{R}}{\pi(E+i\Gamma)^2} \left\{ \tilde{g} \left[ \xi(E+i\Gamma) \right] + \tilde{g} \left[ \xi(-E-i\Gamma) \right] - 2\tilde{g} \left[ \xi(0) \right] \right\}, \tag{121}$$
 with  $\tilde{g}(\xi) = -2\psi \left( \frac{g}{\xi} \right) - \frac{\xi}{g} - 2\psi \left( 1 - \xi \right) - \frac{1}{\xi}, \ \xi(z) = \frac{2}{\sqrt{\frac{E_0 - z}{R}} + \sqrt{\frac{E_0 - z}{R}} + \frac{4}{g}}, \tag{122}$  and  $A = \frac{e^2 \sqrt{m_0}}{\sqrt{2}\pi\varepsilon_0 \hbar^2} \mu_h^{3/2} \frac{E_P}{3}.$ 

This model is quite similar to Eq. (73), since it also takes into account excitonic (and screening) contributions to the CP. We can improve Eq. (121) by including non-parabolicity contributions to the effective mass at the  $\Gamma$ -point. By following the procedure in Ref. [44] we use the small spin-orbit (SO) coupling approximation to get an analytical expression for the CB effective mass and, therefore, the electron density of states (DOS) mass. If we consider an 8-band model (CB, hh, lh, and SO band), our  $\mathbf{k} \cdot \mathbf{p}$  Hamiltonian looks like[111]

$$\mathcal{H}_{0} + \tilde{\mathcal{H}}_{\mathbf{k}} = \begin{bmatrix} E_{0} & 0 & -\frac{\hbar k}{m_{0}} iP & 0\\ 0 & -\frac{2\Delta_{0}}{3} & \frac{2\Delta_{0}}{3} & 0\\ \frac{\hbar k}{m_{0}} iP & \frac{2\Delta_{0}}{3} & -\frac{2\Delta_{0}}{3} & 0\\ 0 & 0 & 0 & 0 \end{bmatrix}.$$
(123)

We can construct an exact solution of the band energies by solving the characteristic equation to this eigenvalue problem. Similar to Eq. (97), the exact solutions to Eq. (123) are not useful for our purposes because they cannot be inverted to get the DOS as a function of energy. Instead, we assume that the spin-orbit (SO) coupling is small and approximate  $\Delta_0 \to 0$ . As a result, this approximation makes the center terms in the Hamiltonian matrix (123) zero and gives two degenerate solutions of zero (the hh- and SO-band) and two non-zero solutions (the CB and lh-band). In Figure 39 (a), we can see that in the small SO approximation, the CB fits reasonable well to the exact solution of the band structure (at least in our 8-band  $4 \times 4$  Hamiltonian model). Since there are two zero solutions in the small SO approximation, the hh- and SO-VB are degenerate and lie on top of the exact solution of the hh-band. The effective mass of the electron in CB and the hole in the lh-band are, therefore, given as

$$m_e = \frac{E_0}{E_P + E_0},$$
  $m_{\rm lh} = \frac{E_0}{E_P - E_0}.$ 

However, the band structure in Figure 39 (a) clearly shows that the small SO approximation does not present a good match with the exact solution of the lh-band. For this reason, we will only consider non-parabolicity effects in the CB, while leaving the VB in its parabolic approximation form. Hence, we will only consider  $m_e$  to calculate the DOS mass[44]

$$m_{e,\text{DOS}} = m_e \left[ (1 + \alpha_e \epsilon + \beta_e \epsilon^2) (1 + 2\alpha_e \epsilon + 3\beta_e \epsilon^2)^2 \right]^{1/3}, \tag{124}$$

where [44]

$$\alpha_e = \frac{E_P^2}{E_0(E_0 + E_P)^2},$$

$$\beta_e = -\frac{2E_P^3}{E_0(E_0 + E_P)^4},$$
(125)

and  $\epsilon$  is the energy above the band minimum  $E_0$ . Including  $\alpha$  and  $\beta$  into the DOS effective mass has the effect of overestimating  $\epsilon_2$ . This can be seen in Figure 39 (b). To compensate this, we would have to consider the k-dependence of the

matrix element  $E_P$ , which should bring  $\varepsilon_2$  closer to the experimental value (we do not pursue this here).[81, 111] Still, independently of the approximation, the amplitude of  $\varepsilon_2$  is around one between 1.5 and 3 eV. Therefore, including  $E_0$  in the Tanguy line-shape would not be enough to match the experimental data in the  $E_1$  and  $E_1 + \Delta_1$  region.

### F Surface effects

To showcase the dielectric function for different surface orientations, we measured Ge substrates with (100), (110), and (111) surface orientations. We then follow the procedure explained in Sec. 4.2 to remove the effects of the oxide layer from the data. The (110) surface orientation had an estimated oxide layer thickness of about 28 Å, whereas the (100) and (111) surfaces had a similar oxide layer thickness of about 25 Å. The resulting point-by-point fits are shown in Figure 40. It can be seen that the difference between the samples is negligible. Therefore, we find it unlikely that these surface-related effects are responsible for the discrepancies between theory and experiment observed in our model for the dielectric function near the  $E_1$  and  $E_1 + \Delta_1$  CPs.

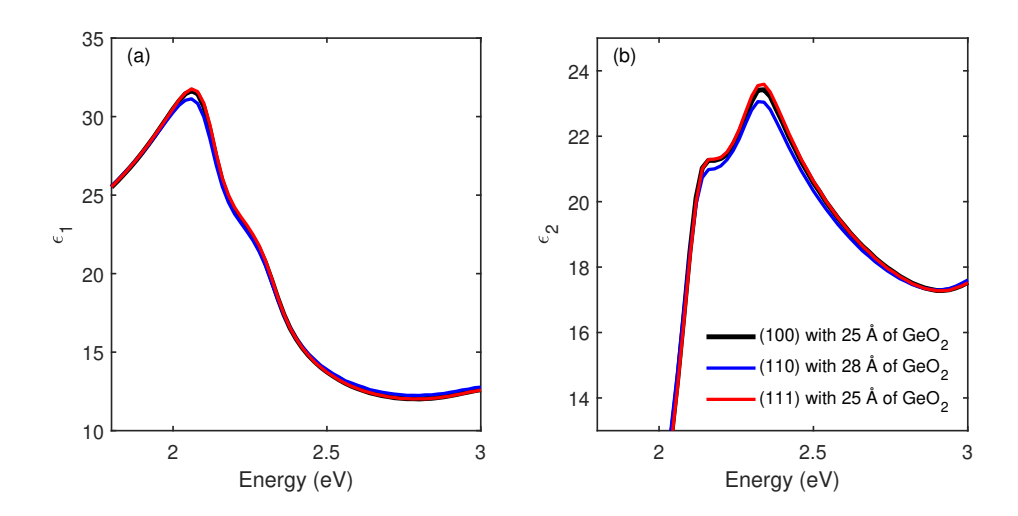


Figure 40: Real (a) and imaginary (b) parts of the dielectric function of Ge from a point-by-point fit for three substrates with (100), (110), and (111) surface orientations (black, blue, and red, respectively).

# G Band-filling effects

The final form of the DF that encompasses band-filling effects is described in Sec. 5.2.2. For the critical point  $E_1$ , it has the form[108, 109]

$$\varepsilon_2(E) = \frac{2e^2 \mu_{\perp}^{(E_1)} \overline{P}^2}{3\pi \varepsilon_0 m_0^2 E^2} H(E - E_1) \int_{-k_{\text{max}}}^{k_{\text{max}}} dk_z \left\{ 1 - f[E_C(E, k_z^2)] \right\}$$
(126)

where  $E_{\rm C}(E,k_z^2)$  is given in Eq. (80). We can analyze the effects of the filling of the bands by adding two similar expressions corresponding to the CPs  $E_1$  and  $E_1 + \Delta_1$  at different points of the chemical potential curve of Figure ?? (a). Figure 41 (a) shows  $\varepsilon_2$  at different points in the calculated chemical potential curve for  $10^{20}$  cm<sup>-3</sup> density. We can see that as the chemical potential increases, the amplitude of  $\varepsilon_2$ 

decreases, consistent with what we see on experimentally. More importantly, as seen in the corresponding 2<sup>nd</sup> derivative, the CP energies do not shift as the band fills up. This indicates that the energy of the CPs are not affected by band-filling effects. We also do not expect to see a Fermi singularity (the bump at around 2.6 eV), given that it is only present at low temperatures.

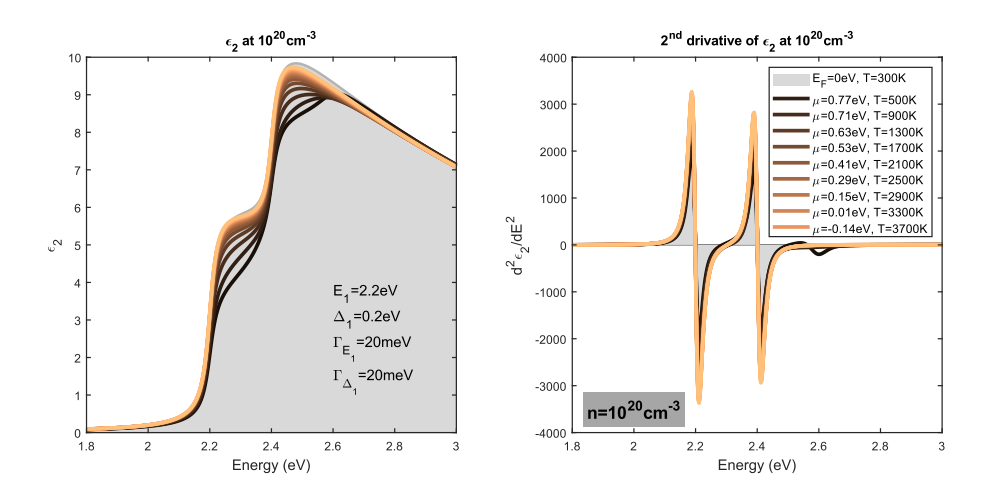


Figure 41: .

## REFERENCES

- M. Cardona, in Atomic Structure and Properties of Solids, edited by E.
   Burstein (Academic Press, New York, 1972), p. 514.
- [2] M. Fox, Optical Properties of Solids (Oxford University Press, 2010).
- [3] H. Kalt and C. F. Klingshirn, Semiconductor Optics 1: Linear Optical Properties of Semiconductors (Springer Nature Switzerland AG, 2019).
- [4] R. J. Elliot, Phys. Rev. 108, 1384 (1957).
- [5] M. Shinada and S. Sugano, J. Phys. Soc. Jpn. 21, 1936 (1966).
- [6] P. Y. Yu and M. Cardona, Fundamentals of Semiconductors: Physics and Materials Properties (Springer, Berlin, 1996).
- [7] M. Grundmann, The Physics of Semiconductors (Springer, Cham, Switzerland, 2021).
- [8] J. I. Pancove, Optical Processes in Semiconductors (Dover, New York, 1971).
- [9] C. Tanguy, Phys. Rev. Lett. **75**, 4090 (1995).
- [10] C. Emminger, N. S. Samarasingha, M. Rivero Arias, F. Abadizaman, J. Menéndez, and S. Zollner, J. Appl. Phys. 131, 165701 (2022).

- [11] J. Menéndez, M. Noël, J. C. Zwinkels, and D. J. Lockwood, Phys. Rev. B 96, 121201 (2017); J. Menéndez, D. J. Lockwood, J. C. Zwinkels, and M. Noël, ibid. 98, 165207 (2018).
- [12] J. Menéndez, C. D. Poweleit, and S. E. Tilton, Phys. Rev. B 101, 195204 (2020).
- [13] M. Dresselhaus, G. Dresselhaus, S. B. Cronin, and A. Gomes Souza Filho, Solid State Properties (Springer, Berlin, 2018).
- [14] M. Cardona, in *Modulation Spectroscopy*, edited by F. Seitz, D Turnbull, and H. Ehrenreich (Academic, New York, 1969).
- [15] J. E. Rowe and D. E. Aspnes, Phys. Rev. Lett. 25, 162 (1970); 25 979 (1970)(E).
- [16] D. E. Aspnes, in *Handbook on Semiconductors*, edited by M. Balkanski (North-Holland, Amsterdam, 1980), Vol. 2, p. 109.
- [17] L. Viña, S. Logothetidis, and M. Cardona, Phys. Rev. B 30, 1979 (1984).
- [18] N. S. Fernando, T. N. Nunley, A. Ghosh, C. M. Nelson, J. A. Cooke, A. A. Medina, S. Zollner, C. Xu, J. Menéndez, and J. Kouvetaskis, Appl. Surf. Sci. 421, 905 (2017).

- [19] H. Fujiwara, Spectroscopic Ellipsometry: Principles and Applications (Wiley, Chichester, 2007).
- [20] J. W. Garland, C. Kim, H. Abad, and P. M. Raccah, Phys. Rev. B 41, 7602 (1990).
- [21] J. Humlíček and F. Lukeš, Phys. Stat. Solid. (b) 77, 731 (1976).
- [22] M. Rohlfing, Phys. Rev. B 82, 205127 (2010).
- [23] B. A. Barker, J. Deslippe, J. Lischner, M. Jain, O. V. Yazyev, D. A. Strubbe, and S. G. Louie, Phys. Rev. B 106, 115127 (2022).
- [24] B. Cunningham, M. Grüning, D. Pashov, and M. van Schilfgaarde, Phys. Rev. B 108, 165104 (2023).
- [25] R. Zimmermann, Jpn. J. Appl. Phys. **34**, 228 (1995).
- [26] C. Tanguy, Solid State Commun. 98, 65 (1996).
- [27] C. Xu, N. S. Fernando, S. Zollner, J, Kouvetakis, and J. Menéndez, Phys. Rev. Lett. 118, 267402 (2017).
- [28] C. Xu, J. Kouvetakis, and J. Menéndez, J. Appl. Phys. **125**, 085704 (2019).
- [29] S. Espinoza, S. Richter, M. Rebarz, O. Herrfurth, R. Schmidt-Grund, J. Andreasson, and S. Zollner, Appl. Phys. Lett. 115, 052105 (2019).

- [30] C. Emminger, S. Espinoza, S. Richter, M. Rebarz, O. Herrfurth, M. Zahradník, R. Schmidt-Grund, J. Andreasson, S. Zollner, phys. stat. solidi RRL 16, 220058 (2022).
- [31] C. A. Armenta, M. Zahradnik, C. Emminger, S. Espinoza, M. Rebarz, S. Vazquez-Miranda, J. Andreasson, and S. Zollner, 2024 IEEE Photonics Society Summer Topicals Meeting Series (SUM), Bridgetown, Barbados, 2024, pp. 01-02.
- [32] C. Emminger, F. Abadizaman, N. S. Samarasingha, T. E. Tiwald, and S. Zollner, J. Vac. Sci. Technol. B 38, 012202 (2020).
- [33] T. N. Nunley, N. S. Fernando, N. S. Samarasingha, J. M. Moya, C. M. Nelson, A. A. Medina, and S. Zollner, J. Vac. Sci. Technol. B 34, 061205 (2016).
- [34] See: https://www.jawoollam.com/
- [35] S. Flügge, Rechenmethoden der Quantentheorie (Springer, Berlin, 1965).
- [36] X. L. Yang, S. H. Guo, and F. T. Chan, Phys. Rev. A 43, 1186 (1991).
- [37] K. A. Velizhanin and A. Saxena, Phys. Rev. B **92**, 195305 (2015).
- [38] T. Mueller and E. Malic, npj 2D Mater. Appl. 2, 29 (2018).
- [39] W. C. Dunlap, Jr. and R. L. Watters, Phys. Rev. **92**, 1396 (1953).
- [40] F. A. D'Altroy and H. Y. Fan, Phys. Rev. **103**, 1671 (1956).

- [41] A. K. Sood, G. Contreras, and M. Cardona, Phys. Rev. B 31, 3760 (1985).
- [42] Y. Ma and J. S. Tse, Solid State Commun. 143, 161 (2007).
- [43] G. Dresselhaus, A. F. Kip, and C. Kittel, Phys. Rev. 98, 368 (1955).
- [44] S. Zollner, C. A. Armenta, S. Yadav, and J. Menéndez, J. Vac. Sci. Technol. A 43, 012801 (2025).
- [45] L. J. Bruner and R. W. Keyes, Phys Rev. Lett. **7** 55 (1961).
- [46] R. Zallen and W. Paul, Phys. Rev. **155** 703 (1967).
- [47] N. W. Ashcroft and N. D. Mermin, Solid State Physics (Saunders, Philadelphia, 1976).
- [48] V. L. Le, T. J. Kim, Y. D. Kim, and D. E. Aspnes, J. Vac. Sci. Technol. B 37, 052903 (2019).
- [49] D. K. Hoffman, D. J. Kouri, E. Pollak, Comput. Phys. Commun. 147, 759 (2002).
- [50] See: https://www.mathworks.com/
- [51] A. Savitzky and M. J. E. Golay, Anal. Chem. **36**, 1627 (1964).
- [52] C. Tanguy, Phys. Rev. B **60**, 10660 (1999).
- [53] J. Menéndez (private communication).

- [54] G. Dresselhaus and M. S. Dresselhaus, Phys. Rev. **160**, 649 (1967).
- [55] D. E. Aspnes, Phys. Rev. B **12** 2297 (1975).
- [56] M. Cardona, Phys. Rev. B **15** 5999 (1977).
- [57] M. K. Kelly, S. Zollner, M. Cardona, Surf. Sci. 285, 282 (1993).
- [58] M. R. Molas, A. O. Slobodeniuk, K. Nogajewski, M. Bartos, Ł. Bala, A. Babiński, K. Watanabe, T. Taniguchi, C. Faugeras, and M. Potemski, Phys. Rev. Lett. 123, 136801 (2019).
- [59] H. T. Nguyen-Truong, Phys. Rev. B 105, L201407 (2022).
- [60] F. Stern and W. E. Howard, Phys. Rev. **163**, 816 (1967).
- [61] D. G. W. Parfitt and M. E. Portnoi, Physica E 17, 212 (2003).
- [62] D. G. W. Parfitt and M. E. Portnoi, in Mathematical Physics, Proceedings of the XI Regional Conference, Tehran, Iran, 3-6 May 2004 (World Scientific, Singapore, 2005), p. 52.
- [63] A. J. Makowski, Phys. Rev. A 84, 022108 (2011).
- [64] H. Kalt and C. F. Klingshirn, Semiconductor Optics 2: Dynamics, High-Excitation Effects, and Basics of Applications (Springer, 2024).
- [65] J. Shah, Ultrafast Spectroscopy of Semiconductors and Semiconductor Nanostructures (Springer Science & Business Media, 1999).

- [66] S. Richter, M. Rebarz, O. Herrfurth, S. Espinoza, R. Schmidt-Grund, and J. Andreasson, Rev. Sci. Instrum. 92, 033104 (2021).
- [67] S. Richter, O. Herrfurth, S. Espinoza, M. Rebarz, M. Kloz, J. A. Leveillee, A. Schleifey, S. Zollner, M. Grundmann, J. Andreasson, R. Schmidt-Grund, New J. Phys. 22 083066 (2020).
- [68] S. Espinoza, S. Richter, M. Rebarz, O. Herrfurth, R. Schmidt-Grund, J. Andreasson, and S. Zollner, Appl. Phys. Lett. 115, 052105 (2019).
- [69] S. Zollner, K. D. Myers, J. M. Dolan, D. W. Bailey, and C. J. Stanton, Thin Solid Films 313-314 568 (1998).
- [70] C. Emminger, S. Espinoza, S. Richter, M. Rebarz, O. Herrfurth, M. Zahradník, R. Schmidt-Grund, J. Andreasson, and S. Zollner, Phys. Stat. Solid. (RRL) 16, 2200058 (2022)
- [71] J. Shah, in *Hot Carriers in Semiconductor Nanostructures: Physics and Applications*, edited by J. Shah (Academic Press, Sn Diego, 1992).
- [72] B. R. Nag, in Semiconductors Probed by Ultrafast Laser Spectroscopy Volume I, edited by R. R. Alfano (Academic Press, Orlando, 1984).
- [73] J. Shah and R. F. Leheny, in Semiconductors Probed by Ultrafast Laser Spectroscopy Volume I, edited by R. R. Alfano (Academic Press, Orlando, 1984).

- [74] P. Vashista and R. K. Kalia, Phys. Rev. B 25, 6492 (1982).
- [75] T. S. Moss, Proc. Phys. Soc. B **67**, 775 (1953).
- [76] E. Burstein, Phys. Rev. **93**, 632 (1954).
- [77] E. Baron, R. Goldhahn, S. Espinoza, M. Zahradník, M. Rebarz, J. Andreasson, M. Deppe, D. J. As, and M. Feneberg, J. Appl. Phys. 134, 075702 (2023).
- [78] E. Baron, R. Goldhahn, S. Espinoza, M. Zahradník, M. Rebarz, J. Andreasson, M. Deppe, D. J. As, and M. Feneberg, J. Appl. Phys. 134, 075703 (2023).
- [79] A. Othonos, H. M. van Driel, J. F. Young, and P. J. Kelly, Phys. Rev. B 43, 6682 (1991).
- [80] A. Othonos, J. Appl. Phys. 83, 1789 (1998).
- [81] P. Y. Yu and M. Cardona, Fundamentals of Semiconductors: Physics and Materials Properties (Springer, Berlin, 1996).
- [82] A. L. Smirl, in Semiconductors Probed by Ultrafast Laser Spectroscopy Volume I, edited by R. R. Alfano (Academic Press, Orlando, 1984).
- [83] B. W. Levinger and D. R. Frankel, J. Phys. Chem. Solids 20, 281 (1961).
- [84] W. Fawcett, Proc. Phys. Soc. **85**, 931 (1965).
- [85] S. H. Groves, C. R. Pidgeon, and J. Feinleib, Phys. Rev. Lett. 17, 643 (1966).

- [86] G. G. MacFarlene, T. P. McLean, J. E. Quarrington, and V. Roberts, Phys. Rev. 108, 1377 (1957).
- [87] R. Kleim, L. Kuntzler, and A. El Ghemmaz, J. Opt. Soc. Am. A 11, (1994).
- [88] P. S. Hauge and F. H. Dill, Opt. Commun. 14, 148 (1975).
- [89] J. Lee, P. I. Rovira, I. An, and R. W. Collins, Rev. Sci. Instrum. 69, 1800 (1998).
- [90] H. G. Tompkins and J. N. Hilfiker, Spectroscopic Ellipsometry: Practical Application to Thin Film Characterization (Momentum Press, 2016).
- [91] See: https://www.coherent.com/
- [92] See: https://www.jawoollam.com/
- [93] X. Q. Zhou, H. M. van Driel, and G. Mak, Phys. Rev. B **50**, 5226, (1994).
- [94] A. I. Lobad, Y. Kostoulas, G. W. Wicks, and P. M. Fauchet, in *Hot Carriers in Semiconductors*, edited by K. Hess, J. P. Leburton, and U. Ravaioli (Plenum Press, New York, 1996).
- [95] M. Zürch, H.-T. Chang, L. J. Borja, P. M. Kraus, S. K. Cushing, A. Gandman, C. J. Kaplan, M. H. Oh, J. S. Prell, D. Prendergast, C. D. Pemmaraju, D. M. Neumark, and S. R. Leone, Nature Communications 8, (2017).

- [96] A. Elci, M. O. Scully, A. L. Smirl, and J. C. Matter, Phys. Rev. B 16, 191 (1977).
- [97] S. Zollner, S. Gopalan, and M. Cardona, Solid State Commun. 76, 877 (1990).
- [98] W. B. Wang, M. A. Cavicchia, and R. R. Alfano, in *Hot Carriers in Semi-conductors*, edited by K. Hess, J. P. Leburton, and U. Ravaioli (Plenum Press, New York, 1996).
- [99] A. L. Smirl, in *Physics of Nonlinear Transport in Semiconductors*, edited by
   D. K. Ferry, J. R. Barker, and C. Jacoboni (Plenum Press, New York, 1980).
- [100] M. Grundmann, The Physics of Semiconductors: An Introduction Including Nanophysics and Applications (Springer, 2021).
- [101] See: https://www.mathworks.com/
- [102] J. Menéndez, C. D. Poweleit, and S. E. Tilton, Phys. Rev. B, 101, 195204 (2020).
- [103] A. Elci, M. O. Scully, A. L. Smirl, and J. C. Matter, Phys. Rev. B 16, 191 (1977).
- [104] H. Kalt and M. Rinker, Phys. Rev. B 45, 1139 (1992).
- [105] C. A. Armenta and S. Zollner, J. Appl. Phys. (under review), (2025).

- [106] M. Cardona, in Atomic Structure and Properties of Solids, edited by E. Burstein (Academic Press, New York, 1972), p. 514.
- [107] J. Humlíček and F. Lukeš, Phys. Stat. Solid. (b) 77, 731 (1976).
- [108] C. Xu, N. S. Fernando, S. Zollner, J. Kouvetakis and J. Menéndez, Phys. Rev. Lett. 118, 267402 (2017).
- [109] C. Xu, J. Kouvetakis and J. Menéndez, J. Appl. Phys. 125, 085704 (2019).
- [110] K. W. Böer, and U. W. Pohl, Semiconductor Physics. (Springer Nature, 2023).
- [111] E. O. Kane, J. Phys. Chem. Solids 1, 249 (1957).
- [112] R. Roucka, Y.-Y. Fang, J. Kouvetakis, A. V. G. Chizmeshya, and J. Menéndez, Phys. Rev. B 81 245214 (2010).
- [113] O. Madelung, Semiconductors, Landolt-Börnstein, New Series Vol. 41, Pt. A (Springer-Verlag, Berlin, New York, 2001).
- [114] D. F. Gibbons, Phys. Rev. **112** 136 (1958).
- [115] G. A. Slack, S. F. Bartram, J. Appl. Phys. 46, 89 (1975).
- [116] G. A. Thomas, E. I. Blount, and M. Capizzi, Phys. Rev. B 19, 702 (1979).
- [117] M. Gienger, P. Gross, and K. Lassmann, Phys. Rev. Lett. **64**, 1138 (1990).

- [118] V. G. Tyuterev, S. V. Obukhov, N. Vast and J. Sjakste, Phys. Rev. B 84, 035201 (2011).
- [119] R. R. Lieten, K. Bustillo, T. Smets, E. Simoen, J. W. Ager III, E. E. Haller, and J.-P. Locquet, Phys. Rev. B 86, 035204 (2012).
- [120] G. Nilsson and G. Nelin, Phys. Rev. B 6, 3777 (1972).